Doctoral Dissertation

LABORATORY STUDY OF CROSS-SHORE SEDIMENT TRANSPORT IN THE SWASH ZONE BASED ON IMAGE ANALYSIS

September 2017

Graduate School of Marine Science and Technology

Tokyo University of Marine Science and Technology

Doctoral Course of Applied Marine Environmental Studies

WU LIANHUI

Doctoral Dissertation

LABORATORY STUDY OF CROSS-SHORE SEDIMENT TRANSPORT IN THE SWASH ZONE BASED ON IMAGE ANALYSIS

September 2017

Graduate School of Marine Science and Technology

Tokyo University of Marine Science and Technology

Doctoral Course of Applied Marine Environmental Studies

WU LIANHUI

Abstract

The active swash zone is arguably the most dynamic part of the nearshore region separating the land and the sea. It is characterized by transient, violent, unsteady multi-phase flow, shallow water depth, high turbulent level, large sediment transport and rapid morphological evolution. A comprehensive understanding of sediment transport in this region is of great importance both for coast protection and engineering application. However, due to the complexity of the swash zone processes, measurement of sediment transport in this region is still challenging up to now, which makes the understanding of the swash zone far from satisfying. Motivated by this, the objectives of this study are 1) to develop a high-resolution measurement technique for swash zone sediment transport and 2) to improve our knowledge of the swash zone by using the measurement technique.

In Chapter 2, a new sediment flux measurement system based on image-analysis is developed. Sediment movement in the target flow is recorded by a high-speed camera with an electronic luminance sheet as a backlight and a stroboscope as a front light source. The instruments are synchronized by a digital delay generator and two types (backlight- and combined- illuminated) of images can be obtained in a series of images by appropriate shifting timing of the instruments. Sediment flux is quantified by simultaneous measurement of sediment concentration and transport velocity at respective location in the recoded images. Sediment concentration is estimated from the backlight-illuminated images according to the Beer-Lambert law. A specially designed PIV algorithm is used to evaluate the sediment transport velocity. Verification tests show that sediment flux up to 300 g/L can be measured with error less than 10%.

In Chapter 3, a laboratory experiment is carried out on an initially plane sand bed (d_{50}=0.16 mm) with a slope angle of 9.5^{o} under dam-break flow in the swash zone. Twenty dam-break flows run over the mobile sand bed and the sediment transport is measured by the system developed in Chapter 2. Sediment concentration, velocity and flux are successfully obtained across the entire water column and the whole swash duration. It is the first time that the sediment dynamics could be completely measured in

the swash zone with such a high resolution (temporal resolution of 0.01 s and spatial (vertical) resolution of 0.27 mm) leading to an extremely valuable database for investigating the swash zone sediment transport.

In Chapter 4, detailed experimental results are illustrated and many new insights are obtained in terms of the swash zone sediment transport. Sediment concentration reaches a peak soon after the swash arrival and it decays gradually until the final backwash where sediment re-suspension takes place resulting in an increase in the concentration. Sand particles generally gather in a thin layer (< 1.0 cm) close to the sand bed. Exceeding this elevation, sediment concentration drops gradually and restlessly due to sinking. The vertical distribution of time-averaged sediment concentration can roughly fulfill the Rouse's profile and the Rouse number is found to be ranging between 0.43 and 0.62. Vertical gradient of the bed-parallel velocity is very large throughout the whole water column in the entire uprush period and is only significant in the lower water column during the backwash. The instantaneous boundary layer thickness can extend to the local water depth in the initial uprush, staying for about 1/10 of the swash period and it is almost zero during flow reversal. The instantaneous boundary layer thickness grows progressively after flow reversal and is limited by the water depth again in the late backwash (keeps approximately 1/5 of the swash period).

The maximum sediment flux for both uprush and backwash occurs between 0.05h and 0.10h (h is the maximum water depth). Sediment flux above the boundary layer is smaller than that inside the boundary layer by one order of magnitude. The magnitude of maximum uprush instantaneous sediment transport load (1.2 kg/m/s) could be twice as large as the backwash value (-0.6 kg/m/s). It is found that the instantaneous sheet layer thickness is approximately 1/3 of the bottom boundary layer depth during the uprush in this study. Sheet flow transport almost vanishes after the flow reversal thus it contributes to a positive (onshore) sediment transport with a magnitude of approximately 10 kg/m/s and it is offset by the suspended load with similar magnitude leading to a very weak accretion in the measurement location. Sediment transport within the bottom boundary layer contributes approximately 75% of the onshore load and 60% of the offshore load. The magnitude of net sediment transport load at each elevation is about half of the one-way sediment transport load. Cumulative net sediment transport

load is offshore in the vicinity of the bed, onshore in the middle of the flow region and almost zero in the upper layers. The difference between the total net sediment transport estimated by the measurement system and that evaluated by the bed level change is small indicating the reliability and accuracy of the measurement system.

In Chapter 5, the logarithmic model is employed in order to derive the bed shear stress for evaluating the Bagnold's model as well as the Meyer-Peter and Müller model. Most of the velocity profiles are well described by the logarithmic model. The maximum bed shear stress occurs in the initial uprush accompanied by the flow arrival and then it decays gradually until the flow reversal. During the backwash, the bed shear stress firstly grows gently, reaching a peak in the middle backwash and decreases after that till the end of the swash event. The equivalent bed roughness is relatively stable (0.03 in the uprush and 0.02 in the backwash) except for the very initial and late period in the uprush and backwash. The Swart formula is found to be appropriate for estimating friction coefficient for most of the swash period except the flow reversal and late backwash.

The Bagnold's model can be used for roughly predicting sediment transport in the swash zone while it overestimates the sediment transport in the initial uprush due to 'phase lag' effect (response time for sand bed to answer the sudden large bed shear stress) and underestimates the sediment transport because of sand re-suspension. Therefore, it is suggested that energetics type models need to be modified by including the 'phase lag' and re-suspension effect. The transport coefficient in the uprush is found to 10 to 20 times as large as that in the backwash. The Meyer-Peter and Müller' model overpredicts the sediment transport in the very initial uprush and underestimates significantly in the residual uprush period. It can predict the backwash sediment transport well while the modeled value lags the measured value slightly. Agreement between the model and measurements is generally within factor order 3. It is supposed that the critical Shields parameter is necessary to be modified corresponding to the grain size. More importantly, sediment advection-diffusion should be incorporated into the model when predicting sediment transport over fine sand beach.

In summary, the present study has released a new sediment flux measurement system based on image-analysis. It is one of (probably the only one so far) the techniques which can be used for quantifying sediment dynamics in various flow conditions with high resolution. The measurement system has been employed in a laboratory experiment to investigate sediment transport in the swash zone and many new insights have been obtained. The experimental results have been further used to examine two sediment transport models, and their capability and limitation are specified. Further studies are expected to be conducted over sand beds with various grain sizes, bed forms and flow conditions based on the measurement system for comprehensive understanding of the swash zone.

Acknowledgements

First and foremost, I would like to express my sincere gratitude to my respectful supervisor Prof. Dr. Akio Okayasu. I still remember the scene when we met at Qingdao for the first time in 2012 and I can remember what we talked at the JCK program entrance interview. I really appreciate him for providing me the opportunity to study at TUMSAT and for the continuous support of my research and life in Japan. Because of his guidance, I know how to do research, how to be a researcher and how to do things in the right way. His immense knowledge (not only in research), strict logic, great patience and continuous encouragement inspired me a lot and certainly will benefit me forever.

I would like to thank my sub-supervisor, Assoc. Prof. Takenori Shimozono at the University of Tokyo for guide me into the development of the sediment flux measurement system and support of my research even after he left TUMSAT. I learned a lot from him through discussions on the research. His high-efficiency, great concentration on research encouraged me a lot and is my forward goal in the future.

I would also like to thank my thesis committee members: Prof. Hisayuki Arakawa, Prof. Tsuyoshi Ikeya, Asscoc. Prof. Masayoshi Toda and Asscoc. Prof. Daisuke Inazu, for their insightful comments and advices. This dissertation has been significantly improved because of their recommendations from various perspectives.

Besides, I would like to thank my senior, Dr. Dejun Feng. I cannot forget those days we fighting together in the Hydraulic Laboratory. I am grateful to him for his help on the PIV programming and data analysis. I am greatly appreciated the previous and current members of CEEL for their generous help not only in research but also in daily life during my stay in Japan.

Special thank goes to my parents, parents-in-law, my elder sister for their support and encouragement during all these years.

Finally, I want to dedicate this dissertation to my beloved wife and daughter. They are the motivation to keep me going.

Table of Contents

List of Figures

List of Tables

Chapter 1 General Introduction

The active swash zone is arguably the most dynamic part of the nearshore region separating the land and the sea. It is characterized by transient, violent, unsteady multi-phase flow, shallow water depth, high turbulent level, great in/exfiltration, large sediment transport and rapid morphological evolution. The swash zone is important both for scientific research and engineering application generally due to the following reasons (from the perspective of physics). The swash zone acts as a 'sponge' between the inner surf zone and the land. Wave breaking, run-up and run-down play critical roles in coastal engineering designs and applications (Kobayashi, 1999). Significant fluid-sediment interactions taking place in this region results in the erosion and accretion and therefore determines the shoreline morphology. The swash zone dynamics further affect the offshore hydrodynamic and beach groundwater greatly.

During the last few decades, many researches have been carried out by means of laboratory/field experiments and numerical approaches to investigate the swash zone processes. Two international workshops on swash zone processes have been held among the swash zone community in 2004 (Puleo and Butt, 2006) and 2014 (Puleo and Torres-Freyermuth, 2016) respectively where research advances and future needs have been specified. Several reviews related to this dynamic region have been published in the last two decades. Butt and Russel (2000) published the first review article focusing on the cross-shore hydrodynamics and sedimentations in the swash zone. Long et al. (2002) summarized the turbulence in the swash zone. Masselink and Puleo (2006) evaluated the swash zone mainly from the morphodynamic perspective. Bakhtyar et al. (2009) analyzed the conceptual and mathematic modeling in terms of the sediment transport in the swash zone. Chardón-Maldonado et al. (2016) concluded the research advances of small-scale hydrodynamics and sediment transport processes in the swash zone from 2004. Braganti et al. (2016) further presented a comprehensive summation of numerical modeling of swash zone process between 2005 and 2015.

Our knowledge of the swash zone has been significantly improved by the assistance of great advances in measurement instrumentations and numerical modelings which have

been summarized in the previous review articles. However, the swash zone is still challenging and our understanding is far from satisfying. Such as air bubbles due to wave/bore breaking affects the acoustic and optical sensors making the measurement of concentration and velocity impossible at the initial uprush phase (Puleo and Torres-Freyermuth, 2016). There is no powerful instrument can resolve the transport velocity inside the sheet flow layer. Thus, velocity profile across the entire flow depth is difficult to be obtained even by using multiple sensors (Puleo et al., 2016). Furthermore, the inability in measuring velocity close to the bed results in the investigation of bottom boundary layer difficult, especially over the natural moveable bed. The commonly used logarithmic model has shown moderate capability in bed shear stress estimation over the unmovable bed; however, more validation is necessary for mobile bed. Turbulence plays an important role in swash zone sediment transport while the existing methods for quantifying the turbulence level are questionable and it is a major unsolved problem in the swash zone study. It is widely acknowledged that the in/exfiltration greatly control the hydrodynamics and sediment transport rate in the swash zone, but very little advance has been made during this century. Instruments for direct measurement of sediment flux profile across the flow depth do not exist. Sediment flux profile is usually achieved by simultaneous measurement of velocity and concentration. However, either velocity or concentration sensors have more or less limitations when employed in the swash zone leading to the quantification of sediment transport hard. Moreover, confidence datasets for evaluating sediment transport and hydrodynamic models are quite limited. So far, much of the laboratory and field experiments are focused on studying the individual swash event whereas swash-swash (or swash-wave) interaction is more practical in the real world. Since the processes within an individual swash circle are not fully transparent, understating of the processes occurring in the sophisticated interacting events remains a long-term task (Puleo and Torres-Freyermuth, 2016; Chen et al., 2016). Among these major (but not completely listed) disadvantages in the swash zone research, one critical and fundamental problem is that sediment dynamics in this region is less quantified making the further investigation of the swash zone difficult. It is essentially due to our inability in measuring sediment transport with a satisfying resolution for analyzing the fundamental swash zone processes.

Motivated by this, the main objectives of the present study are 1) to develop a high-resolution measurement technique for swash zone sediment transport and 2) to improve our knowledge of the swash zone by using the measurement technique. The present dissertation is outlined as the following. Chapter 2 presents a sediment flux measurement system based on image analysis for laboratory experiments. It is capable of quantifying the sediment concentration and transport velocity simultaneously to produce a high-resolution sediment flux measurement. System principle, development process, advantages, and limitations are specified in sequence. Chapter 3 introduces a laboratory experiment conducted over a mobile sand bed under dam-break flow by using the developed sediment flux measurement system. The experimental setup and methodology are explained in detail. The experimental results are described in Chapter 4. Detailed sediment transport characteristics in the swash zone are analyzed extensively with a special focus on the intra-swash processes. The logarithmic model is evaluated in Chapter 5 and it is further used to examine the sediment transport models (Bagnold's model and Meyer-Peter and Müller model) combined with the measurements. General conclusions of the present study are given in Chapter 6.

Chapter 2 Development of Image-Analysis-Based Sediment Flux Measurement System

2.1 Introduction

Compared to the hydrodynamics, sediment transport in the swash zone is less well quantified. One critical problem is that there is no 'efficient' measurement method for quantifying sediment flux. Sediment traps are commonly employed to measure the sediment transport rate without distinguishing the bed load and suspended load (Austin and Masselink, 2006; Hughes et al., 1997; Jackson et al., 2004; Masselink et al., 2009; Masselink and Hughes, 1998). However, they cannot provide any vertical distribution profile of the sediment flux. Horn and Mason (1994) developed a two-layer sediment trap to investigate the proportions of the bed load and suspended load and successfully utilized in the field. But the definition of each transport load is questionable in their study since they simply defined bed load as sediment transport below 1 cm above the bed and suspended load as that above the level. Othman et al. (2014) conducted dambreak swash experiments over a mobile sloping bed to study the relationship between the uprush sediment transport and the grain size. A truncating trap was used in their study to measure the total uprush sediment transport. O'Donoghue et al. (2016) also carried out dambreak type swash experiments by using sediment traps to measure the sediment flux. A trap net with a synchronizer was employed to quantify the intra-swash sediment flux at a predetermined time. This unique technique gives valuable information of intra-swash sediment flux within single swash events.

Sediment flux can also be inferred from a bed evolution rate via the mass conservation law. Turner et al. (2008) described a non-intrusive ultrasonic instrument system, which is able to measure the bed level in a swash-by-swash time scale. Deploying the sensors at multiple locations, they quantified the net sediment transport per uprush-backwash with high frequency. This technique was also successfully employed by Blenkinsopp et al. (2011) in a field experiment. They revealed that beach face equilibrium is achieved by the transport balance over many swash events rather than the intra-swash balance.

More commonly, sediment flux is obtained by co-located measurements of sediment concentration and transport velocity (Aagaard and Hughes, 2006; Butt et al., 2004, 2005; Masselink et al., 2005; Osborne and Rooker, 1999; Puleo, 2009; Puleo et al., 2000, etc.). The vertical resolution of the sediment flux largely depends on the density of deployed instruments since most of the concentration and velocity devices in the field are only for single-point measurement (e.g. optical backscattering sensor (OBS), acoustic Doppler velocimeter (ADV), electromagnetic current meter (EMCM). Moreover, due to the instrument disability in the vicinity of the bed, bed load transport is often not considered. Very recent studies have attempted to fill the gaps in the absence of intra-swash bed load transport. For instance, van der Zanden et al. (2015) used a conductivity-based concentration measuring technique (CCM^+) with a sampling frequency of 1000 Hz to analyze the phase-averaged intra-swash sheet flow concentrations, particle velocity, sediment flux and bed level evolution. While the probe mounted in the CCM^+ can only do single point measurement and it needs to be moved up and down to obtain the vertical concentration profile, which means that the CCM^+ is only able to be used under periodic flow conditions. Puleo et al. (2016) and Ruju et al. (2016a, b) utilized Acoustic Doppler velocity profilers (ADVP) and conductivity concentration profilers (CCP) to quantify the sheet flow sediment flux. Both ADCP and CCP have a vertical measuring range of 0.03 m with a resolution of 0.001 m, combining with the suspended flux measured by ADVs and OBSs, extremely valuable information of intra-swash sediment transport was obtained. However, velocities in the sheet load transport layer were not successfully measured in their study due to signal attenuation attributed to high sediment and bubble concentrations. Complete velocity and sediment flux profiles are not able to be achieved because of the significant temporal and spatial data gaps in their measurements.

With the acknowledgment of the current situation that there is no powerful technique for quantifying sediment flux which significantly obstructs the understanding of the swash zone sediment transport, a sediment flux measurement system based on image analysis is developed for measuring sediment flux in the swash zone. The measurement system is developed on the basis of several previous efforts (Masame, Y., 2013; Shimozono et al. 2008, 2012, and 2013). In Sect. 2.2, the existing sediment flux

measurement system will be introduced including its mechanism and limitations. After that, the development of improved image analysis based sediment flux measurement system will be explained. Finally, a validation experiment is conducted in order to evaluate the accuracy and measurement range of the developed system.

2.2 Pre-existing sediment flux measurement system

Shimozono et al. (2012, 2013) developed the original sediment flux measurement system based on image analysis techniques. Fig. 2-1 shows the front and cross-sectional views of the measurement system. The measurement system is made up of an electronic luminescence sheet (EL-Sheet hereafter) and a high-speed camera. The EL-sheet is set in the target flow as a backlight to illuminate the sand-water flow. It is a planar lighting device with a brightness of 300 cd/m^2 and the central wavelength of 510-520 nm. The EL-Sheet is like a stiff paper that can be placed in water without disturbing the target flow significantly (parallel to the flow direction) since its thickness is only about 0.5 mm. The high-speed camera is used for recording sediment movement in the target flow. Sediment concentration and transport velocity are measured from the recorded images by two image-analysis techniques. Sediment flux is derived by multiplying sediment concentration and transport velocity at respective locations in the recorded images.

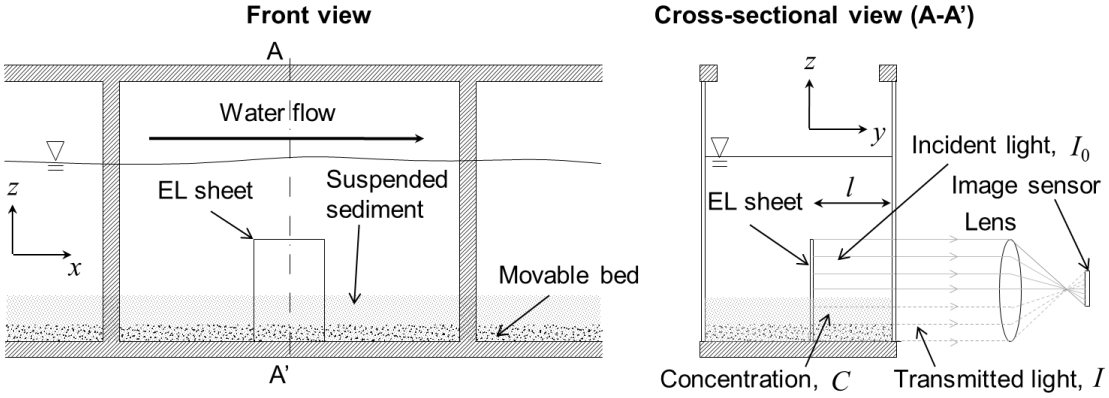

Figure 2-1. Schematic of the pre-existing sediment transport measurement system

2.2.1 Principle of sediment concentration measurement

Sediment concentration is measured by a light extinction method developed by Shimozono et al. (2008). This method is based on the Beer-Lambert law, which is commonly used for chemical analysis. The law states that the light transmissivity has a logarithmic relationship with the product of the attenuation coefficient of the substance and the path length. It is written as follows,

$$A = -\log\frac{I}{I_0} \tag{2-1}$$

$$A = \sigma_{ext} l \tag{2-2}$$

$$\sigma_{ext} = \frac{\pi d_s^2}{4} N Q_{ext} \tag{2-3}$$

where A is the light attenuation due to the existence of sand water flow. σ_{ext} is the attenuation coefficient. l is the path length that stands for the distance the light travels through the material. I_0 and I are the initial light intensity of the EL-sheet and detected light intensity after the presence of sediment particles respectively. d_s is the sand particle diameter and N is the particle number density. Q_{ext} is the absorption coefficient related to the substance the light travels through. In the case of chemical analysis, the light attenuation is mostly due to the absorbance by the solutes, while for the present case, it is because of reflection and scattering by the sand particles in the water.

The particle number density can be transformed into mass concentration as:

$$N = \frac{6c}{\rho\pi d_s^3} \tag{2-4}$$

where c, ρ, d_s are sediment concentration, sediment density, and sediment particle diameter separately. Then Eq. 2-2 can be written as follows by substituting Eq. 2-3 and Eq. 2-4 into it,

$$A = \frac{3}{2} Q_{ext} \frac{cl}{\rho d_s} \tag{2-5}$$

By giving l, ρ, d_s, sediment concentration is able to be derived from Eq. 2-5 if Q_{ext} could be determined since light attenuation can be measured from the recorded images. Therefore, a previous calibration is necessary to determine the relationship between the sediment concentration and light attenuation (e.g. the factor of Q_{ext}).

2.2.2 Principle of transport velocity measurement

Particle Image Velocimetry (PIV) is used for measuring transport velocity in this system. A traditional PIV system usually consists of several sub-systems. In most applications tracer particles have to be added into the flow and need to be illuminated in a plane of the flow at least twice in a short time interval. The distribution of illuminated particles has to be recorded by the camera (usually high-speed camera) either on a single frame or a sequence of frames. Then the displacement of the particles images between the light pulses needs to be determined through evaluation of the recorded frames. The tracer particles need to move with the local flow very well in order to precisely present the velocity field of the flow, so a careful selection of the tracer particles is very necessary and important (such as particle density, size, concentration).

The recorded frames are divided into small subareas called interrogation windows. The displacement of each interrogation window is determined by comparing the image pattern in the window between two illuminations. It is assumed that all particles within one interrogation window move homogeneously between two illuminations. The displacement evaluation process is done by means of statistical methods (auto- and cross-correlation). A careful adjustment of the recording rate is necessary according to the flow condition for the purpose of displacement evaluation. On one hand, if the recording rate is too small, tracer particle distribution in the interrogation window of the

second illumination would be disorder compared to that in the first illumination, leading to the failure of correlation. On the other hand, if the recording rate is too high, movement of the tracer particles would be very small, probably resulting in a large error of correlation. In addition, the seeding concentration of tracer particles also affects the statistic significantly. Either too high or too low seeding concentration might result in the failure of the displacement evaluation. Taking into account of the time interval of two illuminations and the magnification of PIV recording, local flow velocity could be determined by the displacement of the interrogation window. A whole velocity field could be achieved by integrating velocity vector of each interrogation window. Image evaluation of the PIV recording is the most complex work for velocity measurement. There are many kinds of pre- and post-processing techniques need to be employed according to the practical situation.

For the present measurement system, sand particles are assumed as tracer particles since adding other kinds of tracer particles will give rise to measurement error of sediment concentration evaluation. Traditional PIV aims at measuring the flow velocity, however, sand particles are not likely to faithfully follow the flow well due to its high density compared to the water flow. Thus, the measured result is particularly the velocity of the sand particles themselves rather than the water flow.

Normal PIV is a non-intrusive measurement technique since laser sheet is shot into the target flow to illuminate the tracer particles. Here, because the EL-sheet is used as the light source, the measurement is no longer non-intrusive. In addition, the light sheet thickness of the laser is generally very thin (less than 1 mm), so each measured velocity vector is a mean value of the tracer particles in the 2D interrogation window. However, the EL-sheet is a planar backlight being able to illuminate the sand particles in front of it. So velocity vector in the present measurement system is a mean value of sand particles in a 3D sand-water bulk, although the interrogation windows in the recorded frames are 2D. Moreover, the distribution of sediment concentration in real flow is not controllable, making the sand particles in each interrogation window significantly inhomogeneous. Therefore, the present PIV analysis is different from the traditional type and is much more complicated.

2.2.3 Advantage and limitation of the pre-existing sediment flux measurement system

PIV is a whole field measurement technique since the velocity information can be extracted from each interrogation window with moderate tracer particles. Since sediment concentration can also be measured at each interrogation window, the spatial resolution of sediment flux (product of sediment concentration and transport velocity at respective locations) is quite large. Integrating sediment flux is much easier because sediment concentration and transport velocity are able to be measured at the same location (interrogation window) simultaneously. This allows a detailed investigation of hydrodynamics and sediment transport processes as most instruments either for velocity or sediment concentration only provide measurement at a single point.

Shimozono et al. (2012) verified the performance of the measurement system by conducting a series of tests. The results suggest that the system is capable of quantifying sediment flux with less than 10% error in the condition of light attenuation factor A smaller than 2.5. When sediment concentration goes higher, a large part of the incident light from the EL-sheet is obstructed and the interrogation window is full of sand particles. Image patterns thus disappear from the interrogation window and PIV analysis fails due to losing of this vital information for statistical evaluation.

2.3 Development of the improved sediment flux measurement system

The pre-existing sediment flux measurement system is confined due to its limited measurement range. Expanding of the measurement system is necessary for a better employment in much wider conditions. In order to overcome the difficulty in velocity evaluation of the pre-existing measurement system, several new instruments are employed in the improved measurement system. Fig. 2-2 illustrates the side view of the improved measurement system. Similar with the previous one, there is an EL-Sheet set in the target flow as a backlight. A high-speed CMOS camera (IDT Inc., M3) is used to record motion images of sediment movement with a maximum resolution of 1280×1024 pixels. As mentioned above, PIV analysis will break down due to the disappearance of the traceable patterns in the interrogation window when the sediment concentration is high. The reason is that incident light from the EL-sheet cannot pass through the flow because of a huge amount of sediment particles in that case. Therefore, a stroboscope

(Nissin Electronic CO., Ltd., JX612, 0.3 J/F, the exposure time is 15-30 μs, the maximum frequency is 200 Hz) is installed in front of the experimental flume as an additional light source to illuminate the highly concentrated sand water flow. Synchronized by a digital delay generator (Stanford Research Systems, Inc., DG645), the stroboscope is controlled to give out light at half of the frame rate. Thus, normal (EL-sheet only) and combined-illuminated (EL-sheet and stroboscope) images are alternatively obtained at the same frequency.

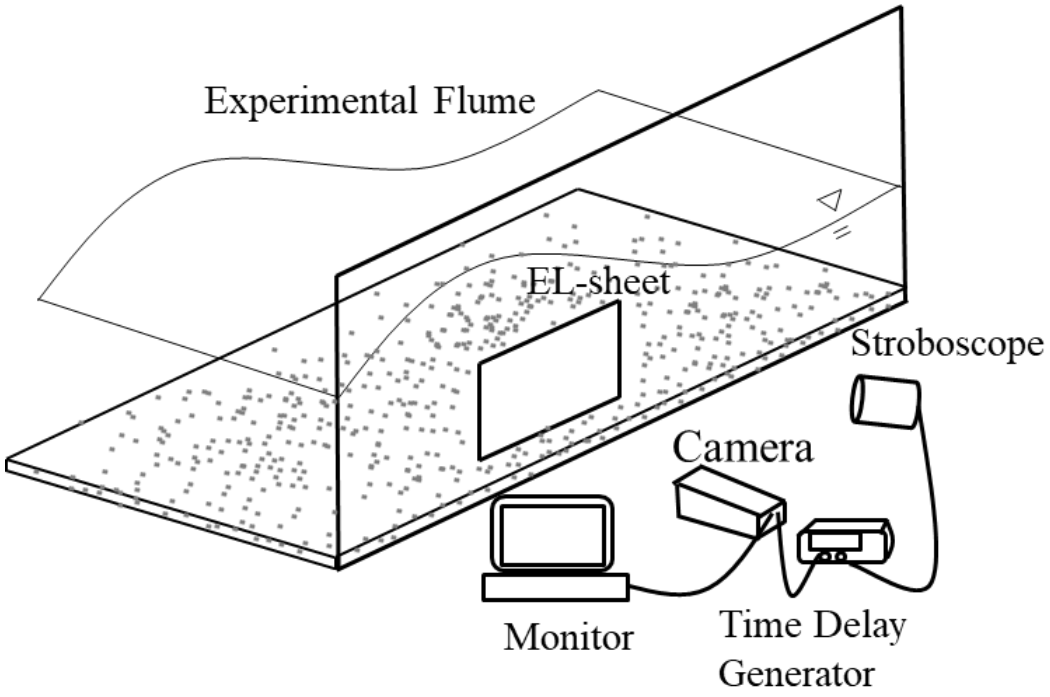

Figure 2-2. The improved image-analysis-based sediment flux measurement system

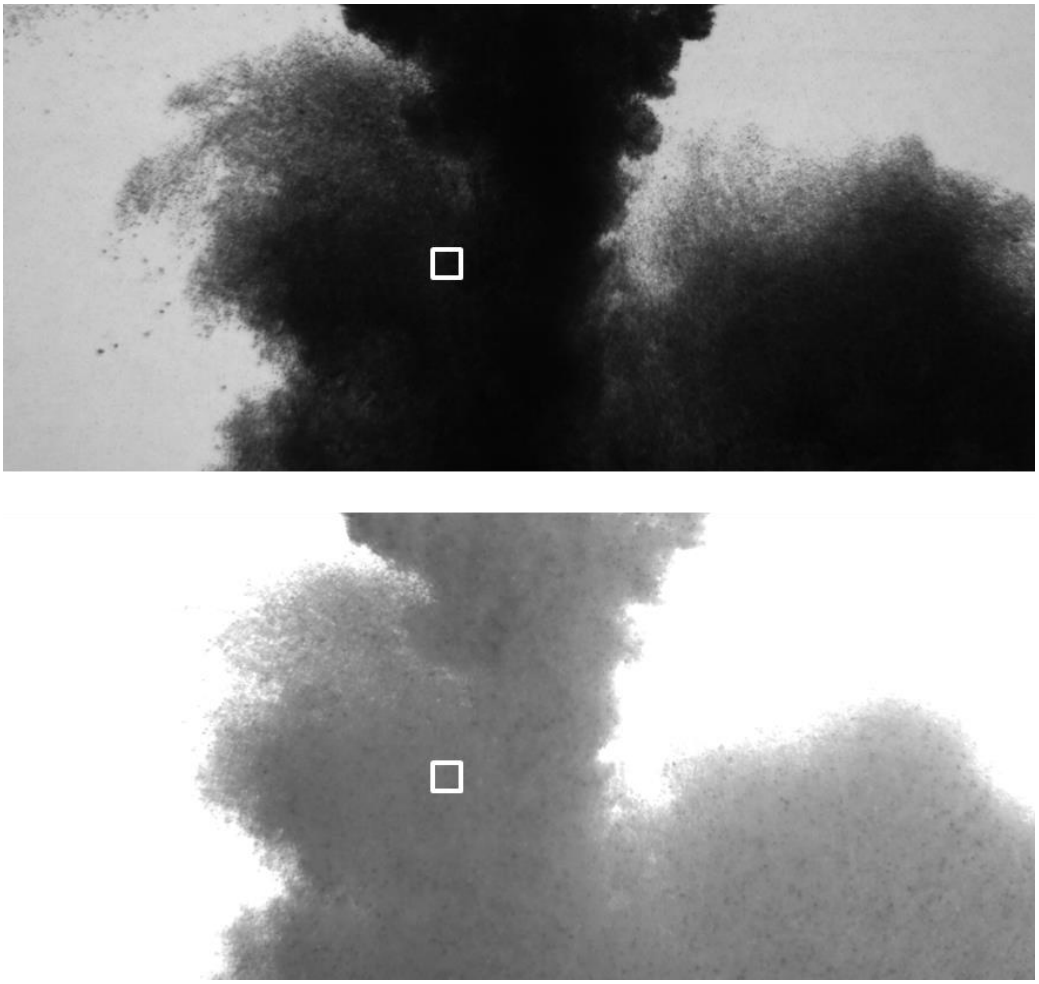

Figure 2-3. Example images of normal (upper) and combined-illuminated (lower) images in dense sediment concentration condition, light intensity distributions of the squares are shown in Fig. 2-4

Example images of instantaneous normal and combined-illuminated images of dense sediment concentration are shown in Fig. 2-3. Light intensity distributions are plotted in Fig. 2-4 of interrogation windows at the same location of the two images indicated in Fig. 2-3. It is found that the highly concentrated sand water flow is able to be illuminated by the stroboscope to provide clear image pattern for PIV analysis. Therefore, normal images can be used for concentration measurement same with the pre-existing measurement system and combined-illuminated images are expected to give velocity vectors by using PIV analysis.

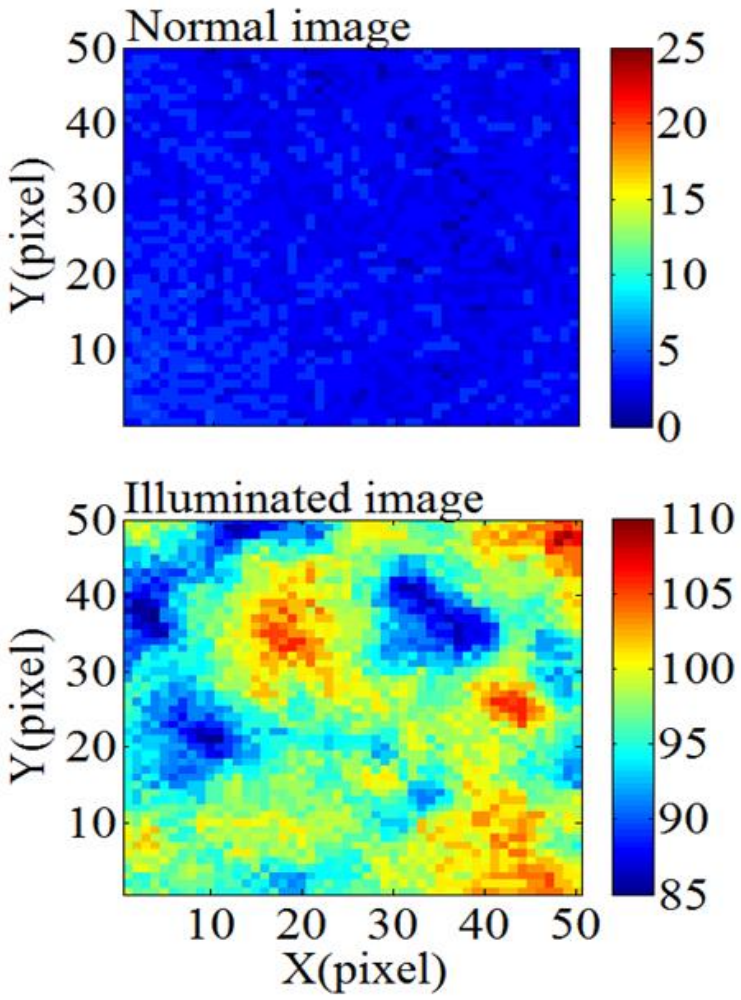

Figure 2-4. Light intensity distributions of the squares indicated in Fig. 2-3, the upper one is the normal image and the lower one is the combined-illuminated image. Colorbar indicates the light intensity in gray-scale

2.4 Verification of the improved sediment flux measurement system

In order to evaluate the capability of the improved sediment flux measurement system, a serious of verification tests was carried out. As has been indicated before, it is necessary to determine the correlation coefficient k (k=1.5$Q_{ext}/\rho d_s$) in the Beer-Lambert law for the measurement of sediment concentration. Hence, calibration test of the Beer-Lambert law was conducted firstly.

2.4.1 Calibration of the Beer-Lambert law for sands

Transparent acrylic containers filled with a sand water solution of precisely known concentration was used for calibration tests (Fig. 2-5). For each time, the container was filled with a certain amount of silica sand with a median diameter of 0.16 mm, and it was shaken by hands to uniform the concentration throughout it and was immediately placed in front of the EL-sheet. The high-speed camera was focused on the container with a certain distance. After putting in front of the EL-sheet, sediment particles started to deposit and air bubbles went up swiftly, while the concentration still remained uniform and kept constant for a while in the middle layer of the container (Fig. 2-6). Meanwhile, the high-speed camera was triggered to record this process, and then the light attenuation could be evaluated from the average light intensity over the corresponding part of the recorded images. In order to cover a wide range of concentrations, a serious of concentrations were used in the calibration. Moreover, containers with different width (path length) of 1.0 cm, 1.5 cm, 2.0 cm, 3.0 cm, 4.0 cm, 4.5 cm and 5.0 cm were used in the calibration. In each case, the procedure was repeated several times to minimize the accidental error. Detailed calibration conditions are listed in Table 2-1 and example images of different light attenuation are illustrated in Fig. 2-7. Specific calibration results of each path length are shown in Fig. 2-8.

The relationships between the sediment concentration and light attenuation do not satisfy the Beer-Lambert law strictly when light attenuation turns to be very large. This phenomenon is caused by strong light scattering when the concentration is very high as the silica sand is non-absorptive material. And it is more obvious accompany with the increase of the path length. In the case of path length equals to 1.0 cm, the relationship between concentration and light attenuation can keep linear until the concentration exceeds 300 g/L, while in the case of path length equals to 5.0 cm, the linearity can only maintain below 40 g/L. Therefore, a careful selection of the path length is necessary when conducting flume experiments. If the sediment transport is expected to be significant, a small path length might be suitable as its measurement range large. Otherwise, big path length is suggested because the influence due to the EL-sheet is mild when the distance between the EL-sheet and side wall is large.

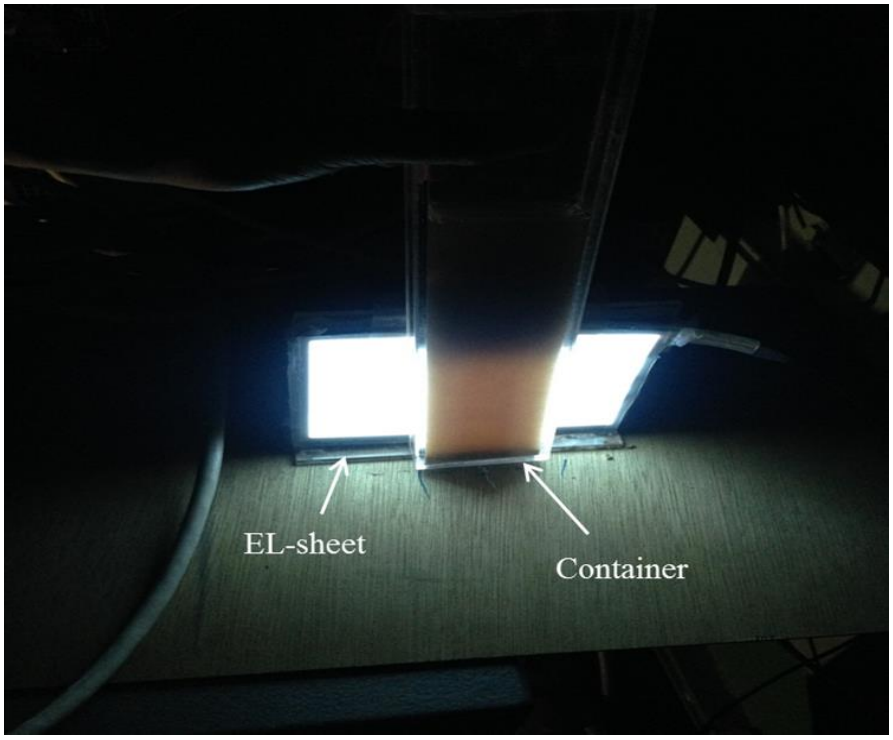

Figure 2-5. Photo of the acrylic container and the EL-sheet used in calibration

Sand water mixture in the container resembles the concentrated sand flow between the EL-sheet and flume sidewall. So the calibration result could be directly employed in real flume experiments if the path length is identical with the container width and the distance from the high-speed camera to the EL-sheet is constant. However, it is worth noting that the calibration is also affected by the following factors: aperture size of the high-speed camera, shutter speed, the distance between the high-speed camera and the EL-sheet. The aperture size and shutter speed control how much light reaches the image plane. Narrow aperture and large shutter speed give dark images and vice versa. Table 2-2 and Fig. 2-9 illustrates the comparison between large and small aperture sizes in the path lengths of 2.5 cm and 4.5 cm. It is obvious that two calibration curves are completely different. For large aperture, higher concentration range can be measurable but low concentration band is missing. On the contrary, low concentration band is measurable while the measurement range is quite limited for a small aperture. The shutter speed and distance between the high-speed camera and the EL-sheet also have a

similar effect. This means that when we employ these calibration curves in a laboratory experiment, the experimental condition should be exactly the same with the calibration conditions. However, making the setup of the high-speed camera exactly same with the calibration condition will limit the flexibility of instruments setup as the high-speed camera need to be installed somewhere according to the measurement objective and also the aperture size and shutter speed need to adjusted to find an optimal setting depending on the practical condition.

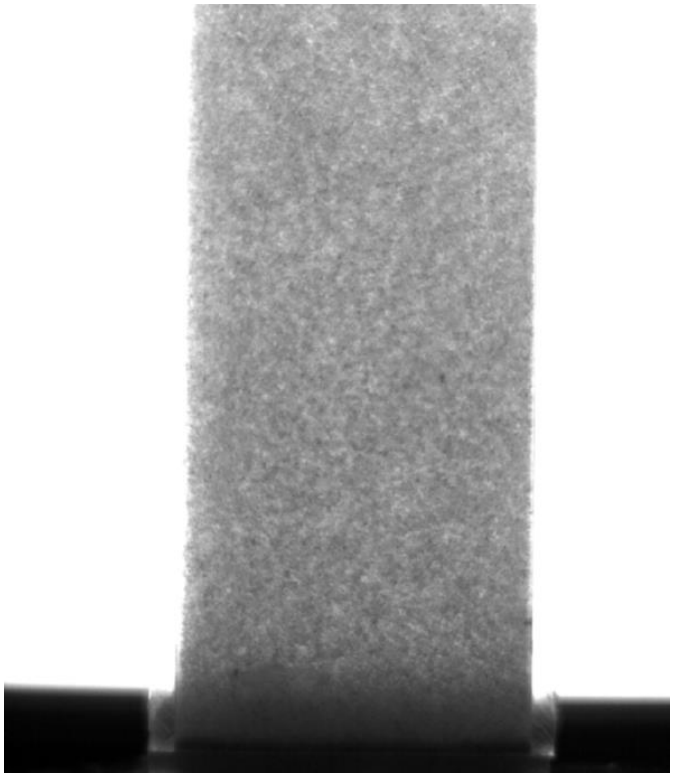

Figure 2-6. Example recorded image of water-sand mixture in the calibration

Through a serious of tests, it is found that making the laboratory experimental conditions and the calibration conditions completely identical is not necessary. There are two sufficient factors to ensure that calibration result can be applied in flume experiments. One is that the distance from the high-speed camera to the EL-sheet must be same between the calibration condition and laboratory experimental condition. Another one is that the incident light intensity of the EL-sheet recorded by the high-

speed camera must be same between the calibration condition and laboratory experimental condition, which can be achieved by adjusting the aperture size and shutter speed. However, for the conditions of large aperture size, the camera is overexposure and the incident light intensity maintains in 255 (maximum value of light intensity) despite the increase in concentration in a certain concentration range (e.g. calibration result of large aperture size in the path length of 2.5cm). In that case, the incident light intensity of EL-sheet cannot be used as an indicator, while the transparent container used in calibration experiments can be applied for adjusting the camera aperture size and the shutter speed. The method is similar to the calibration experiments. After fixing the position of the high-speed camera, the transparent container loading with precisely known concentrations of sediment can be put in the experimental location to check the light intensity. Once the light intensity is same with the calibration result under the same concentration by means of using different combinations of aperture size and shutter speed, the calibration curve is considered could be used in that experimental condition. Therefore, determination of the high-speed camera and the EL-sheet is the first step before conducting calibration. It is also worth noting that the light attenuation in the calibration are measured from mean values of light intensity of small areas rather than single pixel intensity in the recorded images. This is because even similar sand particles generate different light attenuation due to the small difference in the morphology (e.g. shape, size, color), so using single pixel intensity to measure light attenuation would bring large errors. Therefore, mean values of light intensity are suggested to measure sediment concentration in practical cases.

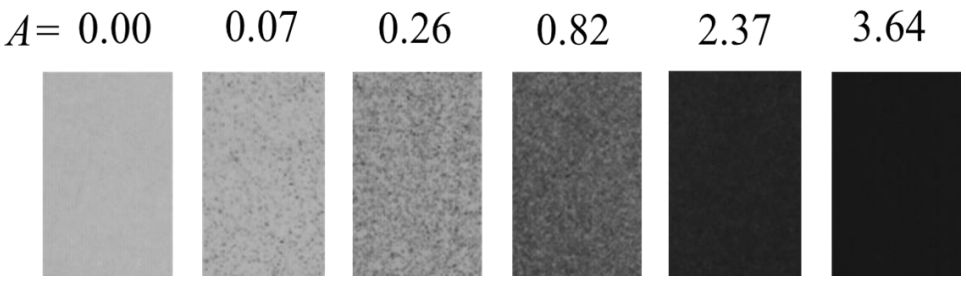

Figure 2-7. Example images of different light attenuation

Table 2-1. Experimental conditions of calibration for the Beer-Lambert law

Path length (cm)	1.0	1.5	2.0	2.5	3.0	4.0	4.5	5.0
Case 1	0	0	0	0	0	0	0	0
Case 2	1	1	1	1	1	1	1	1
Case 3	2	2	2	2	3	3	2	2
Case 4	3	5	5	3	5	5	3	5
Case 5	4	10	10	4	10	10	4	10
Case 6	5	20	20	5	15	15	5	20
Case 7	10	30	30	10	20	25	7	30
Case 8	20	50	40	15	30	35	10	40
Case 9	30	75	50	20	40	45	15	50
Case 10	50	100	75	25	60	55	20	75
Case 11	80	125	100	30	80	70	30	100
Case 12	100	150	125	40	100	85	40	150
Case 13	150	175	150	50	120	100	50	200
Case 14	200	200	200	60	150	150	60	300
Case 15	250	225	250	80	200	200	80	
Case 16	300	250	300	100	300	300	100	
Case 17	350	300	350	150			150	
Case 18	400	350		200			200	
Case 19	500			300			300	

Table 2-2. Calibration conditions for evaluating the effect of different aperture size

Path length	Aperture size										
2.5 cm	small	c (g/L)	0	1	2	3	4	5	7	10	15	20
		A	0.00	0.00	0.01	0.02	0.04	0.07	0.14	0.28	0.49	0.74
		c (g/L)	25	30	40	50	60	80	100	150	200	300
		A	0.95	1.21	1.62	1.99	2.42	3.03	3.29	3.86	4.21	4.29
	large	c (g/L)	0	2	4	10	20	30	40	50	60	70
		A	0.00	0.00	0.00	0.00	0.00	0.18	0.65	1.04	1.41	1.80
		c (g/L)	80	110	130	150	170	190	220	250	300	350
		A	2.08	2.83	3.19	3.43	3.61	3.75	3.83	3.87	3.90	3.97
4.5 cm	small	c (g/L)	0	1	2	3	4	5	7	10	15	20
		A	0.00	0.04	0.13	0.21	0.30	0.38	0.56	0.82	1.25	1.65
		c (g/L)	25	30	40	50	60	80	100	150	200	300
		A	1.96	2.27	2.89	3.28	3.68	4.08	4.26	4.44	4.45	4.45
	large	c (g/L)	0	1	5	8	10	20	30	40	50	60
		A	0.00	0.00	0.00	0.00	0.00	0.78	1.50	2.10	2.69	3.09
		c (g/L)	70	80	110	130	150	170	190	220	250	300
		A	3.41	3.67	3.98	4.06	4.11	4.18	4.21	4.22	4.22	4.23

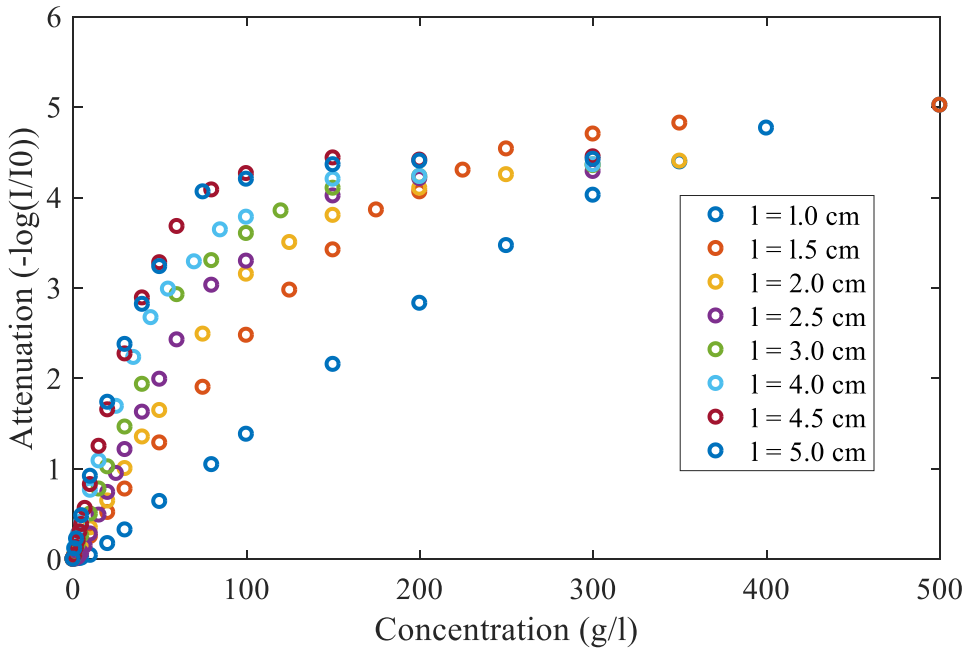

Figure 2-8. Relationship between the sediment concentration and light attenuation for different path length

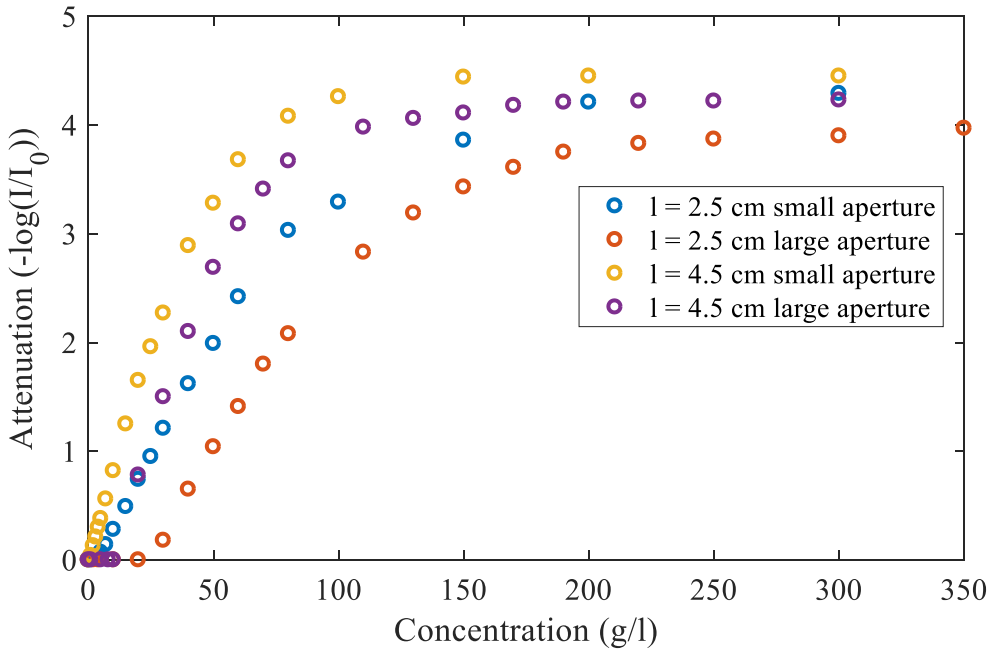

Figure 2-9. Calibration results of the Beer-Lambert law for sands by using different aperture size

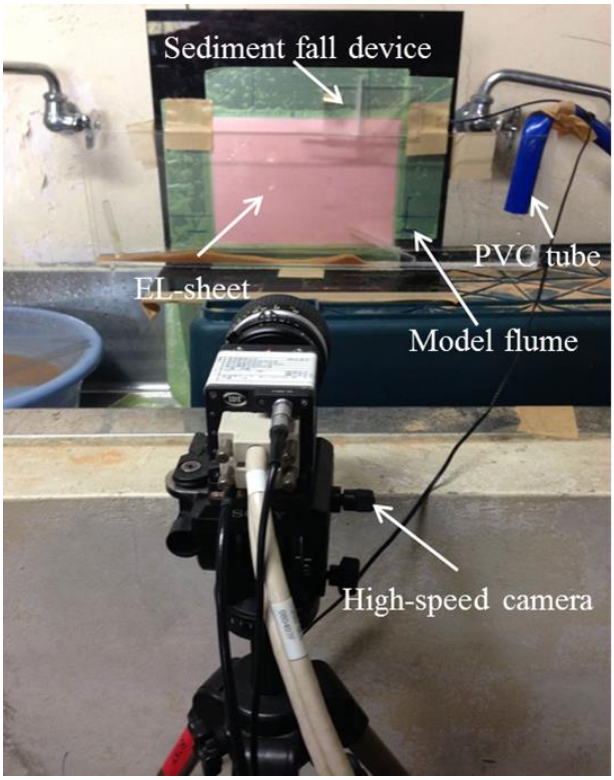

Figure 2-10. Experimental setup for the validation test

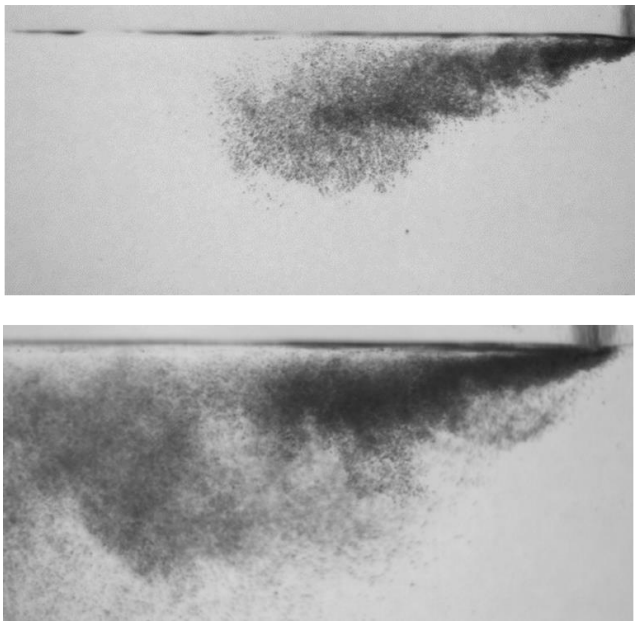

Figure 2-11. Example recorded images of validation test

2.4.2 Evaluation of the influence of the path length

Before validating the improved sediment flux measurement system, a series of tests were carried out for investigating the measurement range of each path length of the pre-existing measurement system. Because sediment concentration is not so large in some sediment transport experiments that the measurement range of the pre-existing system is enough for investigation. A clear determination of measurement range of the pre-existing system is necessary, for the purpose of better employment of itself and the improved measurement system.

The configuration of verification tests is shown in Fig. 2-10. An EL-sheet (20×15 cm^2) was stuck on the backside wall of a transparent flume. The model flumes were made of acrylics with length of 50 cm, height of 15 cm. There was a PVC tube connected to tap water at one side of the flume, used for generating flow. A gate was installed at the other end of the flume to control the water depth. Silica sands with a median diameter of 0.16 mm were released into model flumes through a simple sediment fall device. This device enables the sand particles drop into the flume uniformly perpendicular to the sidewall. Sand particles then moved under the resultant force of the gravity and flow. The high-speed camera was 30 cm from the model flumes to record the sand movement. By using a lens with fixed 50 mm focal length, the setup gives a resolution parameter λ = 100 μm/pixel. The high-speed camera was set in an fps (frames per second) of 500. Six model flumes with a width of 1.0 cm, 1.5 cm, 2.0 cm, 3.0 cm, 4.0 cm and 5.0 cm separately were used in the verification tests. For each model flume, six different amounts of sands were released into the flow and were compared to the sand load measured by the system to evaluate the measurement accuracy at each path length. Examples of recorded images are given in Fig. 2-11.

For each case, several inspection lines were set to measure the sediment flux. Distance interval between two adjacent inspection lines was 40 pixels. On each inspection line, velocity was calculated in a distance interval of 12 pixels. Direct cross-correlation method was used on each adjacent images pairs to calculate the integer displacement of the interrogation windows. The direct cross-correlation is the most accurate displacement determination method for PIV analysis even though its computational

effort is quite large. In the direct cross-correlation, the interrogation window in the first image is used as a sample to find the most similar (highest cross-correlation coefficient) one in the second image. The cross-correlation coefficient *R* is determined by,

$$R(x,y) = \frac{\sum_{j=-k}^{k}\sum_{j=-l}^{l} G(i,j)G'(i+x,j+y)}{\sqrt{\sum_{j=-k}^{k}\sum_{j=-l}^{l} G^2(i,j)}\sqrt{\sum_{j=-k}^{k}\sum_{j=-l}^{l} G'^2(i+x,j+y)}} \quad (2\text{-}6)$$

The variables *G* and *G'* are the intensity values as extracted from the images where *G*' is larger than the template *G*. Essentially the template *G* is linearly 'shifted' around in the sample *G'* without extending over edges of *G'*. (*x*, *y*) is the image plane coordinate of the interrogation window. *i*, *j* are the integer distances with a unit of pixel in the direction of horizontal and vertical respectively, and (*i* + *x*, *j* + *y*) is the image plane coordinate of the region in the search window where cross-correlation was carried out with the interrogation window. For each choice of sample shift (*x*, *y*), the sum of the products of all overlapping pixel intensities produces one cross-correlation value *R*(*x*, *y*). By applying this operation for a range of shifts (-*M* ≤ *x* ≤ +*M*, -*N* ≤ *y* ≤ +*N*), a correlation plane the size of (2*M*+1) × (2*N*+1) is formed. For shift values at which the samples' particle images align with each other, the sum of the products of pixel intensities will be larger than other locations, resulting in a high cross-correlation value *R*(*x*, *y*) at this position. Essentially the cross-correlation function statistically measures the degree of match between the two samples for a given shift. The highest value in the correlation plan can then be used as direct estimate of the particle image displacement. The direct cross-correlation gives velocity vectors at the accuracy of one pixel. In order to enhance the estimation accuracy, peak detection technique was carried out to improve the accuracy to the order of 1/10 pixel (subpixel level). The principle of the peak detection method is beyond the scope of the present study, so only the calculation method introduced here. The three-point estimators are the most widely used peak detection methods, and in this study, the Gaussian peak fit is chosen to improve the measurement accuracy of velocity. The estimator is written as,

$$x_1 = x_0 + \frac{\ln R(i-1,j) - \ln R(i+1,j)}{2\ln R(i-1,j) - 4\ln R(i,j) + 2\ln R(i+1,j)} \quad (2\text{-}7)$$

$$y_1 = y_0 + \frac{\ln R(i,j-1) - \ln R(i,j+1)}{2\ln R(i,j-1) - 4\ln R(i,j) + 2\ln R(i,j+1)} \quad (2\text{-}8)$$

where, (x_1, y_1) is the coordinate of peak detection result with accuracy of subpixel. (x_0, y_0) is the image plane coordinate where the highest cross-correlation coefficient occurs. i, j are the inter displacement calculated by the cross-correlation for horizontal and normal direction respectively.

Interrogation widow with a size of 24×24 pixels was applied in the direct cross-correlation. Meanwhile, the average value of light intensity in the interrogation window was used to calculate the concentration based on the previous calibration result. Thus, the overlap between two adjacent interrogation areas was 50%, giving a 47×16 velocity vector grid and concentration grid with a spatial resolution of 4.7 mm and 1.6 mm. Total sediment flux can be integrated at every inspection line, and transport load of sand is able to be derived by assuming a uniform distribution of sediment flux perpendicular to the EL-sheet as follows,

$$M_s = \int_o^T c(x,y)u(x,y)dldt \quad (2\text{-}7)$$

where, M_s is measured transport load (mass). T is the duration of sands falling into the flume. c and u are sediment concentration and transport velocity at each interrogation window, respectively. d is distance interval between the centers of two adjacent interrogation windows. l is the path length (flume width). The measured mass is compared to the input mass for evaluating the reliability and accuracy of the pre-existing measurement system. Example results of velocity and concentration measurement are shown in Fig. 2-12. Detailed results of the verification tests for determining the measurement range and effect due to the path length of the pre-existing measurement system are illustrated in Table 2-3. Similar conclusion is found by the

validation tests that the pre-existing sediment flux measurement system performs well when the concentration is not very high (usually the errors can be within 10% or even smaller), while it will break down when the concentration goes higher. By comparing the measured masses in different inspection lines, the system is considered as highly reliable when the concentration is not high. The main reason for failure is the inability of velocity analysis due to the missing of the traceable pattern when concentration goes higher (e.g. Fig. 2-13(c)). The factor of light attenuation of 2.5 can be regarded as the measurement limit of the pre-existing system. When the light attenuation exceeds 2.5, precise velocity result is difficult to be obtained even using large interrogation window or other post-processing methods for PIV analysis.

Measurement range narrows down along with the increase in the path length. In the section of concentration calibration, it has been indicated that the relationship between concentration and light attenuation is not always linear. The relation curve levels off after the sediment concentration reaches a critical value. This critical value decays with the increase of path length, which leads to the decrease in measurable range of the sediment concentration. Moreover, because of the short distance between the light source and sidewall of the flume in the case of small path length, traceable patterns disappear in a higher critical concentration than large path lengths. The pre-existing sediment flux measurement system turns to be unstable when the path lengths are too large (e.g. l = 4.0 cm). One reason is that the large path length makes the traceable patterns disappear in a very low concentration. Another reason is that the flow is significantly turbulent when a large bulk of sands falls into the flume in that case leading to difficulties in the velocity analysis.

In summary, the pre-existing sediment concentration measurement system performs well in low concentration conditions with high accuracy and reliability. The measurement system cannot work for highly concentrated sand water flows. Light attenuation of 2.5 can be used as an indicator of the measurement limit. Measurement range decays with the increase in path length. Large path length is not suggested for the pre-existing measurement system.

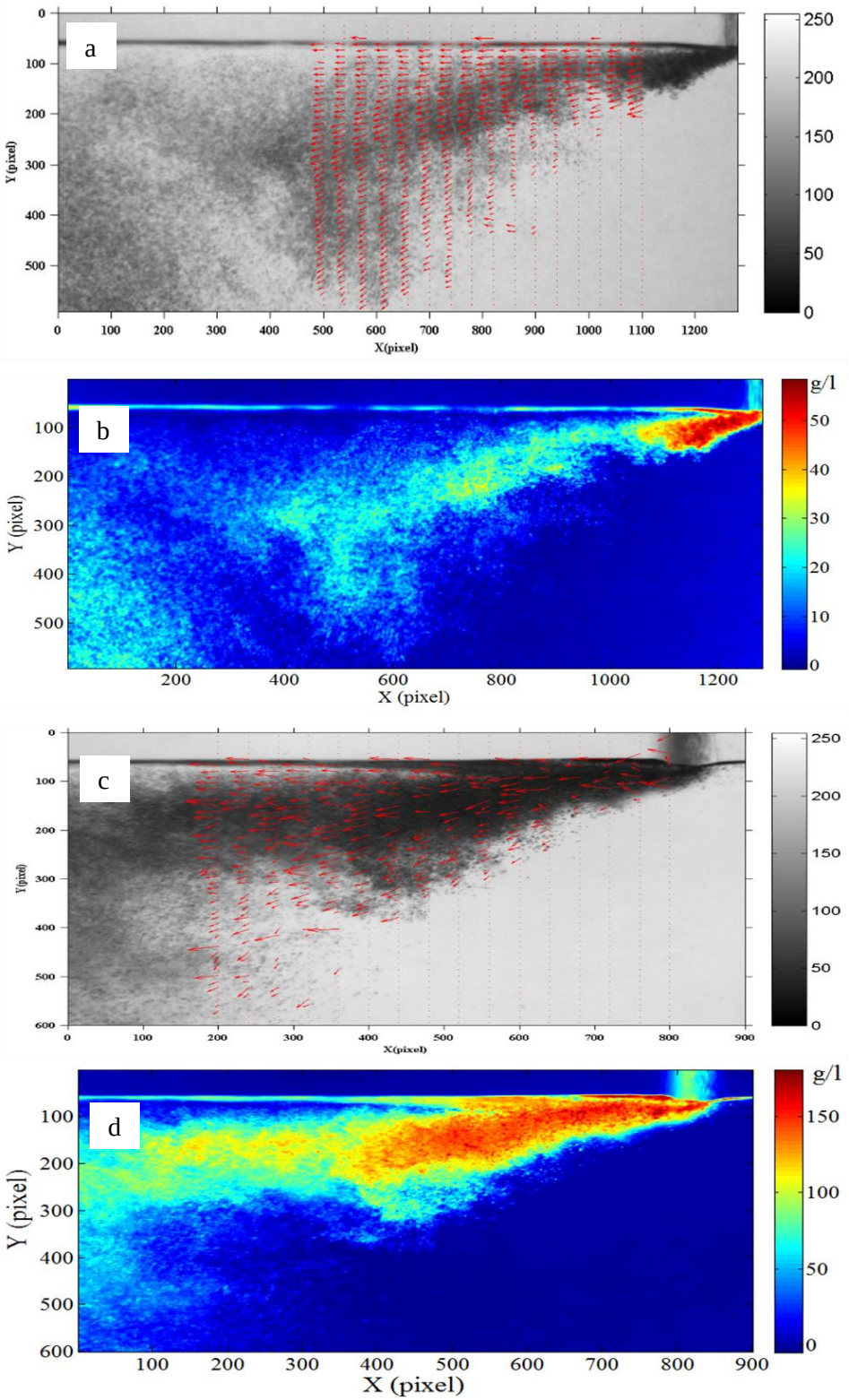

Figure 2-12. Example results of velocity (a, c) and concentration (b, d) distribution in the verification tests of the pre-existing measurement system (a, b: low concentration condition; c, d: high concentration condition)

Table 2-3. Verification test results of the pre-existing sediment flux measurement system

Path length (cm)	Input mass (g)	Inspection line									
		1		2		3		4		5	
		Measured mass	Error(%)	Measured mass	Error(%)	Measured mass	Error(%)	Measured mass	Error(%)	Measured mass	Error(%)
1	4.48	4.62	3.19	4.66	3.91	4.59	2.46	4.67	4.17	4.67	4.17
	5.11	5.35	4.76	5.36	4.97	5.21	2.02	5.28	3.32	5.32	4.10
	5.28	5.35	1.42	5.37	1.75	5.57	5.42	5.54	4.89	5.37	1.61
	5.6	5.77	3.07	5.71	2.05	5.89	5.18	5.8	3.60	5.81	3.82
	6.38	6.59	3.22	6.66	4.33	6.62	3.76	6.58	3.07	6.6	3.43
	12.1	10.03	-17.19	9.82	-18.93	9.64	-20.41	9.91	-18.18	10.12	-16.45
1.5	7.12	7.25	1.81	7.24	1.64	7.28	2.23	7.31	2.72	7.22	1.42
	7.74	7.97	2.94	7.67	-0.91	7.49	-3.25	7.68	-0.74	7.73	-0.17
	8.33	8.5	2.08	8.63	3.55	8.62	3.49	8.66	3.99	8.62	3.52
	8.62	8.43	-2.23	8.5	-1.36	8.8	2.12	8.56	0.71	8.35	-3.15
	10.32	10.71	3.78	10.78	4.47	10.68	3.53	10.8	4.68	10.75	4.14
	15.42	12.13	-21.34	12.04	-21.92	11.03	-28.47	12.44	-19.33	11.57	-24.97
2.0	4.38	4.64	3.00	4.66	6.49	4.66	6.49	4.74	8.21	4.56	4.18
	4.45	4.69	5.43	4.85	8.98	4.76	7.03	4.78	7.38	4.84	8.77
	6.1	6.41	5.07	6.14	0.69	6.4	4.85	6.12	0.41	6.13	0.44
	6.36	6.49	2.04	6.73	5.82	6.65	4.53	6.72	5.64	6.6	3.79
	9.93	7.41	-25.38	8.02	-19.23	7.37	-25.78	7.11	-28.40	7.6	-23.46
	12.09	9.7	-19.77	8.72	-27.87	10.17	-15.88	9.64	-20.26	10.32	-14.64

Table 2-3 (continued). Verification test results of the pre-existing sediment flux measurement system

Path length (cm)	Input mass (g)	Inspection line									
		1		2		3		4		5	
		Measured mass	Error(%)	Measured mass	Error(%)	Measured mass	Error(%)	Measured mass	Error(%)	Measured mass	Error(%)
3.0	6.58	7.16	8.77	6.85	4.08	6.88	4.59	7.1	7.94	6.98	6.06
	7.13	6.85	-3.88	6.91	-3.05	7.75	8.71	7.35	3.10	7.02	-1.52
	7.45	7.54	1.24	7.61	2.11	7.59	1.88	7.54	1.18	7.51	0.77
	7.92	8.4	6.10	8.39	5.93	8.46	6.83	8.49	7.19	8.51	7.51
	13.41	11.81	-12.00	11.67	-13.04	10.62	-20.86	10.68	-20.42	12.52	-6.71
	19.61	16.11	-17.85	15.81	-19.38	15.93	-18.77	16.85	-14.07	15.98	-18.51
4.0	8.12	8.56	5.36	8.43	3.82	8.7	-0.68	8.1	-0.21	8.58	5.68
	9.4	11.2	19.15	11.19	19.05	11.66	24.01	11.72	25.03	11.75	24.97
	11.36	11.56	1.77	12.12	6.65	10.32	-9.19	10.52	-7.16	11.62	2.31
	13.8	14.02	1.59	14.9	7.99	14.65	6.16	14.15	2.53	14.62	5.94
	14.2	13.15	-4.20	15.06	6.05	14.74	3.81	15.06	6.04	14.91	5.04
	19.13	17.31	-9.51	16.4	-14.29	15.3	-20.02	15.62	-18.33	17.34	-9.36
5.0	11.76	14.3	21.60	15.21	29.34	13.84	17.69	13.36	13.61	14.53	23.54
	14.22	16.28	14.49	10.32	-27.43	12.03	-15.40	11.24	-20.96	12.2	-14.19
	14.3	12.35	-13.64	16.36	14.41	10.38	-27.41	10.78	-24.61	10.64	-25.63
	15.37	13.28	-13.64	16.36	14.41	10.38	-27.41	10.78	-24.61	10.64	-25.63
	15.84	13.28	-13.79	12.24	-20.36	12.58	-18.12	13.32	-13.33	13.11	-14.74
	17.07	19.23	12.65	13.54	-20.68	19.33	13.24	20.21	18.39	15.35	-10.09

2.4.3 Verification of the improved sediment flux measurement system

Description of the improved sediment flux measurement system is introduced in Sect. 2.3. Since the improved sediment flux measurement system is developed for estimating sediment flux of high concentration, a specially designed verification test was conducted to evaluate its capability.

Fig. 2-13 shows the side view of the verification test configuration for the improved sediment flux measurement system. The EL-sheet was attached to a transparent tank which is made of acrylic plates. The width of the transparent flume was 1.5 cm, which is regarded as a suitable path length for the measurement system. Water in the tank was initially steady and sands were dropped into the tank through a simple dropping device. The dropping device was specially designed which allows a large bulk of sands fall into the tank uniformly perpendicular to the EL-sheet within a short time to generate large sediment concentrations. Silica sands with a medium diameter of 0.16 mm were used in the verification tests. The high-speed camera was set at an fps of 400 to record the movement of the sands and the stroboscope was synchronized at a frequency of 200 Hz by the digital delay generator. The position of the stroboscope was carefully adjusted in order to obtain high-quality PIV recording. Since the frequency of the stroboscope was half of the high-speed camera fps, normal (back-light only) and combined-illuminated images were alternately obtained at the same rate of 200 Hz. The preferences (aperture, shutter speed) of the high-speed camera were also carefully adjusted to be same with the previous calibration experiment so that additional calibration of sediment concentration was not necessary. Normal images were used for concentration measurement based on the calibration result and both of the two sets recorded images were employed for velocity analysis. This is for the purpose of confirming that the stroboscope can work well as expected. Similar to the former verification tests, three inspection lines were set to calculate the sediment flux. As the net amount of input sand was known, the performance of the improved system could be evaluated by comparing the measured mass and actual input mass. The verification tests were carried out for four cases with different amount of input sand.

PIV analysis was carried out similar with that in Sect. 2.4.2 except that the inspection lines are horizontal in the present verification tests. Examples of the measured result of instantaneous velocity and concentration are presented in Fig. 2-14. It is obvious that velocity field measured from combined-illuminated images is better than those from normal images. It can be confirmed that the stroboscope is capable of forming traceable patterns for operating PIV analysis by enlarging the light intensity range in the cases of dense sediment concentration (Fig. 2-4).

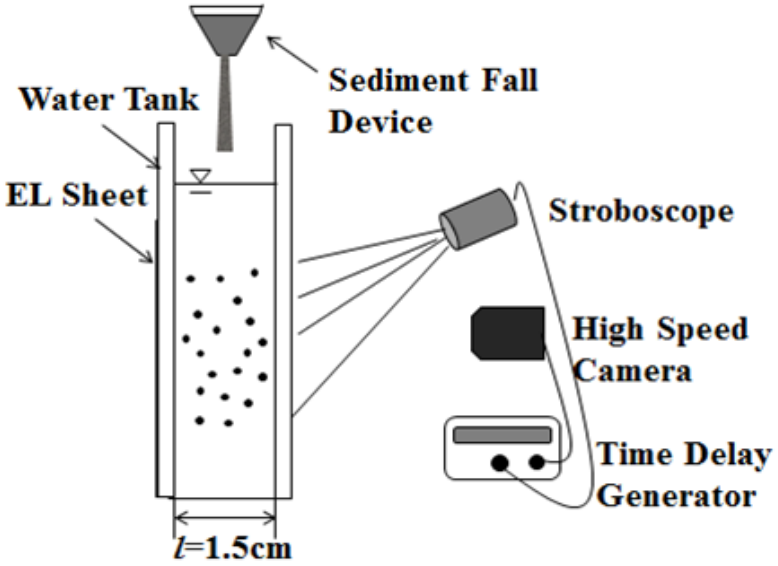

Figure 2-13. Experimental set-up for the improved sediment flux measurement system

It should be noted that sediment concentration around the boundary (between the bulk of sands and pure water) is low in the verification tests. Sand particles in this area are easily disappeared from the recorded images due to the strong illumination by the stroboscope, such as the locations indicated by circles in Fig. 2-14. Therefore, velocity measurement is impossible in these areas because of lack of image pattern for PIV analysis. In contrast, PIV analysis shows good capability in the boundary of the normal images. This is similar to the pre-existing sediment flux measurement system for measuring the velocity of moderate sediment concentration. Therefore, a post-processing method was developed to complement the velocity information in the

boundary of the combined-illuminated images. The missing velocity vectors in the velocity field measured from the combined-illuminated images were recovered by those measured from adjacent normal images of same interrogation windows. The replacement was automatically done based on the light attenuation. Since the recorded images were in gray-scale, and intensity values range from 0 (black) to 255 (white), a critical value of detected light intensity was set to recognize the particle disappearance in the boundary of the combined-illuminated images. In the present case, we found that it is appropriate to set the critical value at 235 (Wu et al., 2014). Once the mean light intensity value of an interrogation window exceeds the critical value, traceable patterns would disappear in the corresponding areas and the combined-illuminated images are regarded as not suitable for PIV analysis in these regions. After recognizing these interrogation windows where traceable image patterns disappear, the replacement of velocity vectors is carried out. By using this method, data completeness is guaranteed and measurement error is avoided.

Three inspection lines were set to measure the sediment transport load. Since all of the input sand passed through the inspection lines, net sediment flux measured in each inspection line should be same among each other and same with the actual input mass if the improved measurement system works properly. Sediment concentration and velocity are measured at an interval of 12 pixels (about 0.1 cm) along each inspection line. Both velocity results measured from normal and combined-illuminated images (after complementing of velocity vectors) were substituted into Eq. 2-7 for calculating sediment transport load to evaluate the performance of the improved measurement system.

The results of verification tests are presented in Table 2-4. The two columns at the right of the table show the difference of measured sediment load over actual input amount in each inspection line. The measured sediment mass from velocities estimated by combined-illuminated images are more close to the actual input mass than those by normal images, as all of their errors are less than 10%. Moreover, the measured masses calculated from combined-illuminated images at each inspection line are close to each other in the same case, indicating that concentration and velocity measurements are pretty accurate and reliable. Maximum and mean values of sediment concentration and

light attenuation for each inspection line in every case are also presented in Table 2-4. It is found that the improved measurement system performed well beyond the measurement limit (light attenuation of 2.5) of the previous system. The maximum and mean values of light attenuation are 4.47 and 3.12 respectively which means that the improved measurement system successfully breaks the limitation of the pre-existing system by using the stroboscope, and the measurement range is expanded greatly. In the verification tests, the maximum value of measurable sediment concentration could reach as high as 193 g/L for the path length of 1.5 cm and it is not the measurement limit of the improved system.

2.4.4 Conclusion and discussion

The verification tests have shown that the stroboscope is capable of illuminating the highly concentrated sand water flow well by careful position adjustment. Clear traceable image pattern could be captured by the high-speed camera which is essential for PIV analysis. By integrating the velocity information in regions of dense sediment concentration measured from combined-illuminated images and in regions of low sediment concentration measured from normal images, a whole field of transport velocity could be obtained. Thus, quantification of sediment flux in the case of very dense sediment concentration can be achieved which is not possible in the pre-existing measurement system.

The improved measurement system is flexible since it could be used in flow conditions with a wide range of sediment concentration. When sediment concentration is not large, the normal images are enough to quantify sediment flux. On the contrary, when sediment concentration is large, combined-illuminated images might be suitable for PIV analysis. In many cases, distribution of sediment concentration is significantly inhomogeneous in the recorded images, thus the combinational use of the velocity information from both of the two types of images is necessary for velocity measurement. Moreover, if the concentration varies significantly during a wave period, alternatively use of the normal and combined-illuminated images for PIV analysis is optimal. The selection of the two types of the image for velocity evaluation should be depended on the detailed practical situations (case by case). This is also the reason why combined

illumination is essential in the improve sediment flux measurement system. Liu and Sato (2005) confirmed that only using stroboscope cannot measure the sediment concentration. On the other hand, using stronger backlight sources probably able to produce clear image pattern in high concentration conditions and extend the measurement range of the pre-existing system but it will result in the missing of small concentration band.

Transport velocity can be achieved no matter how large the sediment concentration is with the assistance of the stroboscope. Verification tests were also carried out for the extreme condition to evaluate the function of the stroboscope. The transparent container filled with sands (no water, to make a 100% concentration) to half of its volume was shaken slowly. The high-speed camera was used to record the movement of the sands under the illumination of the stroboscope. PIV analysis shows that accurate velocity can be obtained even in this kind of extreme conditions. Therefore, the capability of the improved sediment flux measurement system is limited by the valid range of the Beer-Lambert law because linearity between the sediment concentration and light attenuation no longer exists when sediment concentration exceeds a critical value (explained in Sect. 2.4.1). small path length and high incident light intensity give a large measurement range. For the case of path length equals to 1.0 cm in the calibration tests, the valid range of the Beer-Lambert law is over 300 g/L which is sufficient for most sediment transport experiments (except for some exceptional cases with large sheet flow transport).

The temporal resolution of the improved sediment flux measurement system is determined by the frequency of the high-speed camera and the stroboscope. Modern high-speed camera usually has a maximum fps of several thousand hertz, so the temporal resolution of the measurement system is mainly limited by the stroboscope. The frequency of the high-speed camera and the stroboscope were 200 Hz and 100 Hz respectively in the verification tests. It should be noted that velocities in the present verification tests are not so large that the maximum frequency (100 Hz) of the stroboscope is enough for PIV analysis. While in some strong flow conditions, velocity usually turns to be very high. The maximum frequency of the stroboscope might be insufficient for PIV recording as has been explained in Sect. 2.2.2. Therefore,

stroboscope of much higher frequency is necessary when measuring sediment transport in strong flow conditions.

Spatial resolution of the improved sediment flux measurement system depends on the setup of the high-speed camera. If the high-speed camera is installed close to the target flow, capture area is small but the magnification is large. It means that measurement region is small while spatial resolution of the measurement is improved. On the contrary, if the high-speed camera is installed far away from the target flow, the spatial resolution would be decreased compensated by a large measurement area. Balance of the measurement area and spatial resolution relies on the detailed experimental purpose.

The improved sediment flux measurement system needs to be employed in the dark without any other light source (e.g. the EL-sheet and stroboscope should be the only light sources). Light reflection caused by the sidewall is not significant in the present case and it does not influence the measurement system seriously.

Table 2-4. Verification results of the improved sediment flux measurement system

Case	Input mass (g)	Inspection line	Sediment concentration (g/L)		Light attenuation		Error without stroboscope (%)	Error with stroboscope (%)
			Max	Ave.	Max	Ave.		
1	13.09	a	193.20	136.61	4.47	3.12	-34.6	-5.2
		b	184.37	135.78	4.26	3.11	-27.0	-5.6
		c	178.92	130.02	4.15	3.01	-23.1	-7.4
2	18.04	a	176.32	105.45	4.13	2.98	-41.6	-4.7
		b	175.20	103.24	4.11	2.76	-35.7	-2.4
		c	170.01	98.35	4.04	2.35	-22.2	-8.9
3	18.06	a	149.06	76.79	3.45	1.75	-13.9	-2.6
		b	149.56	73.22	3.45	1.67	-16.4	0.8
		c	145.46	70.53	3.36	1.60	-15.8	-4.0
4	19.32	a	179.68	111.33	4.47	2.69	-37.1	-7.8
		b	177.27	105.76	4.23	2.56	-26.6	-5.5
		c	171.11	101.08	4.15	2.45	-20.8	-5.2

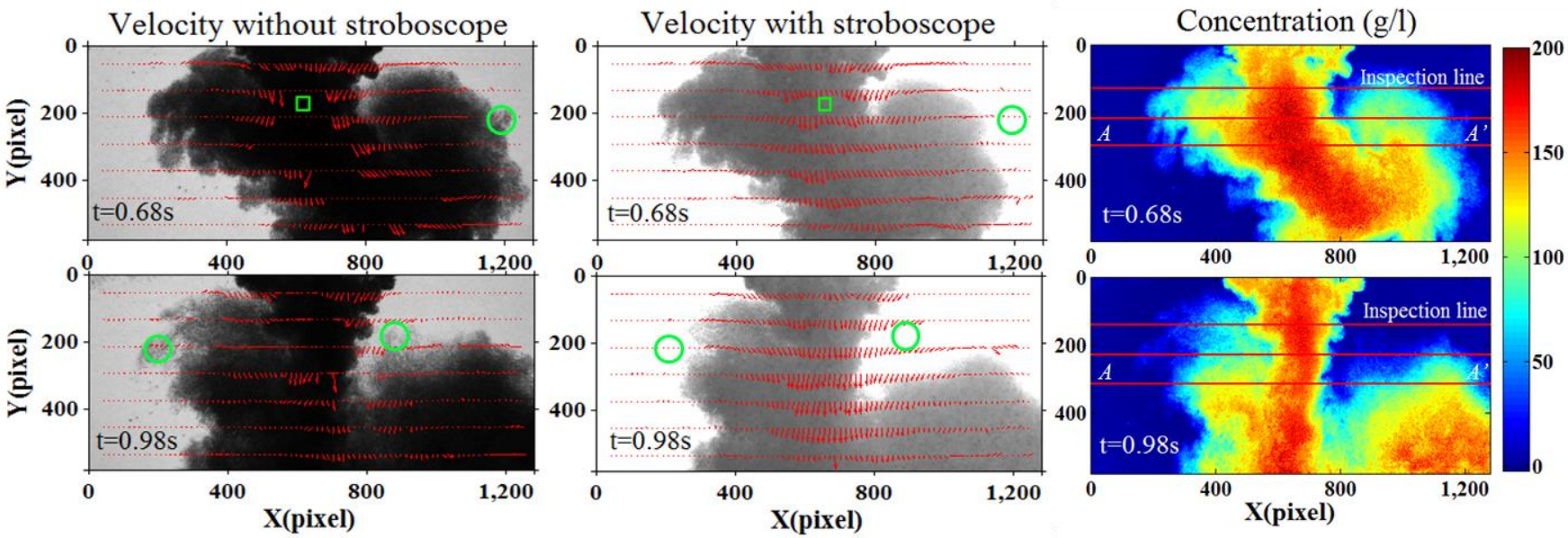

Figure 2-14. Experimental result of velocity and concentration distribution measured by the improved sediment flux measurement system

Chapter 3 Laboratory Experiment of Sediment Transport in the Swash Zone

3.1 Introduction

Field experiments in terms of the swash zone have resulted in a reasonable and valuable understanding of the swash zone processes (Butt and Russell, 2000; Longo et al., 2002; Elfrink and Baldock, 2002; Masselink and Puleo, 2006; Chardón-Maldonado et al., 2016). However, the complexity of processes in the real field makes the measurements difficult and uncontrolled. As for the large-scale wave flume experiment, it is also difficult to isolate and quantify the fundamental processes for investigating the parameters of interest. An alternative approach for studying the swash zone is to generate the dam-break flow where the gate of a reservoir filling of water is suddenly released leading to a bore propagating downstream and climbing on a sloping bed. The dam-break generated flow produces a single, repeatable and large-scale swash event with hydrodynamics could be comparable to that in the real field. Therefore, the dam-break swash flow avoids many complexities in the field and wave flume such as the low-frequency oscillation, swash-swash/wave interaction. This reduction in complexity along with high-repeatability characteristic allows detailed investigation of the fundamental process occurring in the swash zone. Furthermore, dam-break swash experiments provide benchmark databases for validating and developing numerical models regard to hydro- and sediment dynamics in the swash zone. Barnes et al. (2009) used a dam-break set-up to directly measure intra-swash bed shear stress by using a shear plate. O'Donoghue et al. (2010) and Kikkert et al. (2012, 2013) carried out a series of dam-break experiments to study the detailed hydrodynamics of swash over immobile, impermeable/permeable beaches of varying surface roughness to measure hydrodynamics in the swash zone by PIV and LIF (Laser induced fluorescence). Previous dam-break swash experiments involving a mobile sediment beach are limited to Othman et al. (2014) and O'Donoghue et al. (2016). Othman et al. (2014) used a sloping dam-break apparatus to measure swash uprush sediment transport at the end of a truncated slope, their particular focus being on the influence of grain size and pressure gradient on sediment transport, rather than the detailed intra-swash sediment flux.

O'Donoghue et al. (2016) used the same dam-break facility as used for these previous experiments (Kikkert et al. (2012, 2013)) to measure the intra-swash sediment flux for well-controlled swash conditions. Sediment flux in their experiment was only resolved as depth-integrated and it is measured by lifting a trap at different times for repeats of the swash events and measuring the mass of sediment collected over the time interval.

Sediment flux over the mobile sand bed is not resolved well so far. Even though instrumentation for swash zone sediment transport is promoted rapidly in recent years, a detailed structure of vertical distribution of sediment flux in the swash zone is not yet available either in the field campaigns or laboratory experiments making the quantification of sediment transport difficult. Moreover, velocity structure in the vicinity of the sand bed (e.g. within the sheet flow layer) is not well resolved. Previous studies using the logarithmic model to evaluate the bed shear stress seems questionable since the velocity very close to the mobile bed is not truly captured. Precise measurement or estimation of roughness and friction coefficient over the real sand bed in the swash zone is very few (if is not non-existence).

This chapter describes a laboratory experiment conducted over mobile fine sand bed in the swash zone with a special focus on intra-swash sediment dynamics. The image-analysis-based sediment flux measurement system developed in Chapter 2 is employed in the experiment for quantifying the sediment transport process. Detailed experimental setup and methodology will be introduced in the following and experimental results will be shown in Chapter 4.

3.2 Experimental setup and instrumentation

The experiments were carried out in a modified open channel flume at Tokyo University of Marine Science and Technology. It is a 7.1 m long, 0.3 m wide and 0.7 high, glass-sided flume with a water reservoir built into one end. The reservoir is fronted by a gate which can be raised to generate a large plunging wave leading to a bore which propagates towards an impermeable slope located downstream. The slope is a 1/6 transparent inclined bottom made of acrylics with a thickness of 8.0 mm. The slope is mounted to the side-wall of the flume to increase its rigidity. The dimension of the flume is shown in Fig. 3-1. The exit of the reservoir is streamlined to ensure a

smooth transition for the flow from the reservoir to the flume. A sand layer of 3.0 cm depth is covered over the slope to make a moveable bed. Sands used in the experiment are silica sands with a medium diameter of 0.16 mm.

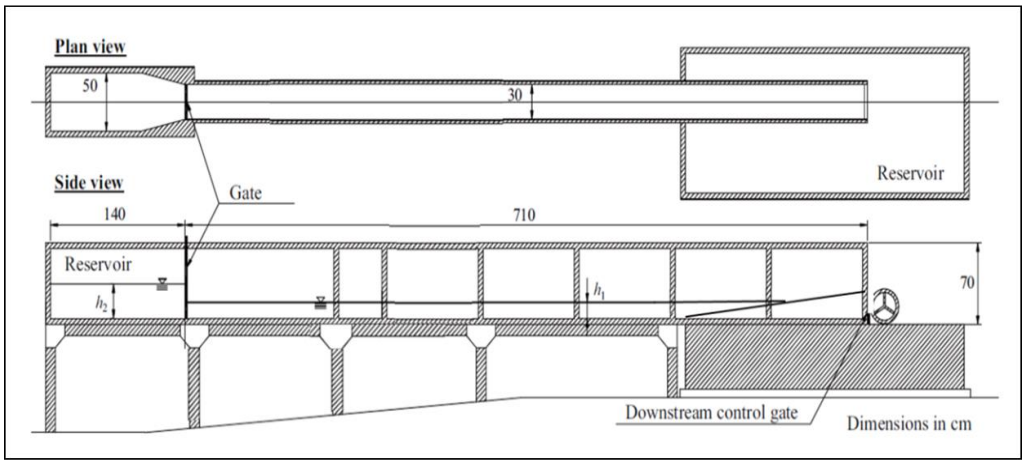

Figure 3-1. Sketch of the experimental flume

Two laser distance meters were employed to measure the evolution of the bed profile before and after each swash event. The horizontal sensor (Jenoptik, LDM41/42) was fixed above the flume to measure the position of the vertical sensor. The vertical sensor (Keyence, LK-G505) was fixed on a trolley which can be slide on the track of the flume. Both of the two sensors are single point distance meter. Following the moving of the trolley, the vertical laser distance meter can measure the distance between the laser head and the sand bed. Thus, the bed form can be determined through the two laser distance meters.

The improved sediment flux measurement system was employed in the experiment to measure hydro- and sediment dynamics in the swash zone. A 20×15 cm^2 EL-sheet was set upon the sand bed 30 cm from the toe of the slope. The EL-sheet was sealed in two acrylic plates (1.0 mm thickness) in order to protect it from the water flow and keep it completely normal to the sand bed. The bottom of the EL-sheet was stick to the acrylic slope bottom, which means that a part of the EL-sheet was under the sand bed so that sediment transport close to the bed can be observed. Distance between the EL-sheet and

the side wall of the flume was 1.5 cm, which means the path length in current setting is 1.5 cm. A CMOS high-speed camera (IDT Inc., M3) mounted with a prime lens (Nikkor, 50mm f/1.2) was set to record the movement of the sediments. It was rotated to be aligned with the 1/6 slope so that the bed-normal and the bed-parallel velocities can be measured. The minimum focal distance of the lens was 50 cm and it does not meet the measurement requirement since large magnification was necessary as one of the objectives of the experiment was to investigate the bottom boundary layer. Therefore, an auto extension ring (Nikon PK-11A) was mounted between the prime lens and the high-speed camera to enable the prime lens to focus closer than its normal set minimum focusing distance. Thus, the high-speed camera was installed 30 cm from the side wall of the flume which gives a resolution parameter λ = 66 μm/pixel. The size of the recorded images was 520 × 1000 pixels, corresponding to a roughly 3.47 cm by 6.67 cm captured areas. The high-speed camera was controlled by specified software named Motion Studio developed by IDT Corporation. As mentioned above, PIV requires a short time interval between two consecutive images when the flow velocity is large. In the bore-driven swash zone, the flow is significantly turbulent, so the stroboscope used in the verification tests cannot fulfill the requirement. Therefore, a new stroboscope was applied in the present laboratory study. It was a double lamp stroboscope (SA-100B-W) designed by Nissin Electronic Corporation. Each lamp has a maximum flash frequency of 120 Hz, while the time interval between the flash of two lamps can be controlled by external signal. After careful position adjustment of the two lamps, illumination effect between them can be very similar, which ensures velocity analysis will not be influenced by the different illumination effect of the two lamps. The photo of the flume and schematic of the experimental setup are shown in Fig. 3-2.

In the present experiments, the fps of the high-speed camera was set in 1000 and the frequency of the two lamps was 100 Hz. The time interval between two lamps was controlled in 1 μs. A digital delay generator (Stanford, DG645) was used in the experiment to accurately trigger and synchronize the measurement system. Thus, there were 2 successive images illuminated by the stroboscope within every 10 frames.

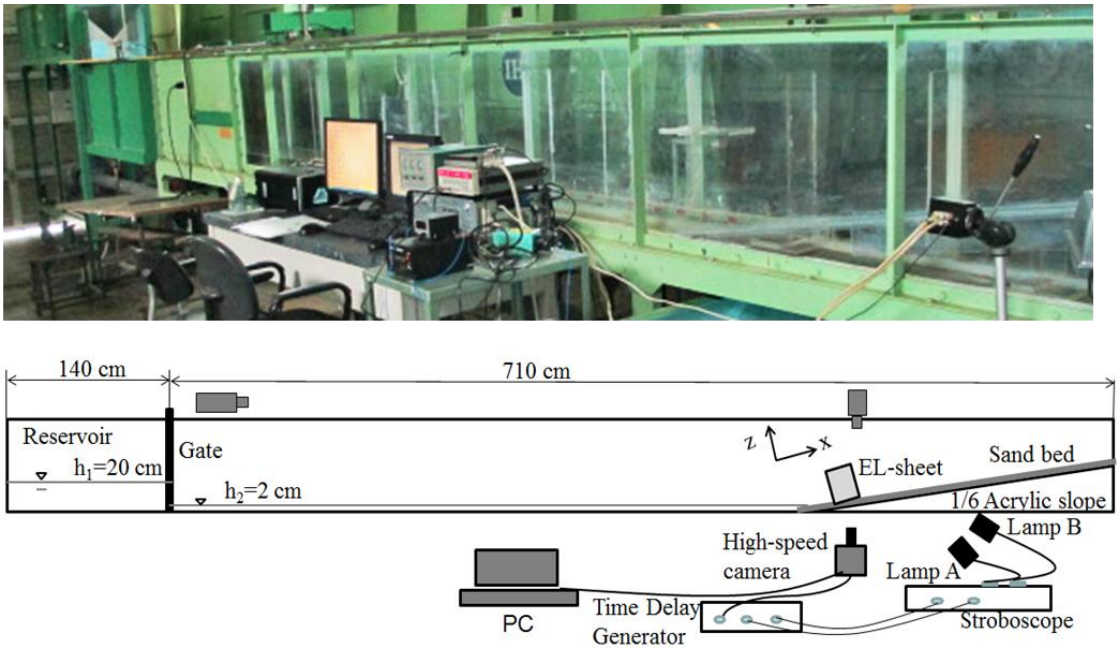

Figure 3-2. Photo of the laboratory flume and experimental set-up

3.3 Experimental conditions and measurement procedures

The experiments were conducted for one initial condition only: a water depth in the reservoir of 20.0 cm and a water depth in front of the gate of 2.0 cm. The origin of the *x*-*z* coordinate system is located at the initial shoreline position, located 3.2 m from the reservoir gate: the *x*-axis is parallel to the original sand bed and is positive shoreward; the *z*-axis is perpendicular to the slope. The corresponding velocity components are *u* and *w* respectively. Measurements were triggered when the dam-break flow reaches the toe of the slope. After installing all of the instruments appropriately, experiments were conducted at the following procedures:

(1) The gate was closed and the water aspirator began to pump water from the flume to the reservoir. Because the sealing between the gate and the reservoir was not good enough, there was water leaking to the flume. While keeping the water aspirator open, water leaking from the reservoir and pumping back to the reservoir would reach equilibrium. Since the total amount of water was carefully calculated before the

experiments, the water depth in the reservoir and flume would be 20.0 cm and 2.0 cm respectively at last.

(2) Keeping the pump open, laser distance meters started to work for measuring the initial bed form before the bore driven flow.

(3) The pump and gate were raised simultaneously at a high speed by hand to generate a dam-break flow. Because the dam-break flow propagated about 3 seconds before reaching the slope, the high-speed camera was set to record images 3 s after the gate was raised. The high-speed camera and stroboscope were synchronized by the digital delay generator with the aforementioned setup.

(4) After the waves rushing down from the sand bed to the reservoir, a temporary baffle wall was manually lowed into the flume to compartmentalize the flume for preventing the sand bed from scouring by the following seiches.

(5) The high-speed camera and stroboscope stopped to work and recorded images would be saved to a hard disk for further analysis.

These five steps were repeated for 20 times in order to investigate the bed form evolution after multiple dam-break flows. One dam-break flow running up and down is defined as a swash event; therefore, we have 20 swash events in total. The dam-break flow running up and down over the sand bed is a ‘pure’ process since there is no interaction between two flows. Example images of one swash event recorded by the high-speed camera are shown in Fig. 3-3. The flow firstly appeared in the image is defined as $t = 0$.

3.4 General description of the dam-break flow

The dam-break flow was broken during the propagation to the sand bed. When the flow firstly reached the measurement region (appeared in the image), it is significantly turbulent. And the water flow was mixed with a lot of air bubbles and solid sand particles to form a three-phase flow. The air bubbles went up rapidly and disappeared in the water surface leaving the flow as a sand-water mixture for most of the phases. This process is pretty short and usually less than 0.1 s. During the flow running up and down

over the sand bed, air bubbles emerged occasionally and the majority of them were found in the uprush.

The water surface of the dam-break flow in the initial uprush is uneven between the EL-sheet and the side wall due to the strong turbulent characteristic. When the water depth decreases, some water leaves on the EL-sheet generating a ‘dark pattern’ in the recorded images, which is particularly obvious in the late backwash (Fig. 3-3). The maximum water depth of the dam-break flow in the measurement region is smaller than the vertical measurement range making the investigation of the whole water column becomes possible. Since the gate was raised by hand in the experiment, so the dam-break flows were not absolutely same. The total duration of the dam-break flow in the measurement region was around 2.4 s with a difference of ±0.2 s among each swash events.

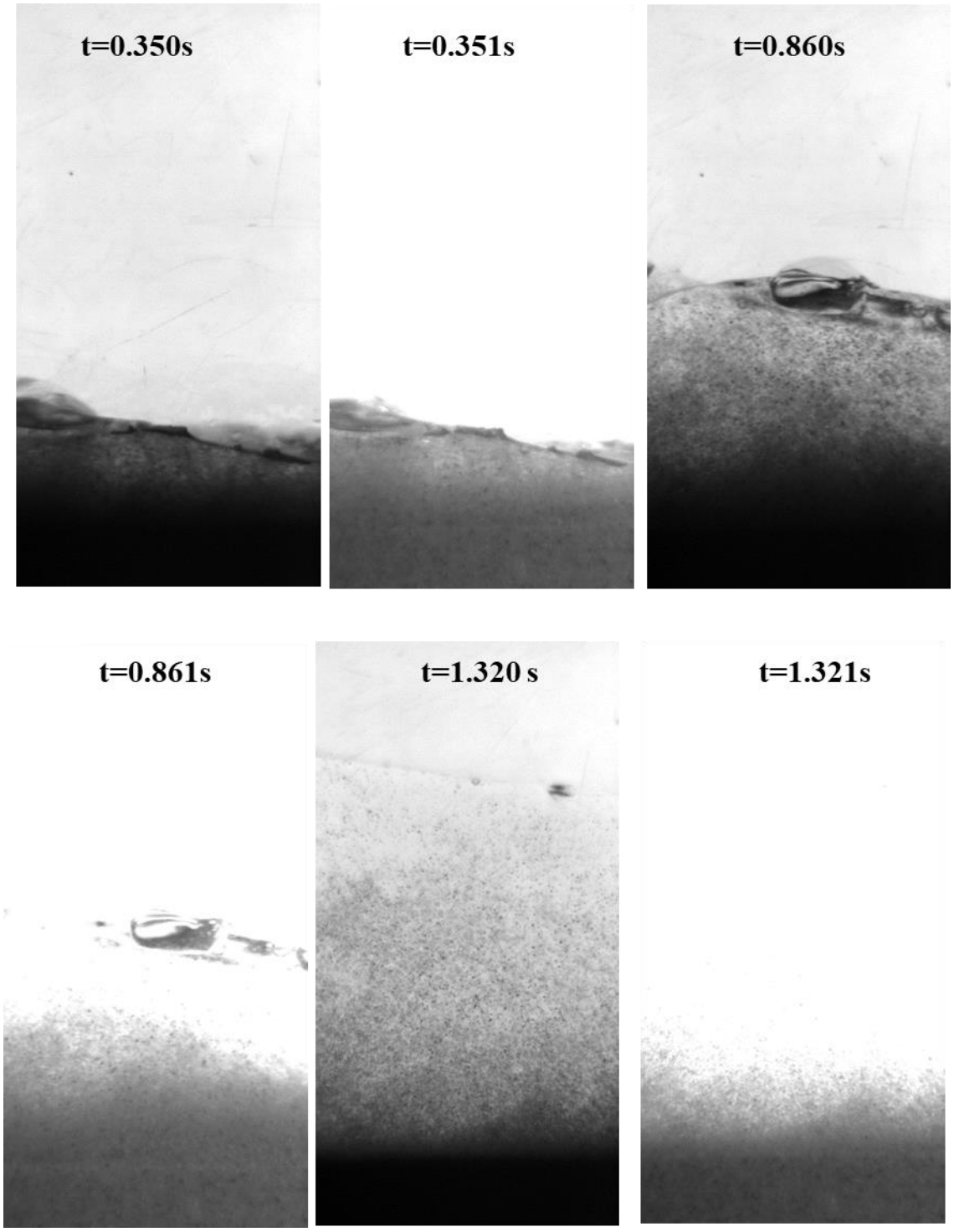

Figure 3-3. Example images recorded by the high-speed camera

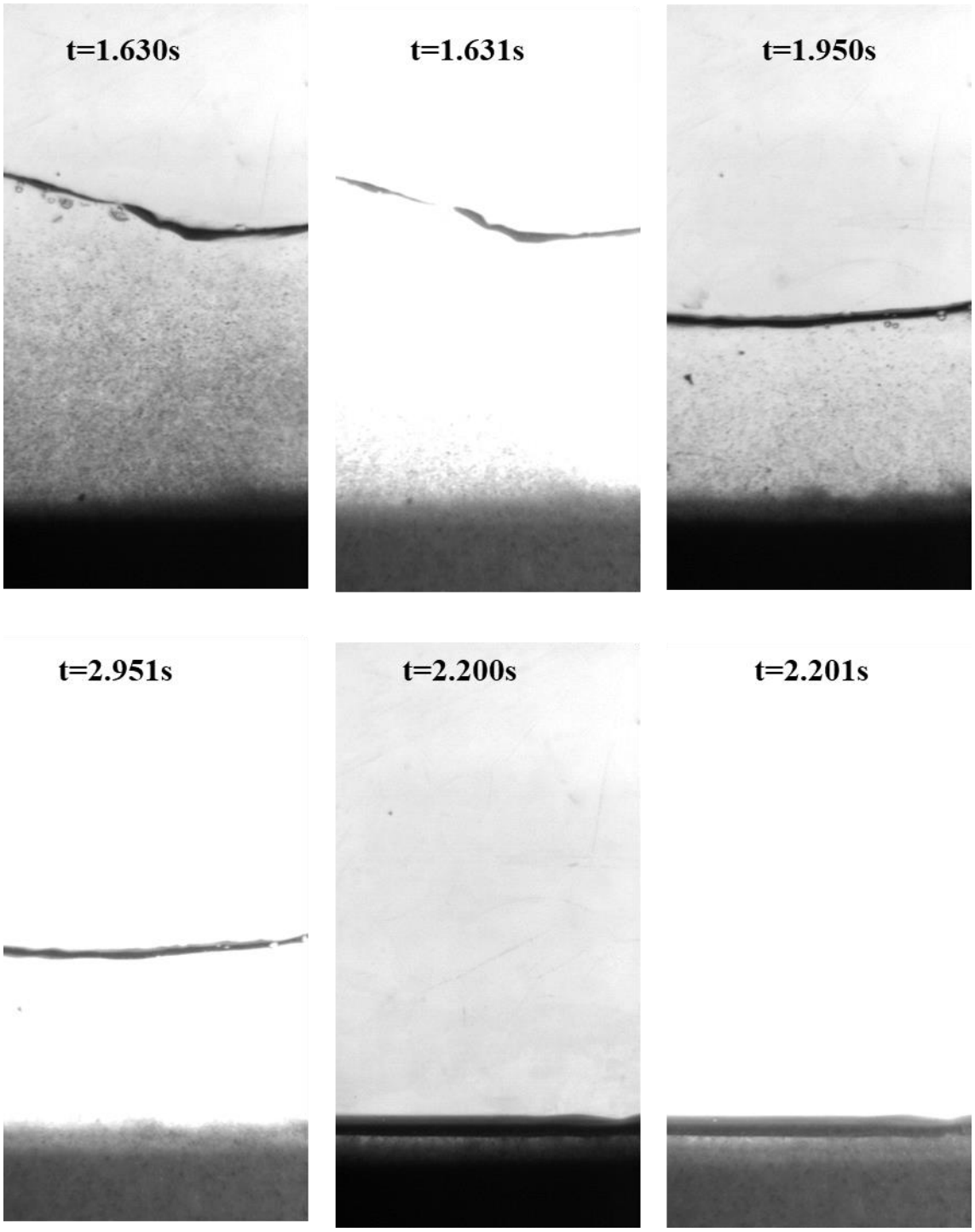

Figure 3-3 (continued). Example images recorded by the high-speed camera

3.5 Velocity measurement

3.5.1 Frequency domain based correlation

In the verification tests, the displacements of the interrogation windows were determined by the best match between two images in a statistical sense (direct cross-correlation). This method is accurate but the computation load is quite large since each interrogation window needs to traverse the search window for conducting cross-correlation. The computation load has an exponential increase with the increase both of the search window and interrogation window. Since measurement resolution (both spatial and temporal) is vital for the further analysis of the bottom boundary layer and sediment transport, the computation load would be tremendously large if the direct cross-correlation still being selected.

On the other hand, the experimental conditions are much more complex than those of the verification tests. The transport velocity varies from the maximum (positive) in the initial uprush to zero in the flow reversal and again maximum (negative) in the late backwash. Moreover, sediment concentration changes significantly not only from uprush to backwash but also in the vertical direction of the measurement region. All of these make the PIV analysis much more sophisticated and difficult. Using a single step direct cross-correlation in the PIV analysis is considered not reasonable and sufficient for accurate velocity measurement. Therefore, a specially designed Matlab-based algorithm was employed to do the velocity evaluation.

Frequency domain based correlation was used in replace of the direct cross-correlation. Principle of the frequency domain based correlation is that the cross-correlation of two functions is equivalent of a complex conjugate multiplication of their Fourier transforms based on the correlation theorem,

$$R \Leftrightarrow \hat{G} \cdot \widehat{G'}^{*} \tag{3-1}$$

where, $\hat{G}$ and $\widehat{G'}$are the Fourier transforms of the functions (interrogation windows) G and G', respectively. in practice the Fourier transform is efficiently implemented for

discrete data using the fast Fourier transform (FFT) which reduces the compotation load from O[N^2] operations to O[$N\log_2 N$] operations (N^2 is the size of the interrogation widow in the unit of pixel). The tedious two-dimensional direct cross-correlation can be reduced to computing two two-dimensional FFT's on equal sized samples of the image followed by a complex-conjugate multiplication of the resulting Fourier coefficients. These are then inversely Fourier transformed to produce the actual cross-correlation plane which has the same spatial dimensions. Thus the computation load could be decreased from O[N^4] operations to O[$N^2\log_2 N$] operations. Moreover, since the real part of the Fourier transform is symmetric, the computation efficiency can increase even further. In practice, two real-to-complex, two-dimensional FFTs and one complex-to-real inverse, two dimensional FFT are needed, each of which require approximately half computation time of the standard FFTs (Raffel et al., 2007).

3.5.2 Implementation of PIV

In order to obtain high resolution, high accuracy velocity information, multiple pass interrogation technique with a grid refining schemes was employed in the PIV analysis. Ten inspection lines along the measurement region were selected to evaluate the transport velocity. The distance interval between two adjacent inspection lines was 40 pixels. A large interrogation window (96 × 32 pixels) was first used to do FFT-based correlation on each inspection line. The reason for using rectangle interrogation window instead of square window is that vertical gradient of the transport velocity is significant, especially in the vicinity of the sand bed. Using small window size in the vertical direction could capture more velocity information. Moreover, aliasing of velocity direction easily occurs if the displacement exceeds half of the interrogation window size when using FFT-based correlation due to periodic characteristic of the correlation data (Raffel et al., 2007). The variation of the bed-parallel transport velocity is great, so a large size of interrogation window in the horizontal (bed-parallel) direction could avoid the aliasing. The vertical distance of two adjacent measurement locations on each inspection line was 8 pixels, giving a vertical overlap of 75% in the first iteration. The data yield by the first iteration of correlation was examined and outliers were replaced by the mean value of their neighbors. In the second iteration, a finer interrogation window (96 × 16 pixels) was used to increase the resolution. The vertical distance of

two adjacent measurement locations was 4 pixels in this iteration. On each measurement location, the closest integer displacement result of the first iteration was used to offset the interrogation window in the second iteration. Except for increasing the vertical resolution, this process has an additional function of reducing the aliasing mentioned above. Outlier detection and replacement were also carried out for the results of the second iteration. Since the Fourier transform has the characteristic of periodicity (also noted as circular effect), the correlation estimates are biased. With increasing shifts less data are actually correlated with each other because the periodically continued data of the correlation template makes no contribution to the actual correlation value. Values of the edge of the correlation plane are computed from only the overlapping half of the data. This would introduce systematic errors or will even hide the correlation signal in noise if not handled properly. Therefore, in the third iteration, a modified FFT-based correlation (Ronneberger et al. 1998) was used in order to avoid the bias error in the normal FFT-based correlation,

$$R = \frac{mG \otimes G' - \sum mG \cdot m \otimes G'}{\sqrt{(\sum mG^2 - (\sum mG)^2) \cdot (m \otimes G'^2 - (m \otimes G')^2)}} \tag{3-2}$$

With the definition of a cross correlation operator $\otimes$ as,

$$x \otimes y = \mathrm{FFT}^{-1}(\mathrm{FFT}^{*}(x) \cdot \mathrm{FFT}(y)) \tag{3-3}$$

m is a normalized mask ($\sum m_{ij} = 1$) used to get rid of the circular effect. mG denotes the element by element multiplication of two images,

$$(mG)_{ij} = m_{ij} \cdot G_{ij} \tag{3-5}$$

The main difference between the modified and normal FFT-based correlation is that mean value of the interrogation window is taken into consideration so that the algorithm can return exactly the same result as the direct cross-correlation. Computation load of

the modified approach is double of the normal FFT-based correlation while much smaller than the direct cross-correlation. Setup of the interrogation windows in the third iteration is same with that in the second iteration and window offset was also used similarly with the second iteration. Gaussian peak fit was carried out after the third iteration to improve the measurement resolution to subpixel level.

3.5.3 Velocity composition

With the setup of the instruments, there were 8 normal images and 2 combined-illuminated images recorded by the improved measurement system within every 0.01s. The specially designed multiple pass interrogation algorithm was employed for the 2 combined-illuminated images and another 2 successive normal images for every 0.01s. Fig. 3-4 shows examples of the velocity fields evaluated by the PIV algorithm of several instantaneous swash moments. The results showed that the improved measurement system works well for evaluating transport velocity. In the initial uprush, the stroboscope can illuminate the whole water column well without losing any image pattern since the sediment concentration is very high. Therefore, velocity field from the bottom to the water surface can be measured from the combined-illuminated images, while the normal images can only give velocity result in the upper layers where sediment concentration is not so high. In the middle uprush, sediment concentration in the upper layers was low and lots of image pattern disappeared there due to strong illumination by the stroboscope, so only transport velocity field in the lower water column can be measured from the combined illuminated images. In the contrary, the normal images give good velocity results in the upper layers and fail in the lower water column. During the flow reversal, the stroboscope seems to lose its function since the velocity of the whole water column can be measured from the normal images. In the backwash, the stroboscope only works well in the vicinity of the sand bed while the normal images could give whole velocity field except for a few moments.

From the example results of velocity fields, it is found that for some parts of the water column, both of the normal and combined-illuminated images can give velocity results. A comparison of the magnitude of the velocities in these regions between the two types of the images was carried out to investigate the effect of illumination by the two lamps.

The comparison result shows that differences between them are generally smaller than 5%, and there is no sudden change of transport velocity within this short time interval. Since there is a time difference of 0.002 s between them and the dam-break flow varies significantly, the small differences indicate that illumination of the two lamps has no negative effects on the PIV analysis.

Based on the small differences between the velocities measured from the two pairs of recorded images in every 0.01s, the flow is assumed stable in this short time interval. Thus, transport velocity fields of the whole water column can be obtained by means of compositing the two velocity field. Through trial and error, a critical value of light intensity of 80 was chosen to conduct the velocity composition. When the mean light intensity of the interrogation window in the third iteration of PIV analysis is smaller than 80, velocity vector measured from the combined-illuminated images is selected to form the final velocity field. Otherwise, velocity vector measured from the normal images will be selected. No further outlier detection technique was employed since the velocity vectors were examined in every step of iteration. And data smoothing techniques were not used for the composited velocity fields in order to keep the 'purity' of the data. Examples of combined velocity fields are shown in Fig. 3-5.

3.5.4 Measurement error in the boundary regions

In principle, tracer particles in the interrogation windows must move homogeneously between two illuminations to obtain accurate velocity vector. However, in the present experiment, two boundaries exist in the recorded images where PIV analysis might be influenced. One is the boundary between the sand-water flow and the air. Another one is between the sand-water flow and the unmovable sand bed. Interrogation windows in the vicinity of these two boundary regions might contain a part of sand-water flow and some unmovable image patterns (air or sand bed). The interrogation windows are difficult to be specially designed to avoid the 'boundary effect' since both of the instantaneous water level and the sand bed level vary significantly within a swash period. Therefore, measurement errors occur when conducting PIV analysis of these interrogation windows. In the vicinity of the sand bed, transport velocity is very low because the sand particles are moving within the bottom boundary layer, so the relative

measurement error due to the unmovable san bed is not so large. However, close to the water surface, transport velocity is quite large and the contamination by the immobile blank in an interrogation widow which mostly filled with speedy sand particles can lead to significant measurement errors according to the principle of correlation evaluation. Since the overlap of two adjacent interrogation windows is 75% and the height of the interrogation window is 16 pixels, 2 to 3 (if the center of the interrogation window is just located on the instantaneous bed level or water surface) velocity vectors would be influenced by the boundary effect. The closer with the boundary, the large the measurement error will be.

As indicated in Sect. 3.3, dark patterns leave on the water surface of the recorded images when water depth is decreasing. Since these kinds of dark patterns will make a great contribution to the cross-correlation so measurement error also occurs when they are involved in the interrogation windows. All of these possible measurement errors in the boundary regions need to be carefully handled when quantifying sediment flux.

3.6 Sediment concentration measurement

According to the setup of the instruments, calibration of the Beer-Lambert law was carried out to obtain the relationship between the light intensity and sediment concentration. The detail process is similar with that in Sect. 2.4.1.

For every 0.01s, sediment concentration was measured from the first normal image which is also used for PIV analysis. The mean value of light intensity of each interrogation window in the third iteration was used to calculate the sediment concentration based on the previous calibration result. Therefore, measured sediment concentration has the same temporal and spatial resolution with the transport velocity field.

Apart from the measurement error of transport velocity due to the boundary effect, sediment concentration was affected as well since the same interrogation widows were used. Close to the bed, measurement errors of sediment concentration due to the boundary effect could be ignored because the light intensity of the densely concentrated flow is very close to the unmovable sand bed. However, measured sediment

concentration was underestimated significantly near the water surface since the difference of light intensity between the sand-water mixture and the blank region is great, especially in the early uprush. Moreover, the dark pattern mentioned in Sect. 3.3 would overestimate the sediment concentration near the water surface.

3.7 Sediment flux measurement

Sediment flux was evaluated by the products of sediment concentration and transport velocity at respective locations. It is worthy to note that ‘sediment concentration’ exists under the instantaneous sand bed since interrogation windows were covered the whole inspection lines in the recorded images, while transport velocity measured there was exactly zero giving a zero sediment flux. The resolution of the measurements (sediment concentration, transport velocity, and sediment flux) is 0.27 cm × 0.027 cm in the bed-parallel and bed-normal direction, respectively.

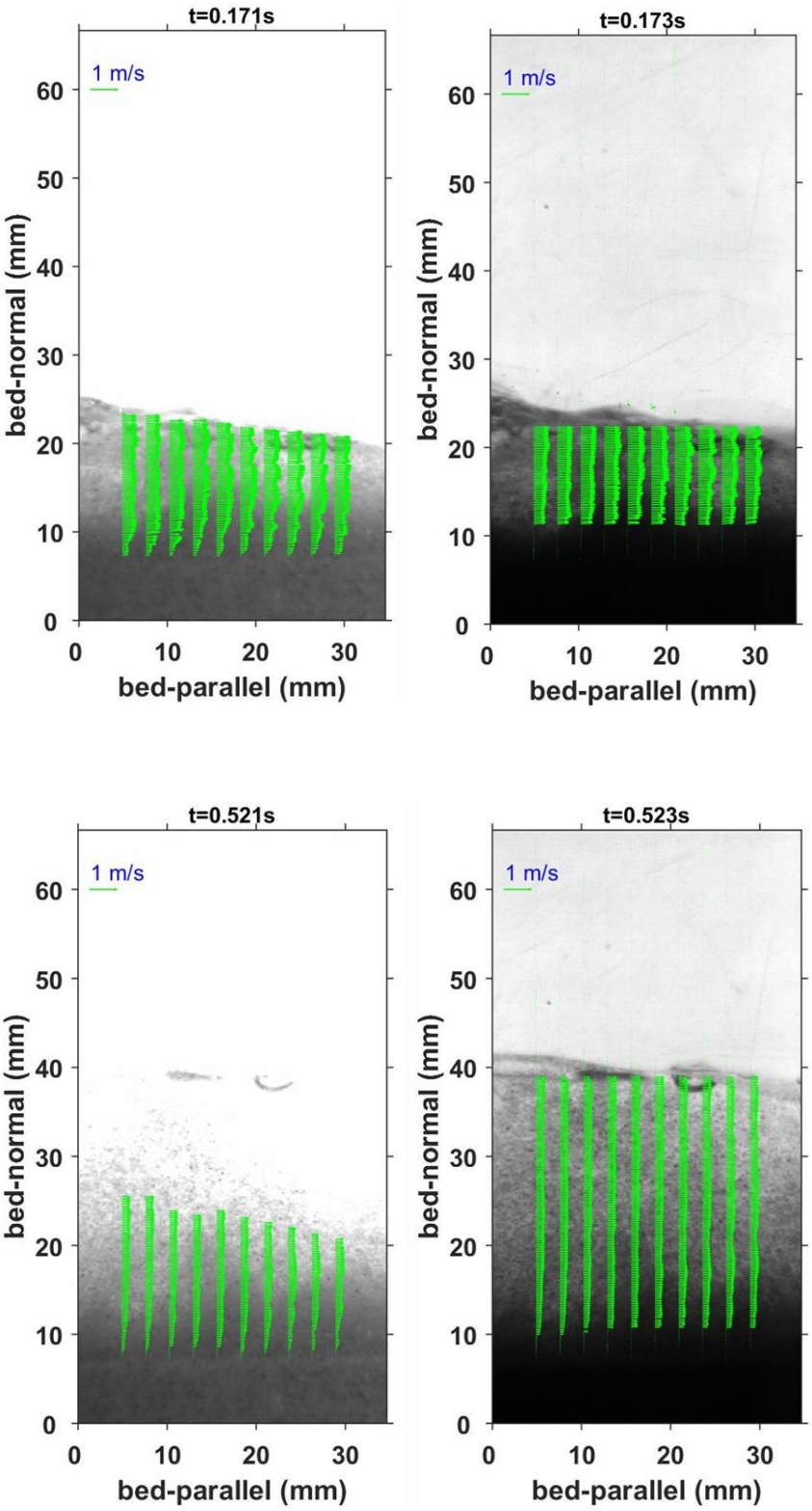

Figure 3-4. Examples of velocity field measured by PIV of several instantaneous swash moments

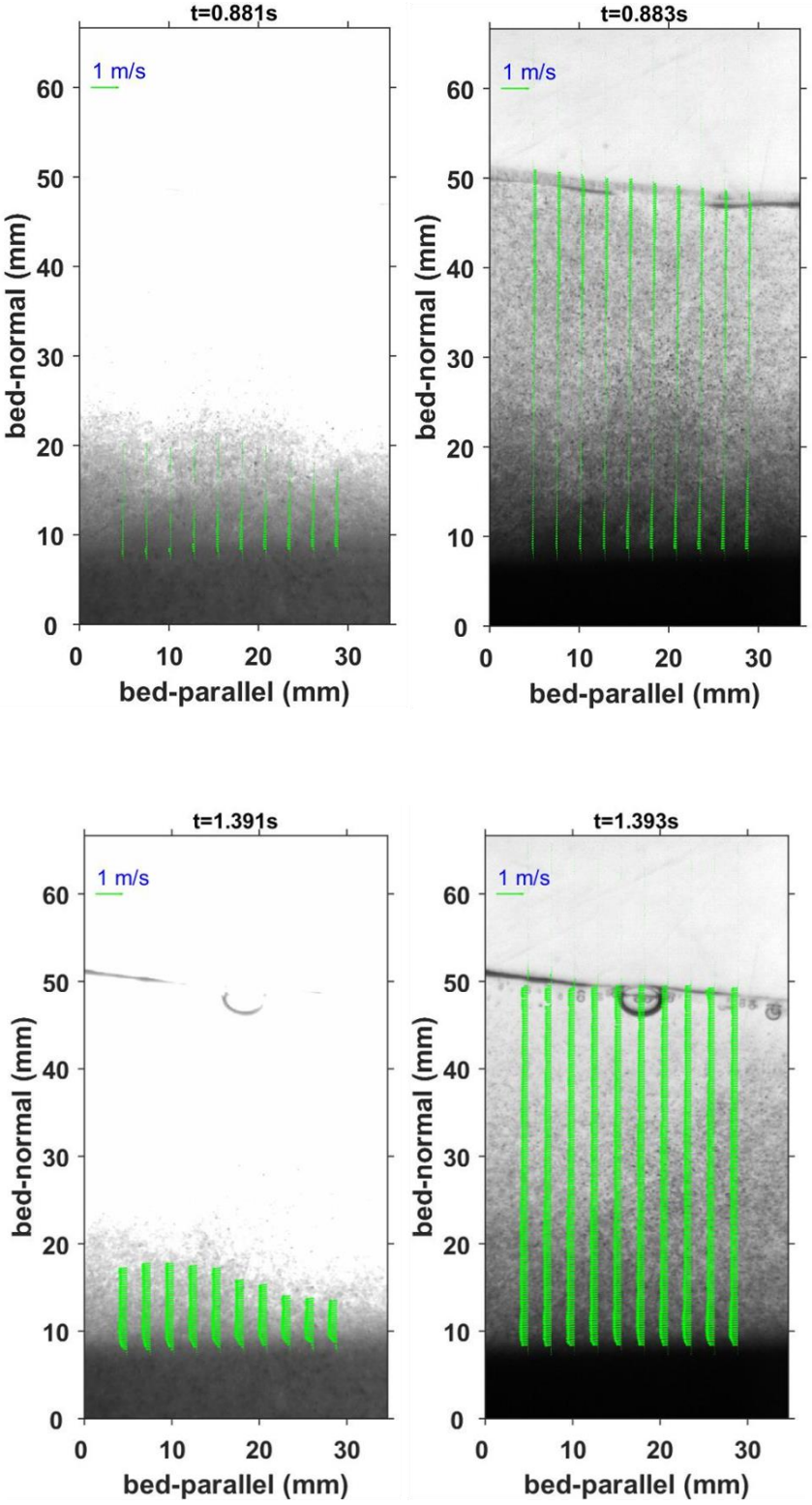

Figure 3-4 (continued). Examples of velocity field measured by PIV of several instantaneous swash moments

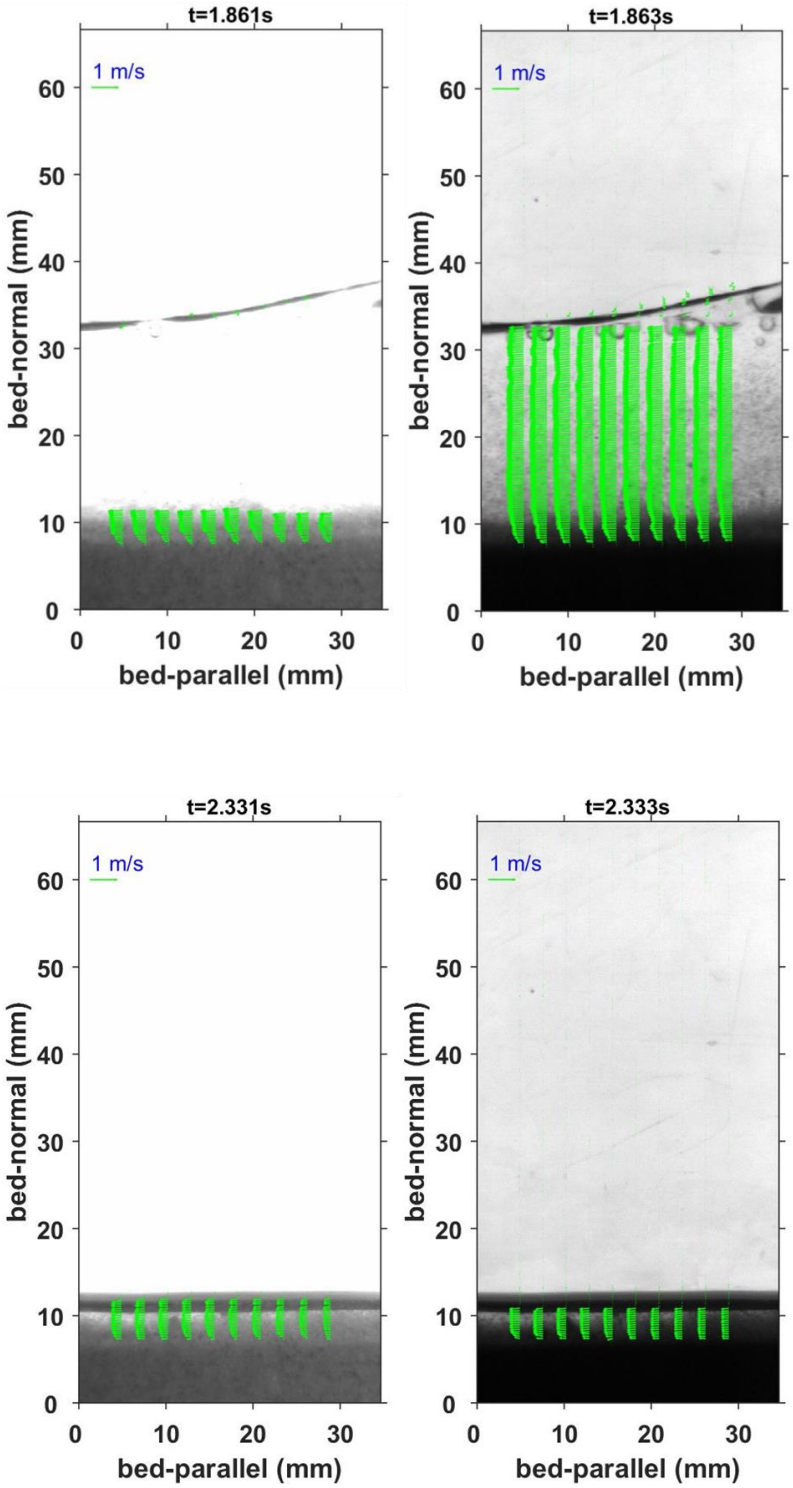

Figure 3-4 (continued). Examples of velocity field measured by PIV of several instantaneous swash moments

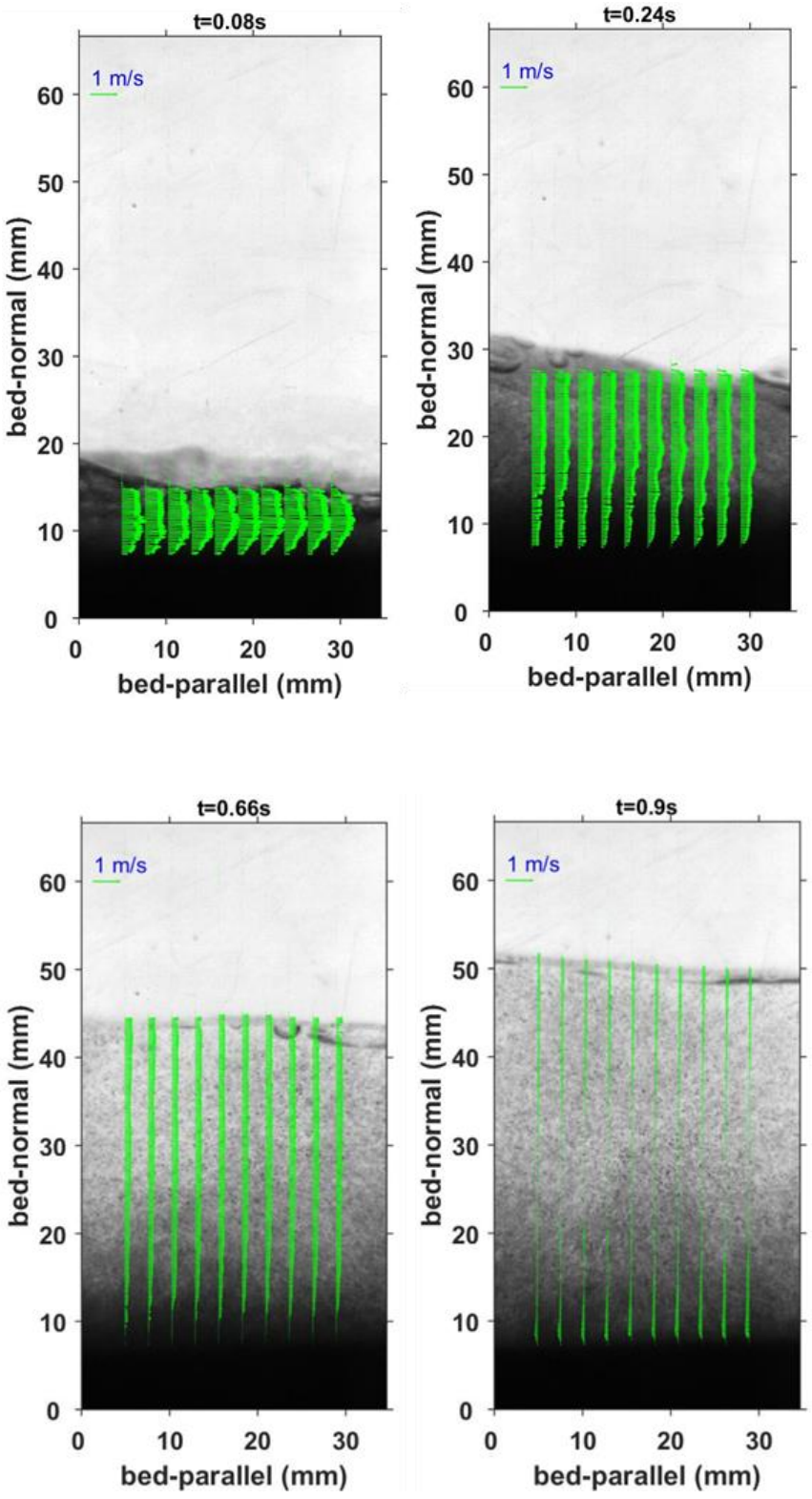

Figure 3-5. Examples of combined velocity field

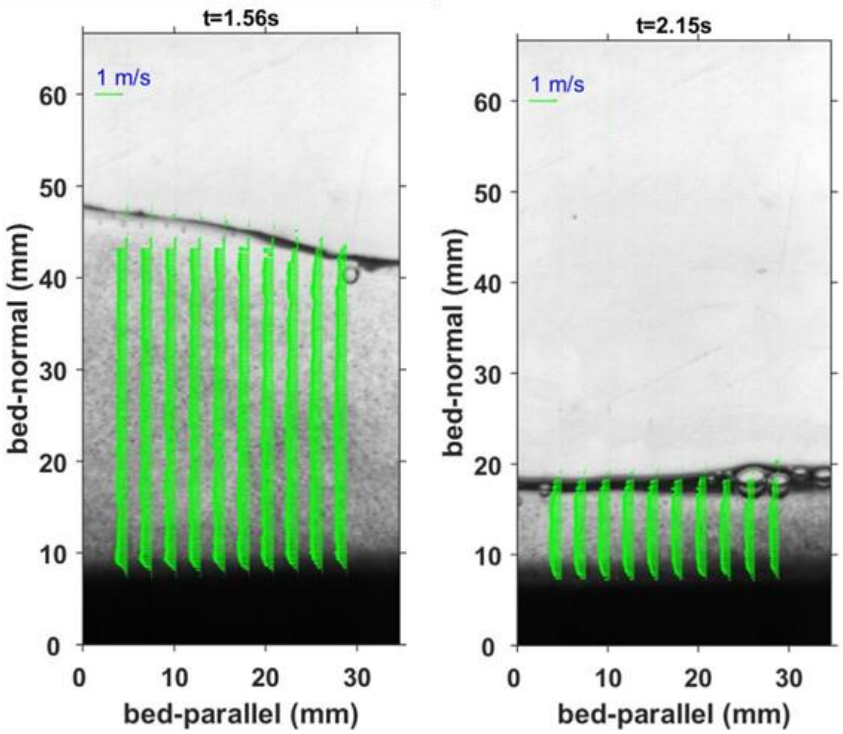

Figure 3-5 (continued). Examples of combined velocity field

Chapter 4 Experimental Results

4.1 Data quality control

In the present study, sediment concentration (c) and transport velocity are measured at 10 inspection lines in the measurement region. z = 0 is the sand bed level before each dam-break flow. In the measurement location, the instantaneous sand bed of one swash circle accretes in the uprush and eroded in the backwash (Fig. 4-3). Net bed level change in the measurement location is positive. Therefore, measurements below the initial sand bed level of each swash circle are not shown in the figures for convenience (hereinafter inclusive). Since the maximum bed level change in the measurement region is around 0.14 cm (Fig. 4-3), 4 to 5 measurement points in maximum would be affected in the vicinity of the sand bed due to the boundary effect mentioned above. Due to the difficulty in decreasing the measurement error in the vicinity of the sand bed, no spatial post-processing methods were employed since errors close to the sand bed are not significant according to the principle of PIV and concentration measurement which have been indicated in the previous section. Some measurement errors could be observed on the water surface due to the dark patterns which have been indicated in Sect. 3.4. They were eliminated manually by comparing the raw recorded images in the further analysis since it is difficult to remove them automatically by using image analysis techniques.

In the following analysis, 4 swash events are selected for detailed analysis based on two criterion. One is that the sand flow is well illuminated by the stroboscope since the stroboscope did not work well for some swash events. Another one is that air bubbles in these 4 swash events are relatively smaller so that the quantification of sediment transport is less affected.

Fig. 4-1 displays the vertical profiles of sediment concentration and bed-parallel velocity at inspection line 1 (left-most in Fig. 3-5), 10 (right-most in Fig. 3-5) and the average value of the 10 inspection lines at several instantaneous phases of swash event 1. It could be found that the difference among them at each swash phase is very small. The phase lag is around 0.05 s which is the duration of the dam-break flow propagating from

the left side to the right side in the measurement region. Sediment concentration and transport velocity are not changed much within this 0.05 s. Vertical profiles of sediment concentration and velocity on the left inspection line could be shifted to the right side almost as they are. Based on this, measurement at the 5th inspection line is chosen for further detailed analysis as a typical representation.

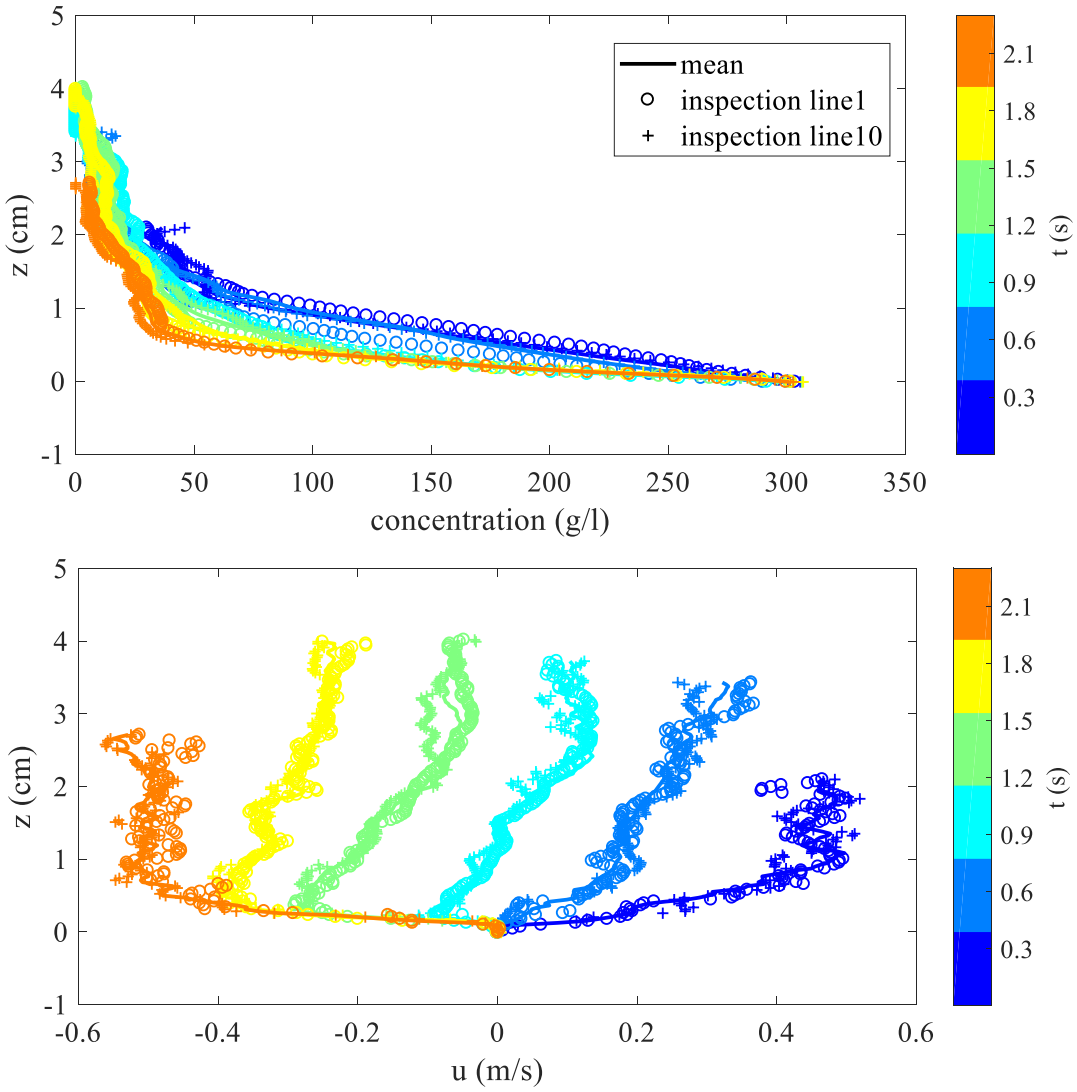

Figure 4-1. Vertical profiles of sediment concentration (upper panel) and bed-parallel velocity (lower panel) at inspection line 1, 10 and the averaged value from the 10 inspection lines of swash event 1

4.2 Bed level evolution

4.2.1 Inter-swash bed level evolution

With the current experimental setup and flow conditions, sands close to the toe of the slope were transported onshore and deposited on the further sand bed. Fig. 4-2 shows the initial sand bed profile and profiles after 5, 10 and 20 swash events of swash event 1. The evolution of the sand bed profile slowed down and did not turn out to be proportional to the number of dam-break flows. In addition, the sand bed did not achieve equilibrium even after 20 swash events.

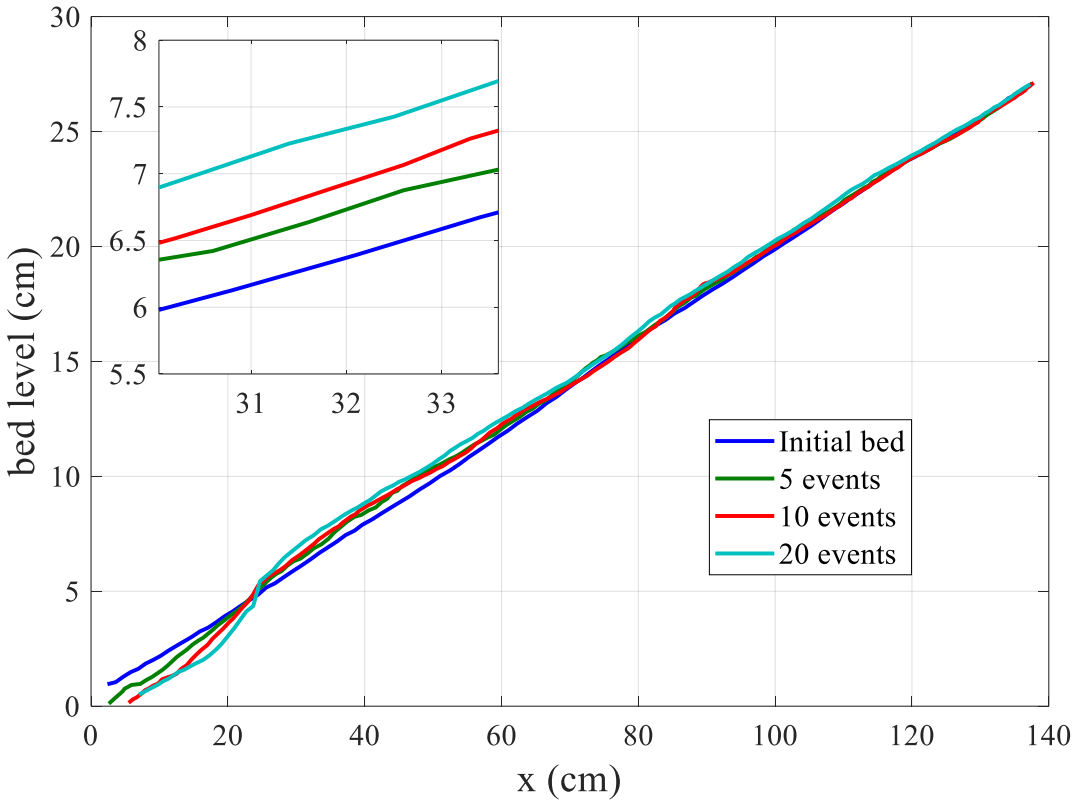

Figure 4-2. Inter-swash bed level evolution of swash event 1

The intersection point of erosion and accretion was located about 25 cm from the toe of the slope, and it kept stable among the 20 swash events. The erosion zone was much narrower than the accretion zone so that the mean erosion depth on the lower bed was

much larger than the mean accretion depth on the upper sand bed. The vertical accretion depth was growing but the change rate was slower than that of erosion. It should be noted that the bed profile very close to the toe of the slope was not measured successfully. Because this part of sand was under the still water level, and the vertical laser distance meter was unable to work in this case.

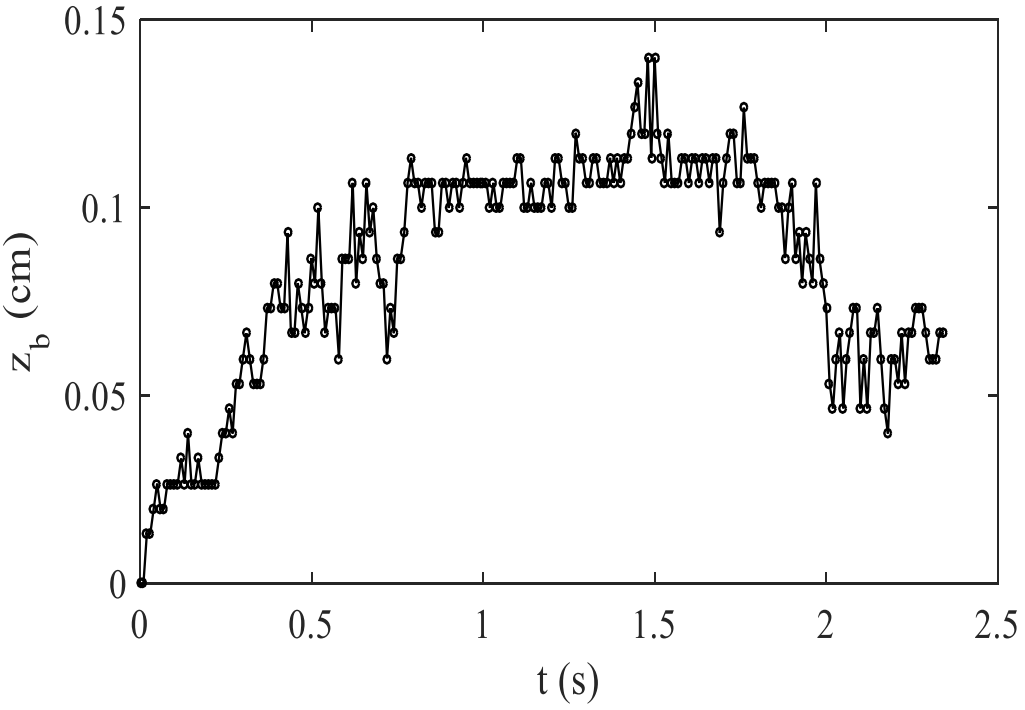

Figure 4-3. Intra-swash bed level evolution of swash event 1

4.2.2 Intra-swash bed level evolution

Since the laser distance meter cannot measure the sand bed level covered by water, the intra-swash bed level was evaluated by image analysis. It was estimated from vertical profiles of image light intensity at a frequency of 100 Hz. Comparing the light brightness profiles between two adjacent combined-illuminated images, they do not change within the immobile part of the sand bed. Therefore, the upper edge of the immobile part was extracted as the instantaneous bed level. Intra-swash variation of bed level is shown in Fig. 4-3. The instantaneous bed level exhibits a gradual increase in the

uprush, keeping stable during flow reversal and decays rapidly in the backwash. Net bed level change due to this swash event was 0.06 cm. The maximum bed level change within this swash circle is 0.14 cm, occurring in the early backwash.

The intra-swash bed level shows a zigzag variation with the swash event. This is because the sand bed does not change much with the short time interval of 0.01s. And a single sand particle (d_{50} = 0.16 mm) sliding on the bed could generate a large variation of the instantaneous bed level since the median diameter of the sand particle is approximately 1/10 of the maximum bed level change of one swash event.

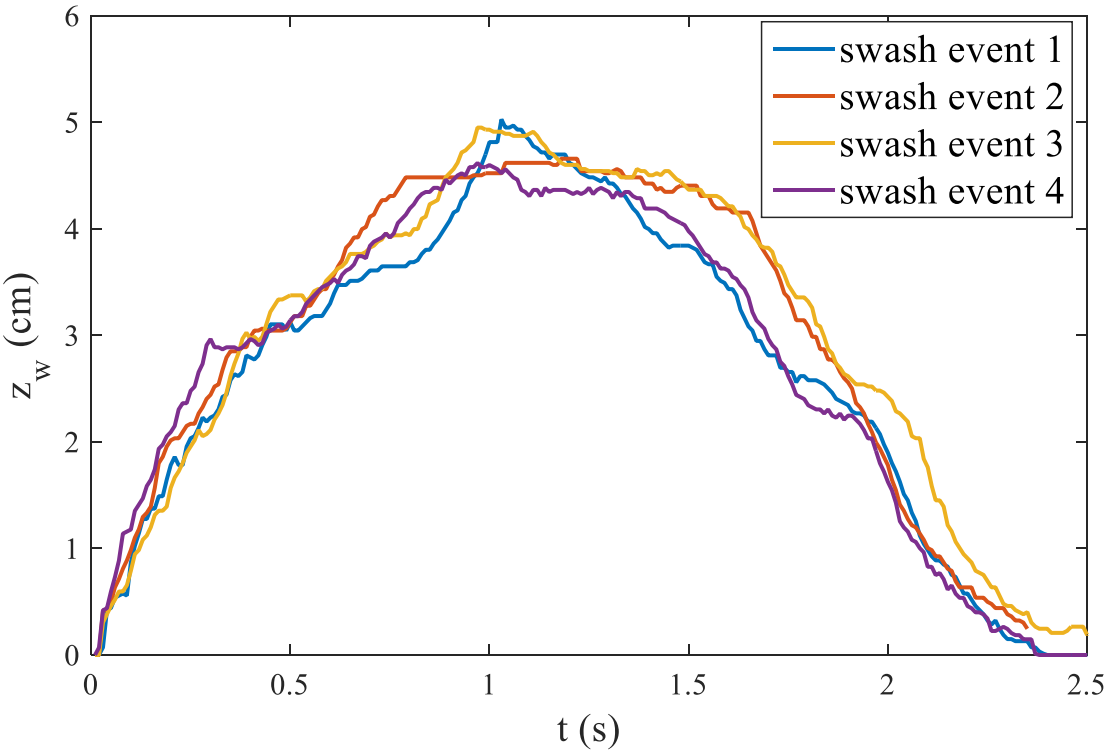

Figure 4-4. Water level evolution of 4 swash events

4.3 Water level variation

The instantaneous water level change of the dam-break generated flow was measured by image analysis through an edge detection technique. Fig. 4-4 shows the instantaneous water level measured at the middle of the recorded images of 4 swash events. Since the

gate of the reservoir was raised by hand and the sand bed was not rebuilt after each dam-break flow, the variation of the instantaneous water level of each swash event was not completely same both in the maximum water depth and the total swash duration (T). However, the general tendency of the water level change is similar with a maximum water depth around 4.7 cm and total duration about 2.4 s. The uprush duration is approximately 2/3 of the backwash duration and the reversal moment of the dam-break flow at the measurement location is 1.0 s (2/5T) after the flow appears in the recorded images.

4.4 Sediment concentration

4.4.1 General distribution of sediment concentration

Fig. 4-5 displays the intra-swash temporal and spatial variation of sediment concentration at inspection line 5 of 4 swash events. General distribution of the sediment concentration is similar among the 4 swash events except for the difference in water surface profiles. It is worth noting that the surface profile of the sediment concentration distribution is slightly lower than the instantaneous water level because measurement errors close to the water surface were removed due to aforementioned boundary effect. Sediment concentration in the uprush is much larger than that in the backwash. A very dense layer of sediment concentration is observed throughout the full swash event in the vicinity of the sand bed. This dense layer can be as high as 0.5 cm in the former half uprush and goes thinner after that. Sediment concentration decreases rapidly with the elevation and concentration during the flow reversal is pretty small.

4.4.2 Time series of instantaneous sediment concentration

Fig. 4-6 shows the instantaneous sediment concentration at inspection line 5 of 4 swash events. The general tendency of sediment concentration at different elevations is similar but the difference in magnitude is large. The difference in the magnitude of sediment concentration varies more significantly in the lower elevations than that in the upper layers and is more severe in the uprush than that of backwash. At the measurement location, sediment concentration reaches a peak soon after the arrival of the dam-break flow. In the very beginning of the uprush, sands on the lower bed are continually picked up and transported onshore-ward. Therefore, the maximum sediment occurs in the

middle of the half uprush rather than the very initial uprush. The occurrence of this peak varies from ¼ to ½ of the uprush duration among different swash events. The maximum sediment concentration is around 250 g/L and 150 g/L at 0.5 cm and 1.0 cm above the initial sand bed, respectively. However, it decreases to 100 g/L and 50 g/L at 1.5 cm and 2.0 m, respectively indicating that the concentration gradient in the lower water column is much more significant. Sediment concentration decays with fluctuation after the peak and there is a sharp decrease when the flow starts to go reversal. This is because the flow turns to be still and there is no force to maintain the sands in suspension when the flow starts to reverse, so the sands deposit quickly resulting in the sharp decrease. On the contrary, there is a small increase in the sediment concentration when the flow starts to go offshore and sands on the further bed moves to the lower region. Sediment concentration then reduces gently until the final backwash with some fluctuations due to the unsteady flow. A sudden increase is observed near the sand bed (z = 0.5 cm) at the final backwash due to re-suspension. Except for the elevations very close to the sand bed where the maximum sediment concentration of backwash appears in the final backwash due to re-suspension, the maximum value of backwash occurs just after the flow reversal when the full water column begins to go to offshore. The difference of the maximum sediment concentration between uprush and backwash is much larger at the lower elevations than that of the higher water column. Sediment concentration varies little close to the water surface (e.g. z = 2.5 cm).

4.4.3 Vertical profiles of instantaneous sediment concentration

Vertical profiles of instantaneous sediment concentration of 4 swash events are shown in Fig. 4-7. Sediment concentration approximately maintains between 250 g/L and 300 g/L in the vicinity of the sand bed throughout the swash event. For each swash phase, sediment concentration decays linearly up to a certain elevation above the initial sand bed. Vertical gradient of the sediment concentration has no general tendency with time elapse. The instantaneous sediment concentration could reduce from 300 g/L to 50 g/L within 2.0 cm for most swash moments. In other words, the dense sediment concentration gathers in a thin layer close to the sand bed. Exceeding this elevation, sediment concentration drops gradually and restlessly due to strong diffusion. Sediment concentration decreases to O (10 g/L) near the water surface finally.

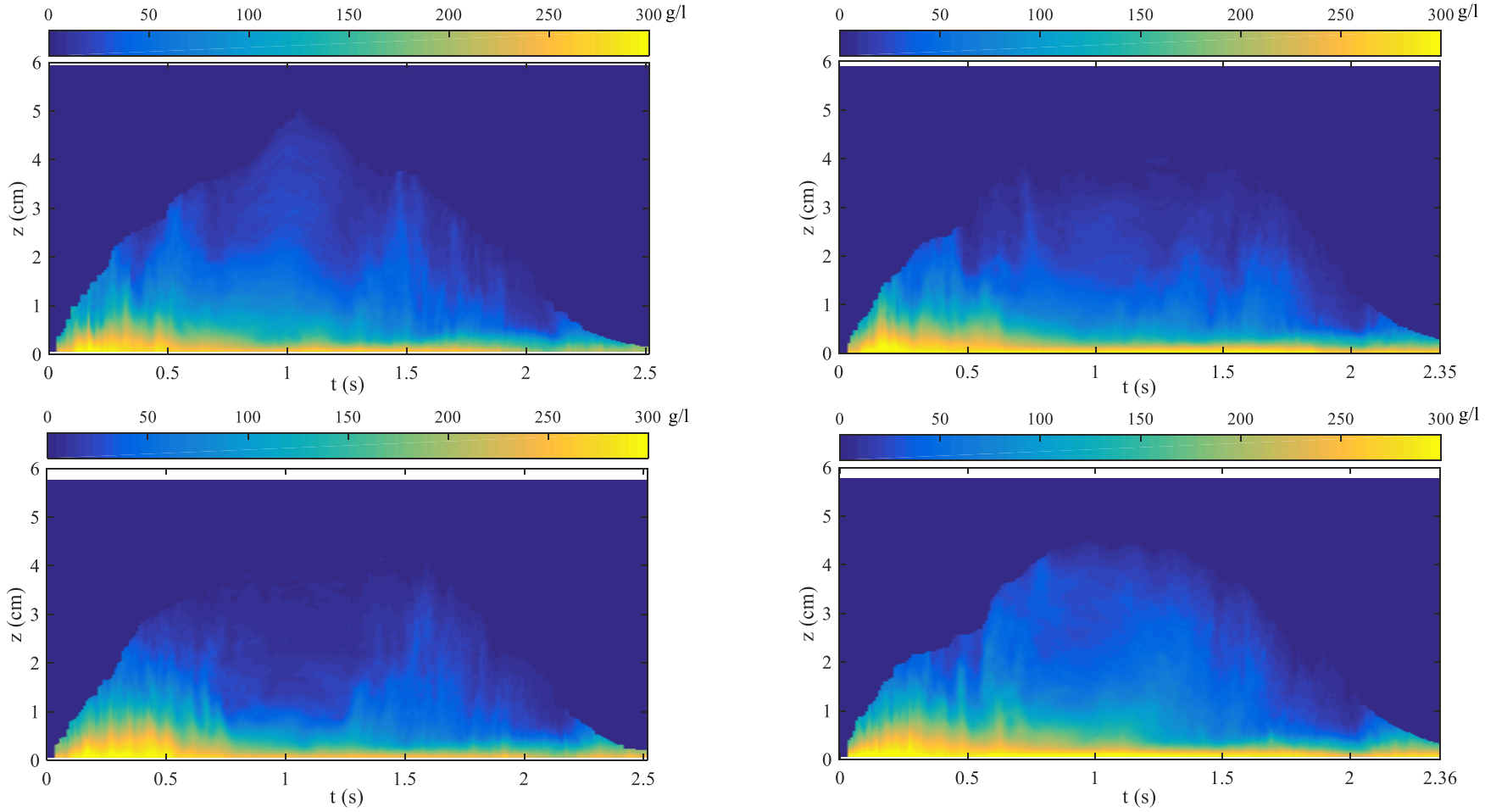

Figure 4-5. Intra-swash sediment concentration distribution of 4 swash events (upper left: swash event 1; upper right: swash event 2; down left: swash event 3; down right: swash event 4, and sic passim)

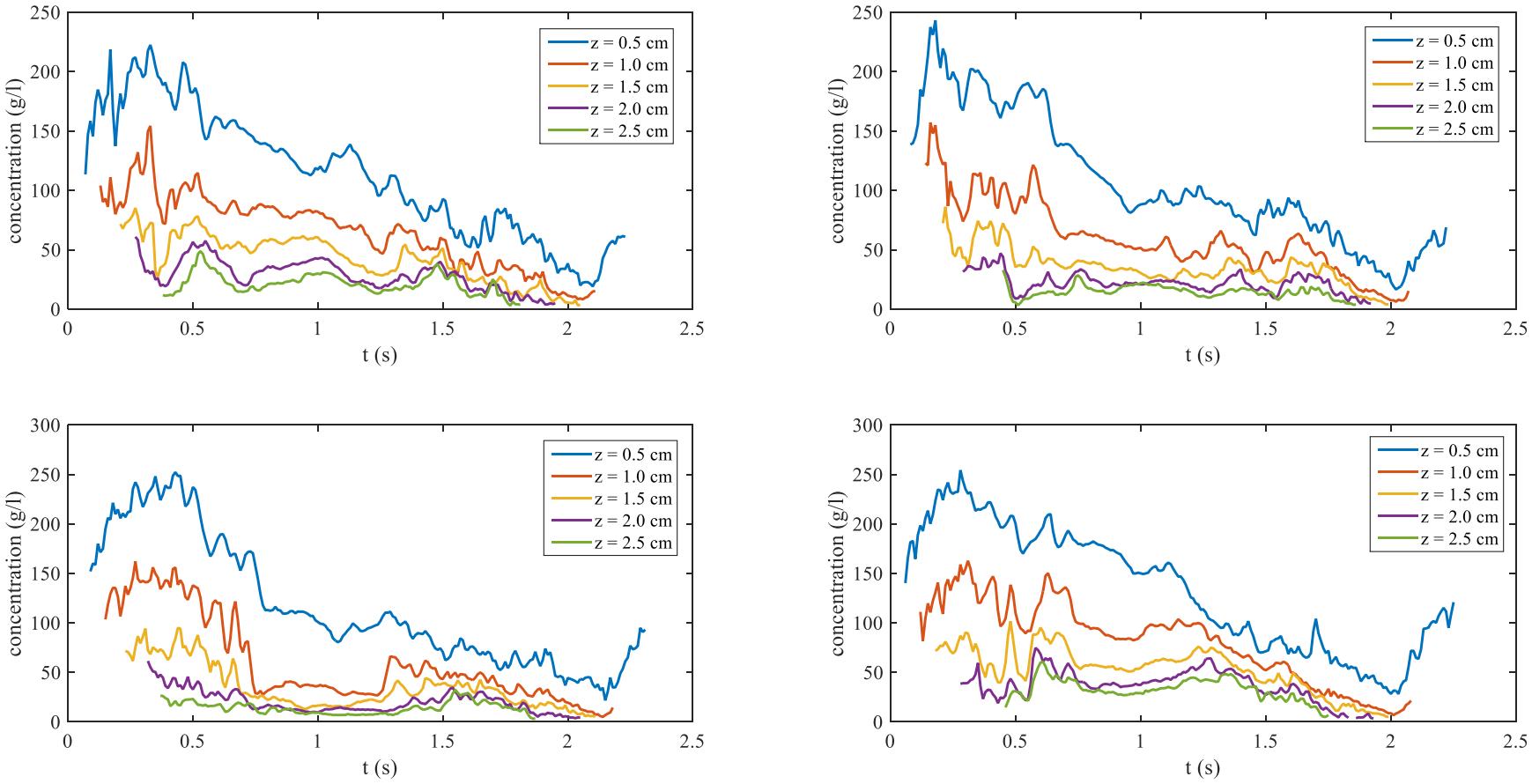

Figure 4-6. Instantaneous sediment concentration of several selective elevations at inspection line 5 of 4 swash events

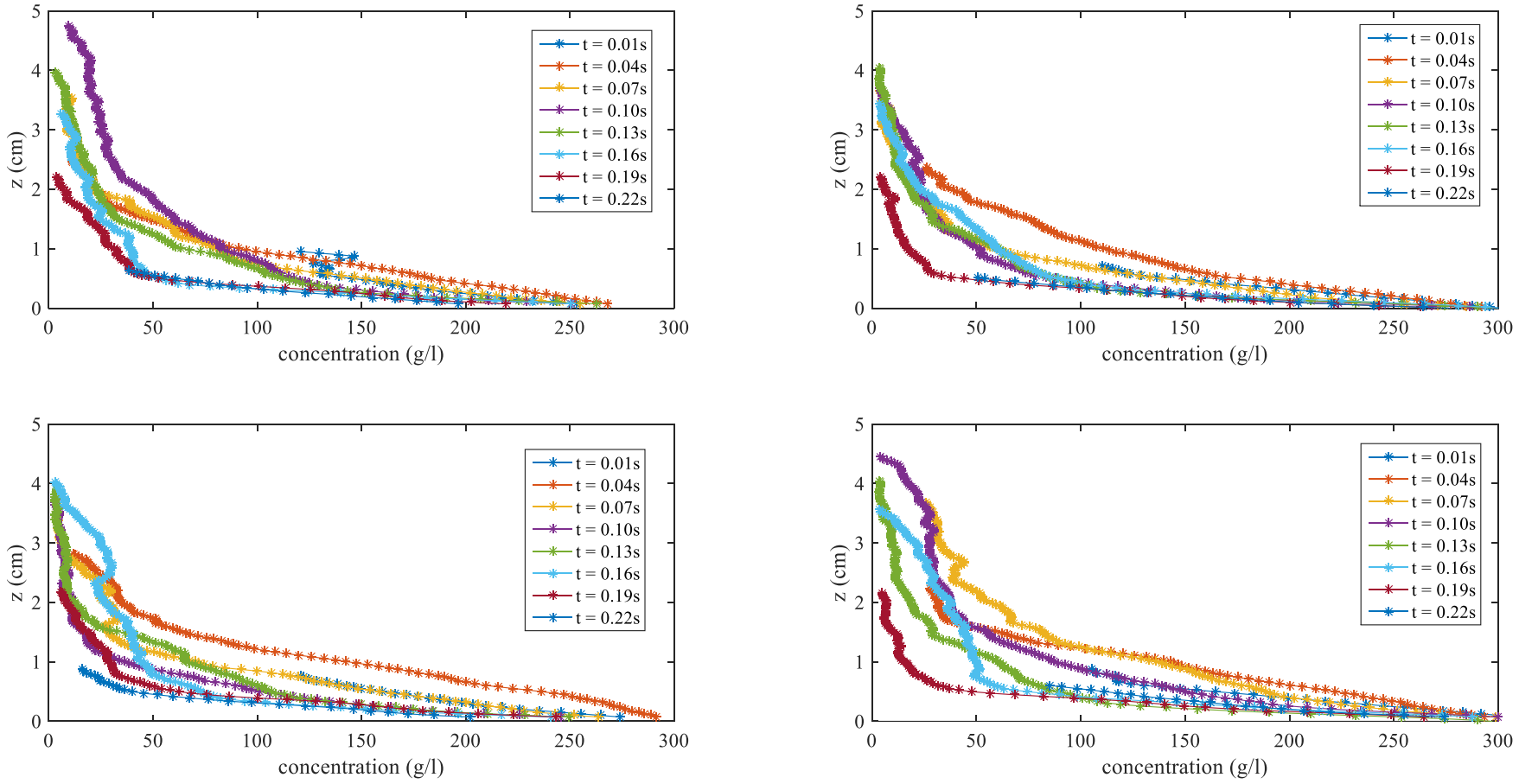

Figure 4-7. Vertical profiles of instantaneous sediment concentration at inspection line 5 of 4 swash events

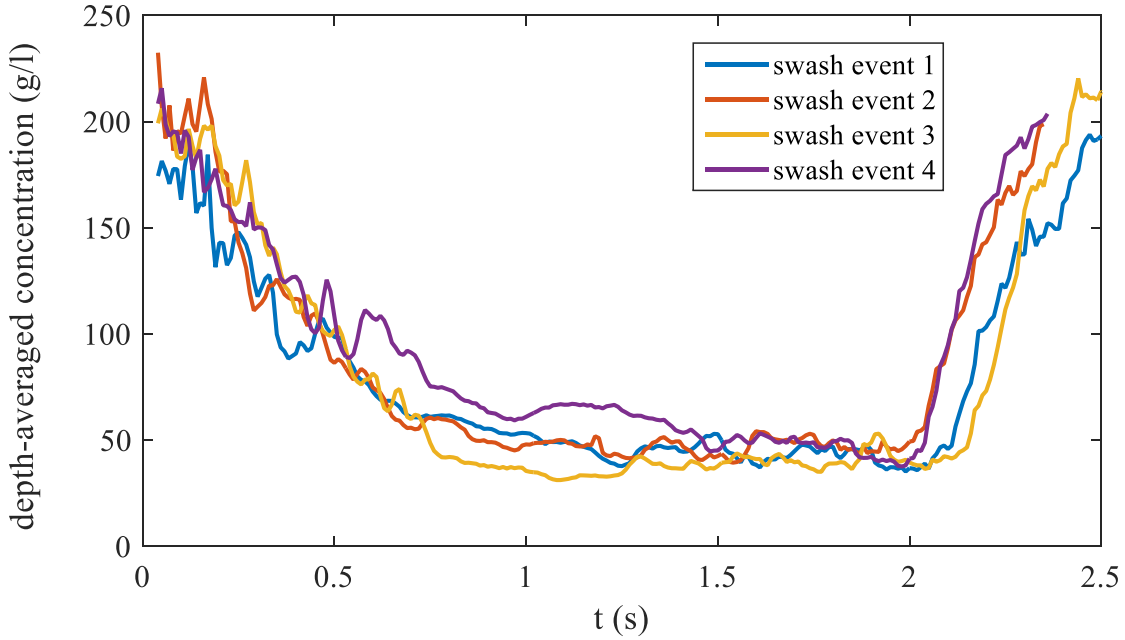

Figure 4-8. Time series of depth-averaged sediment concentration of 4 swash events

4.4.4 Depth-averaged sediment concentration

Fig. 4-8 shows the instantaneous depth-averaged (averaged value between the instantaneous bed level and water level at the measurement location, same below) sediment concentration of 4 swash events. It is found that the maximum depth-averaged sediment concentration is of similar magnitude (200 g/L) both in the initial uprush and later backwash even though that instantaneous sediment concentration has a general decreasing tendency throughout the entire swash duration. The depth-averaged sediment concentration decays gradually during the uprush to a low value about 50 g/L and this value keeps stable during the flow reversal and former half of the backwash, which indicates that sediment pick-up and deposition achieve a balance. In the final backwash, the depth-averaged sediment concentration rises fast due to sediment re-suspension and rapid water depth decreasing. It is found that sediment re-suspension in the final backwash could reshape the sand bed profile significantly by looking into the recorded images.

4.4.5 Rouse's sediment concentration profile

Flowing water has the ability to suspend large quantities of sand particles depending on the availability of sediment and the transport capacity of the flow. To describe the equilibrium conditions in turbulent flows, Rouse (1937) used Schmidt's (1925) diffusion equation and derived the following equations for the vertical distribution of sediment particles,

$$c_z/c_a = \left[\left(\frac{h-z}{z}\right)\left(\frac{a}{h-a}\right)\right]^N \tag{4-1}$$

$$N = \frac{w_0}{\kappa u_*} \tag{4-2}$$

where c_z is the concentration at height z above the sand bed, c_a is the reference concentration at a height $z = a$ of the saltation layer, h is the water depth, N is the Rouse number, w_0 is the settling velocity, κ is the von Karman constant (κ = 0.4), and u_* is the bed shear velocity. The Rouse's sediment concentration profile suggests that the sediment concentration c at a distance z above the bed depends on the total water depth h and the reference concentration c_a at the reference height a based on the ratio of fall versus strength of turbulence acting to suspend particles. This formula has been widely used in engineering application since the sediment concentration profile can be deduced by measurements of several points above the sand bed by using this equation. The Rouse number can be used to determine what grain sizes will travel as suspended or bed load as well. A large Rouse number means the sediment concentration declines more abruptly away from the sand bed, and vise verse.

The value of a on which the vertical profile depends significantly is generally given by $0.05h$ (Vanoni, 1946), half the bed form height (Van Rjin, 1984), or $100d_{50}$ (Shibayama and Rattanapikon, 1993). Since half of the sand bed height and $100d_{50}$ are almost same, here $0.05h$ and $100\,d_{50}$ are used as reference elevations to compare the present measurements to the Rouse's formula for the purpose of validating the Rouse's formula in the swash zone. Fig. 4-9 and 4-10 show the comparison results and Table 4-1 and 4-2

illustrate the fitting parameters by using these two reference elevations, respectively. It is found that the agreement between the measurement and Rouse's formula is good both of the two reference elevations. When $a = 0.05h$, the correlation coefficient of 3 cases is above 0.9 and the other one case is 0.61. For the swash event of low correlation coefficient, the difference between the measurement and the Rouse's formula in the higher elevations is large (over 50%). When using reference elevation of $100d_{50}$, the correlation coefficient of this swash run could be enhanced significantly to 0.81 and the correlation coefficient of the other 3 cases are also improved slightly. The Rouse number varies between 0.43 and 0.68 and transport mode in the present experiment belongs to full suspended load according to empirical law. And it is a little larger when using reference elevation of $100d_{50}$ than that of $0.05h$.

Moreover, when $a = 0.05h$, the Rouse's formula performs better in the lower elevations than the higher water column. On the contrary, the Rouse's formula produces a better result in the higher water column than the lower elevations when using reference elevation of $100d_{50}$. This result is easy to interpret because when a larger reference elevation used, the higher water column would be fitted better according to the property of the exponential function. Even though the Rouse's formula shows a sufficiently acceptable capability of describing sediment concentration profile in the swash zone, it is suggested that better result is expected if using a more suitable reference elevation. However, to achieve this target, a series laboratory measurement is necessary to deduce the function of choosing the optional reference elevation. It is important since most of the measurement instruments cannot cover the whole water column in the swash zone, and interpolation is often conducted for filling in the data gaps (e.g. Puleo et al., 2016). Precise interpolation functions like the Rouse's formula thus play important roles in the quantification of sediment transport.

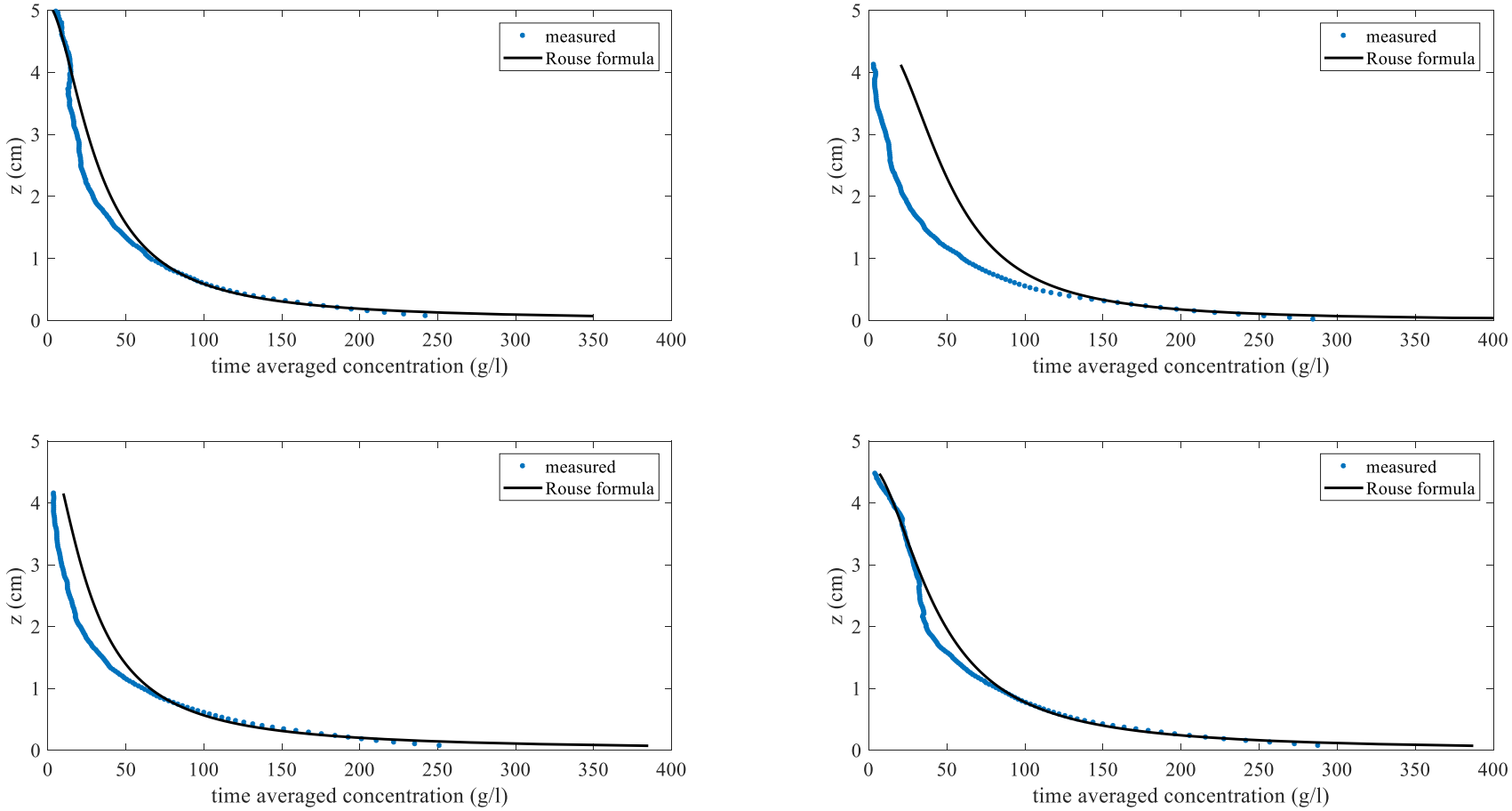

Figure 4-9. Comparison between the Rouse formula and measured time-averaged sediment concentration with the reference elevation equals to 0.05h

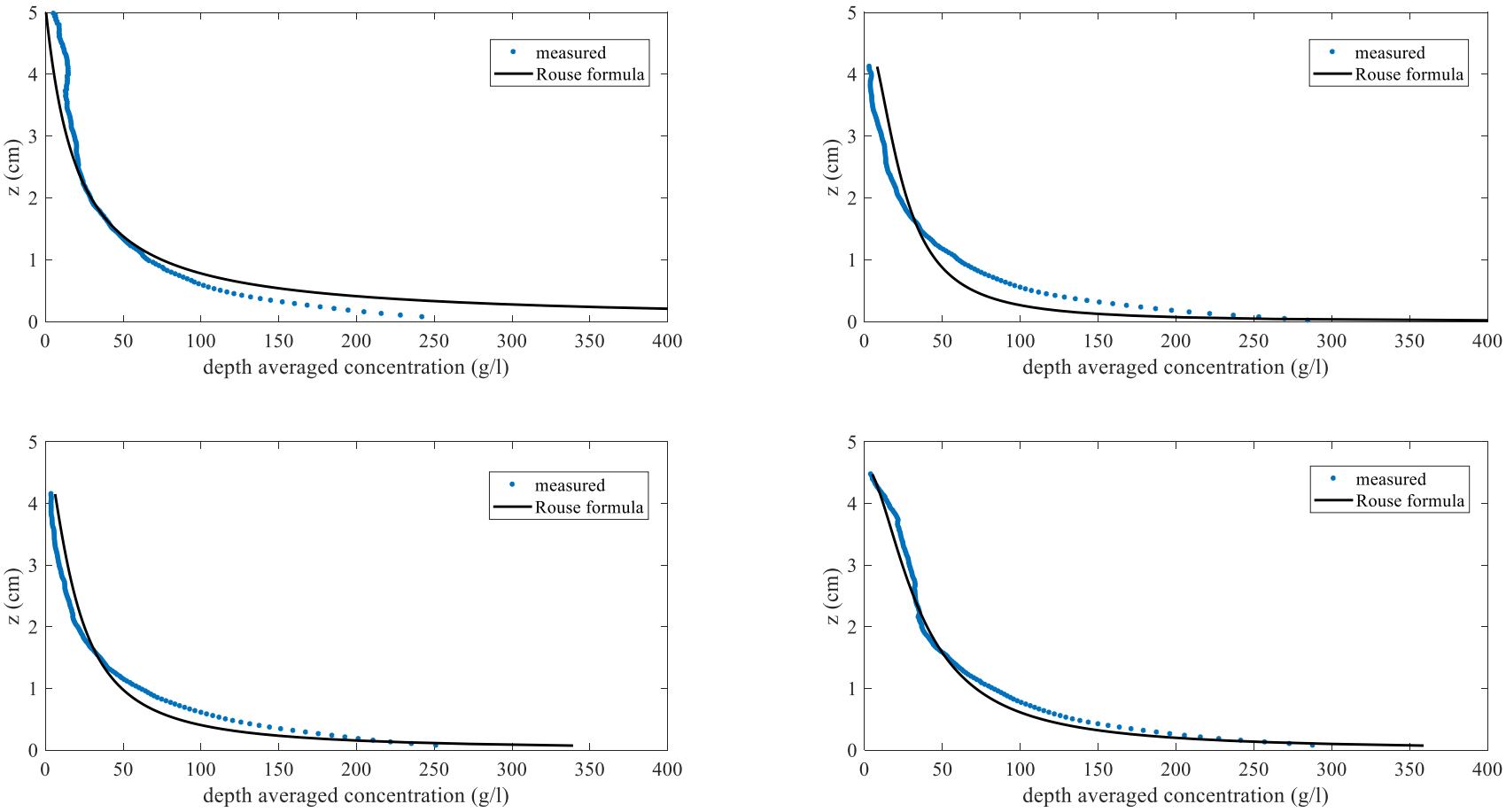

Figure 4-10. Comparison between the Rouse formula and measured time-averaged sediment concentration with the reference elevation equals to $100d_{50}$

Table 4-1.Regression statistics of Rouse formula by using the reference elevation equals to $0.05h$

Case	h (cm)	a (cm)	Reference concentration (g/L)	Rouse number (N)	r^2
1	5.01	0.25	168	0.57	0.94
2	4.66	0.23	177	0.43	0.61
3	4.95	0.25	175	0.62	0.90
4	4.52	0.23	205	0.53	0.96

Table 4-2. Regression statistics of Rouse formula by using the reference elevation equals to $100d_{50}$

Case	h (cm)	a (cm)	Reference concentration (g/L)	Rouse number (N)	r^2
1	5.01	1.60	40	0.58	0.96
2	4.66	1.60	32	0.52	0.81
3	4.95	1.60	32	0.68	0.92
4	4.52	1.60	49	0.56	0.96

4.5 Transport velocity

4.5.1 General distribution of transport velocity

Since the high-speed camera was aligned with the slope, the measured velocities of the 2-D plane were bed-parallel (u) and bed-normal (w) instead of horizontal and vertical. Fig. 4-11 and 4-12 display the intra-swash temporal and spatial variation of bed-parallel and bed-normal transport velocities respectively at inspection line 5 of 4 swash events. For each elevation, the maximum bed-parallel velocity occurs when the dam-break flow firstly reaches the measurement location, and then the transport velocity decays rapidly until the flow reversal. Sand particles close the bed reverse earlier than those in the upper layers. During the backwash, the magnitude of bed-parallel velocity has an increase-to-decrease tendency with the maximum offshore velocity appears in the middle of the backwash. The vertical gradient of bed-parallel velocity is obvious and a thin layer of zero velocity is observed in the vicinity of the sand bed, which shows the variation of the bed level. The magnitude of uprush bed-parallel velocity is generally a little larger than that of backwash because of energy dissipation.

Compared to the bed-parallel transport velocity, the bed-normal velocity is much smaller by almost one order of magnitude. The distribution of bed-normal velocity has no evident trend. The vertical mixing in the initial uprush is significant due to turbulence (both bore generated and bed generated) and then the dam-break flow calms down. Sand particles settle down quickly when the flow starts to reverse. Strong upward bed-normal velocity is found in the late backwash and the resulting fluid force is considered to be the cause of sediment re-suspension. It is worth noting that with the present setup of the instruments, most of the vertical displacements of the interrogation windows within 0.001s are smaller than one pixel (Fig. 4-13), which means that the accuracy of the bed-normal velocity is not high according to the principle of PIV. Therefore, no further analysis of the bed-normal transport velocity is conducted.

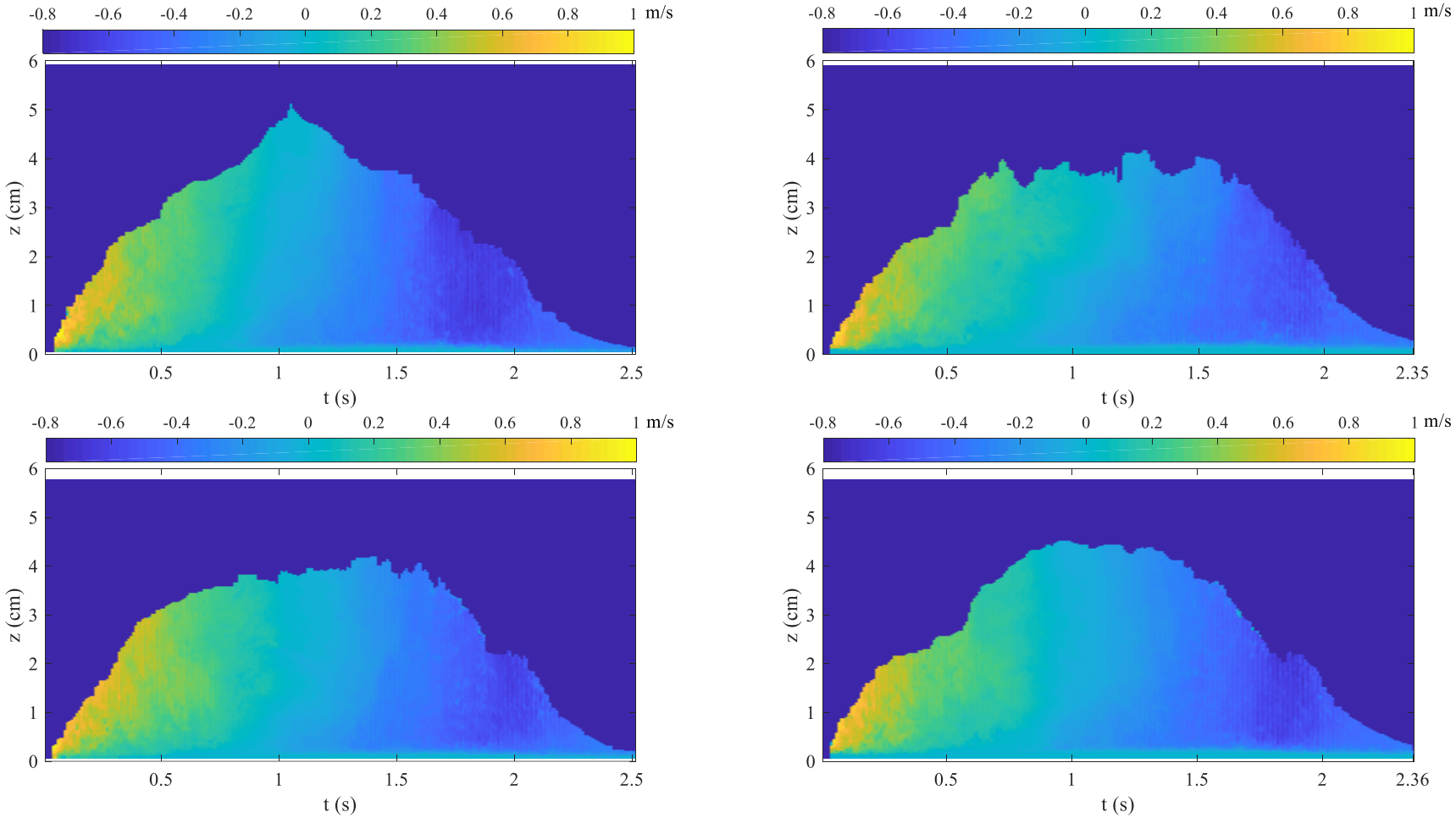

Figure 4-11. Temporal and spatial variation of bed-parallel velocity of 4 swash events

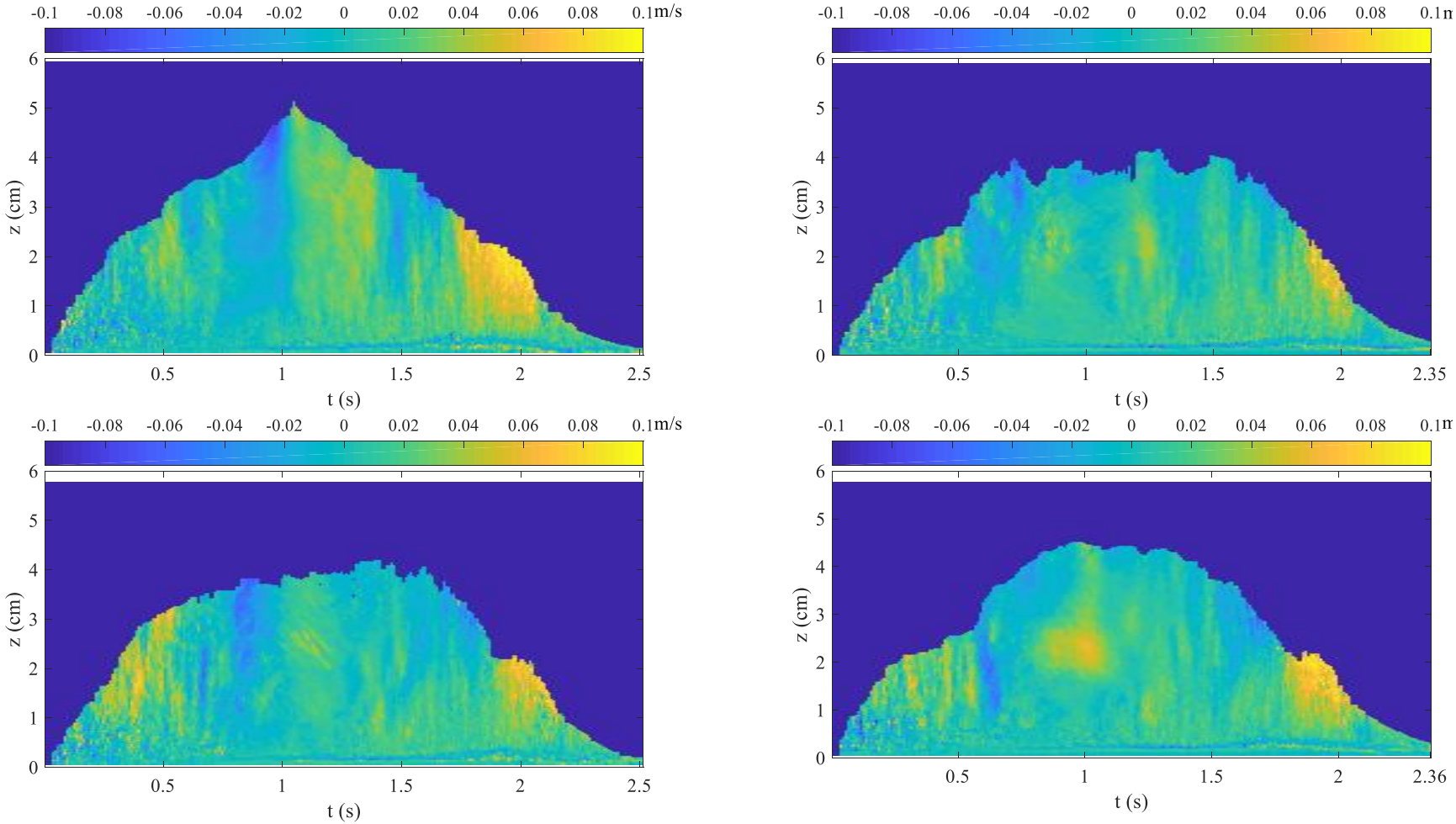

Figure 4-12. Temporal and spatial variation of bed-normal velocity of 4 swash events

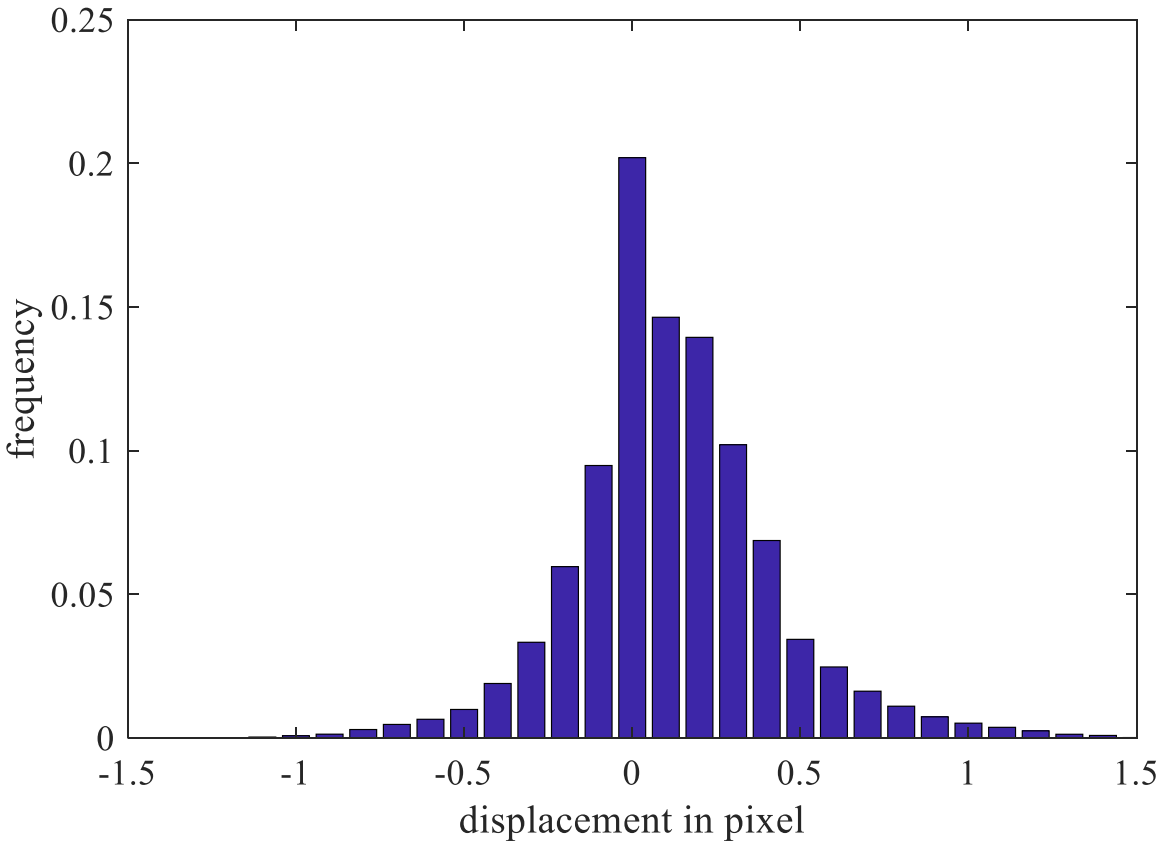

Figure 4-13. Histogram of the bed-normal displacement of the interrogation windows

4.5.2 Time series of instantaneous bed-parallel velocity

Fig. 4-14 shows the time series of instantaneous bed-parallel transport velocity of several selective elevations above the initial sand bed at inspection line 5 of 4 swash events. As indicated above, the measured velocity represents the velocity of sand particles instead of the water flow itself. Even so, sand particles follow the flow well under the bore-driven (dam-break) swash conditions. The overall characteristics of the time series of the transport velocity agree well with those measurements focused on the flow in the past studies carried out in the laboratory (Kikkert et al., 2012, 2013) and the field (Masselink and Hughes, 1998; Puleo et al., 2000, 2012). The variation of the transport velocity is quite fluctuating especially in the initial uprush and late backwash where the flow is significantly turbulent, resulting in a pretty chaotic movement of the

sand particles. It is found that the uprush duration is approximately 2/3 of the backwash duration. Sand particles near the bed reverse earlier than those in the upper layers. Reversal time is around 0.7 s at z = 0.5 cm and 1.1 s at z = 2.5 cm. The difference in the reversal time could be 1/6 of the total swash duration within this thin water depth. The maximum uprush bed-parallel velocity is around 0.8 m/s, occurring when the dam-break flow first reaches the measurement location and then it decays with a relatively stable rate until the flow reversal. Compared to the velocity history in Fig. 4-6, phase lag between the maximum bed-parallel velocity and maximum sediment concentration is very large. The maximum backwash bed-parallel velocity appears in the late backwash instead of the end of the swash event as has been reported by some past researches (e.g. Inch et al., 2015; Ruju et al., 2016b) and its magnitude (around 0.6 m/s) is smaller than that in the uprush. The occurrence time of the maximum bed-parallel velocity depends on the measurement region significantly. The present measurement is carried out on the foreshore of the swash zone and the occurrence time of the maximum bed-parallel velocity in the offshore side may differ. On the other hand, the difference might due to that the traditional instruments for velocity measurement are unable to work very close to the sand bed so that the velocity information is truncated. The magnitude difference of the bed-parallel velocity is larger in the uprush than that of backwash, which means that the bed-parallel velocity profile is more uniform in the backwash.

4.5.3 Depth-averaged bed parallel velocity

Time series of the depth-averaged bed-parallel velocity of 4 swash events is shown in Fig. 4-15. The general tendency of the depth-averaged bed parallel velocity of each swash event is exactly same while difference exists among the magnitude of each swash event. At the measurement location, the maximum depth-averaged uprush velocity occurs in the initial uprush and the maximum depth-averaged backwash velocity appears around 1.7 s. The maximum depth-averaged bed-parallel velocity of uprush and backwash is around 0.7 m/s and 0.5 m/s, respectively.

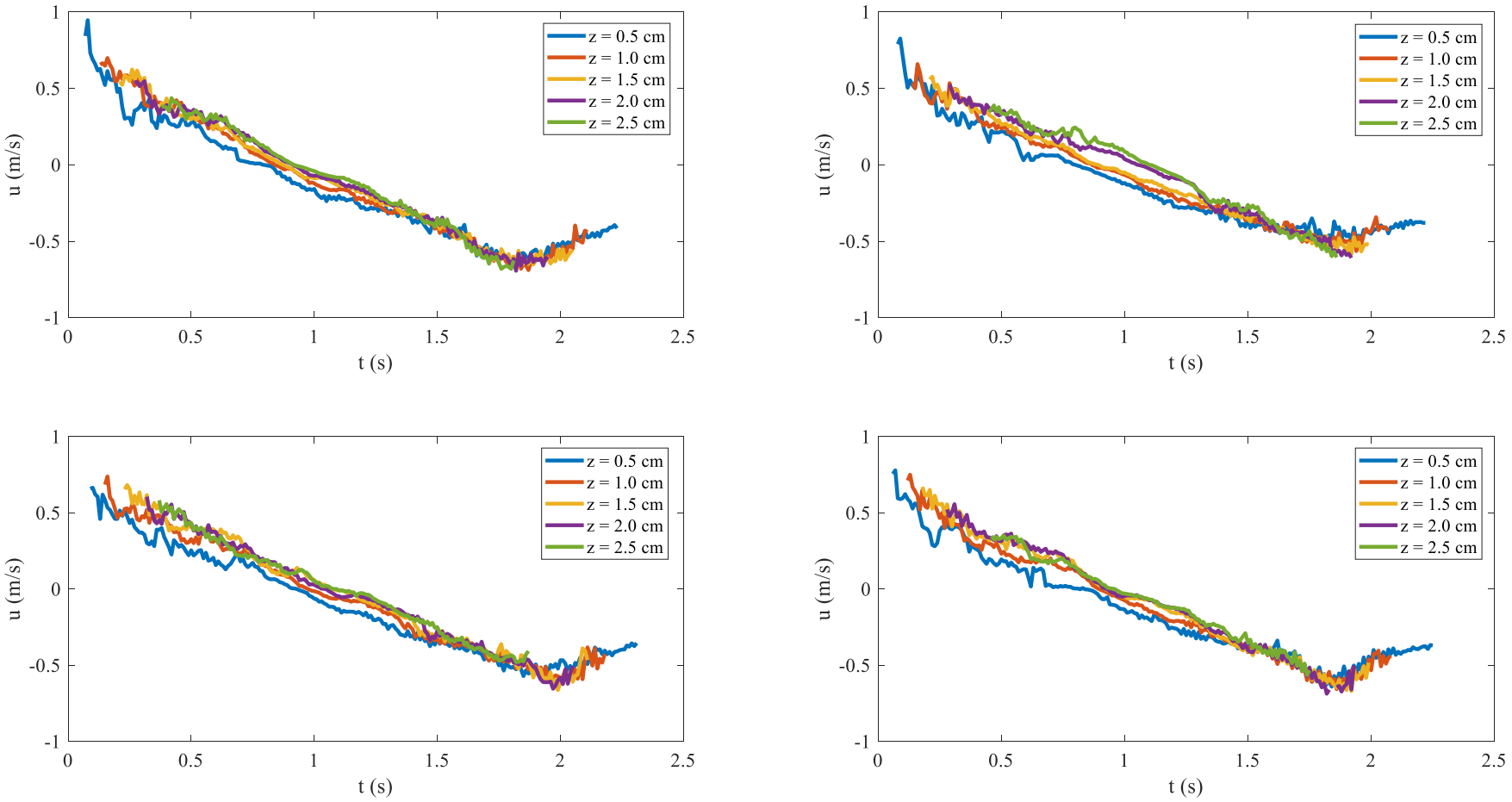

Figure 4-14. Instantaneous bed-parallel velocity at several selective elevations at inspection line 5 of 4 swash events

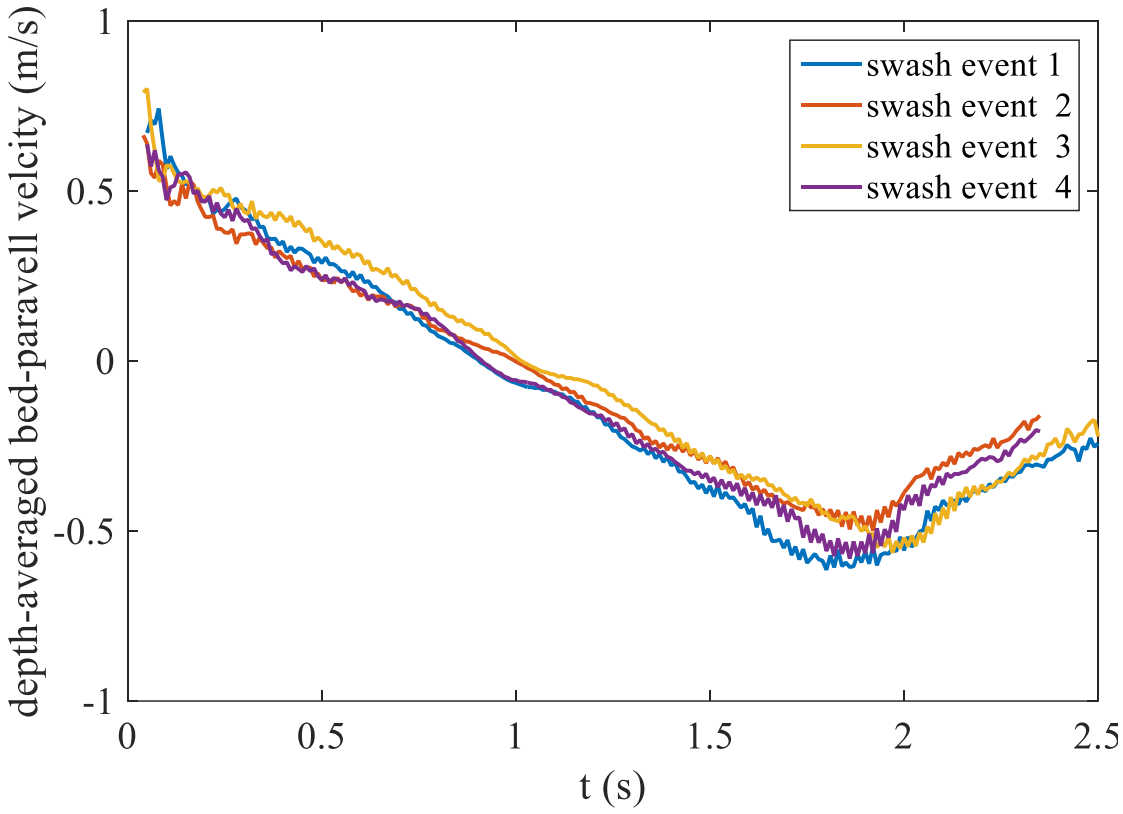

Figure 4-15. Time series of depth-averaged bed-parallel velocity of 4 swash events

4.5.4 Vertical profiles of the bed-parallel velocity

Fig. 4-16 shows the instantaneous vertical profiles of bed-parallel velocity at inspection line 5 of 4 swash events. Generally, velocity profiles exhibit a forward leaning and backward leaning shape in the uprush and backwash, respectively. The magnitude in the vertical gradient of the bed-parallel velocity profiles decays during the uprush and increases during the former half backwash. In the late backwash, the gradient keeps unchanged. Vertical gradient of the bed-parallel velocity is very large throughout the whole water column in the entire uprush period thus the velocity profiles are completely non-depth uniform. In the backwash, the velocity gradient is only significant in the lower water column and the velocity tends to be uniform in the upper layers. The magnitude of the bed-parallel velocity does not show a progressive increasing trend from the sand bed to the water surface in every moment. Oppositely, velocity profiles are quite irregular indicating the turbulence are significantly.

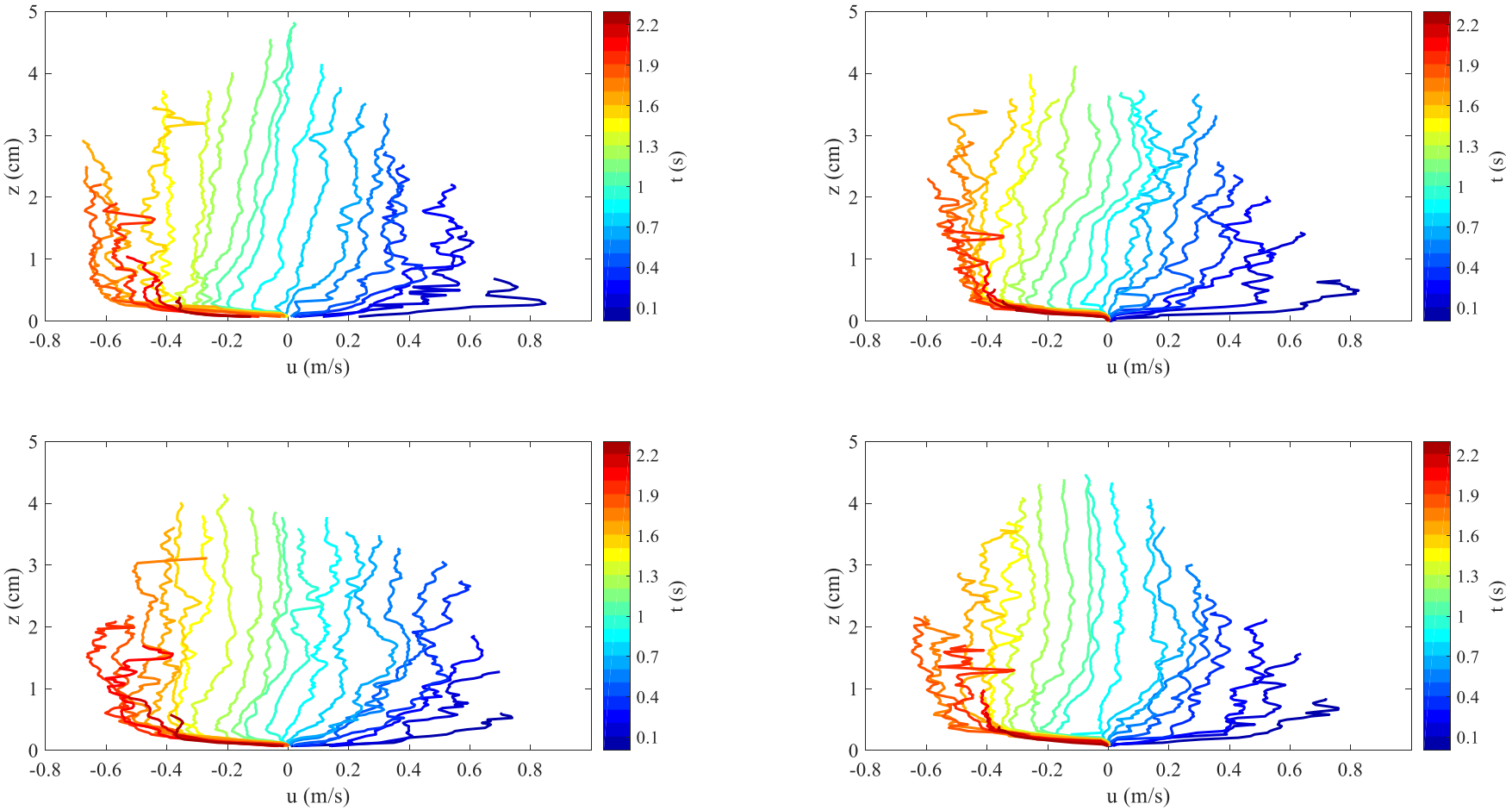

Figure 4-16. Instantaneous vertical profiles of bed-parallel velocity at inspection line 5 of 4 swash events

4.6 Boundary layer thickness

The vertical gradient of the bed-parallel velocity is used to estimate the boundary layer thickness (e.g. location of the top of the boundary layer). It is assumed that the free stream extends above the top of the boundary layer where the local bed-parallel velocity gradients are smaller than a small fraction of a reference velocity gradient,

$$\frac{\partial u}{\partial z} < k\frac{\Delta u}{\Delta z} \tag{4-3}$$

where Δu and Δz are the maximum bed-parallel velocity and maximum water depth during one swash event, respectively. k is constant that was set equal to 0.2 following Ruju et al. (2016b). Ruju et al. (2016b) failed in the identification of the boundary layer thickness during the uprush because significant temporal and spatial variability of the velocity gradient was found which might be due to the bore generated turbulence. In this study, variability in the velocity gradient is also observed since instantaneous data were used (without ensemble averaging). However, thanks to the high-resolution measurement, the proportionality of misguided estimation in the instantaneous boundary layer thickness is less and the obviously mistaken values were replaced by interpolation. Fig. 4-17 shows the time series of instantaneous of boundary layer thickness and water depth of 4 swash events. It is found that the instantaneous boundary layer can extend to the local water depth in the initial uprush and stays for about 1/10T. It decays gradually and turns to be almost zero during flow reversal. The instantaneous boundary layer thickness grows progressively after the flow reversal and is constricted by the water depth again in the late backwash (keeps approximately 1/5T). The maximum boundary layer thickness of both uprush and backwash are of similar magnitude, being 2/5 of the maximum water depth. It is suggested that the boundary layer develops rapidly and can extend to a large part of the water column in the very foreshore region even though the flow duration is very short.

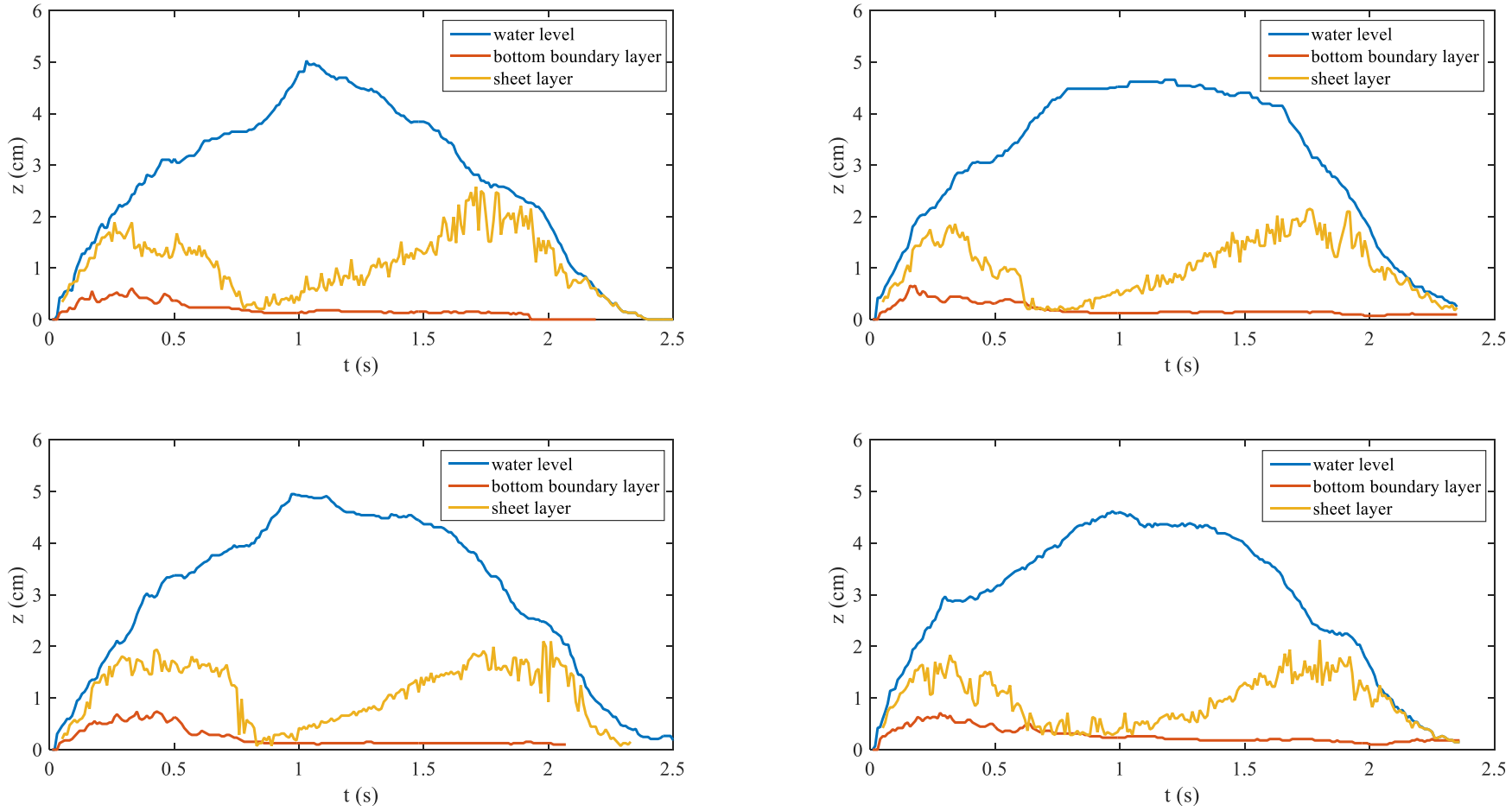

Figure 4-17. Time series of water level, boundary layer thicknessnd sheet layer thickness

4.7 Sediment flux

4.7.1 General distribution of sediment flux

Instantaneous bed-parallel sediment flux (q) was calculated by the product of sediment concentration and bed-parallel transport velocity at respective locations,

$$q = cu \tag{4-4}$$

Hereafter, sediment flux refers to the bed-parallel component without explicitly stating the phrase 'bed-normal sediment flux'. Fig. 4-18 shows the intra-swash temporal and spatial variation of sediment flux of 4 swash runs. The maximum flux occurs in the initial uprush where both sediment concentration and velocity are significant, indicating that a large amount of sand is transported onshore ward when the flow runs up the beach. The bed-parallel sediment flux decays rapidly after this significant onshore transport regime and turns to be almost zero during flow reversal where the transport velocity decreases to zero. In the backwash, sediment flux in the vicinity of the sand bed is large due to large concentration related to deposition. On the contrary, sediment flux is relatively weak in the upper water column due to weak sediment concentration. Vertical gradient of sediment flux during backwash is weaker than that of uprush. The maximum magnitude of sediment flux in the uprush (150 kg/m^2/s) is twice as larger as that of backwash (-80 kg/m^2/s).

Fig. 4-19 shows the temporal and spatial variation of bed-normal sediment flux evaluated by *cw* of 4 swash events. The bed-normal sediment flux is significantly chaotic in the uprush due to high level turbulence and this turbulent phase continues for more than half of the uprush duration. In the backwash, the bed-normal sediment flux is more stable since the bed-generated turbulence is unable to disturb the upper flow regime except for the final backwash. The magnitude of bed-normal sediment flux is smaller than that of bed-parallel sediment flux by one order due to the difference in velocity. Since the accuracy of bed-normal velocity is not so convincible (indicated in Sect. 4.1) that no further analysis is carried out in terms of the bed-normal sediment flux.

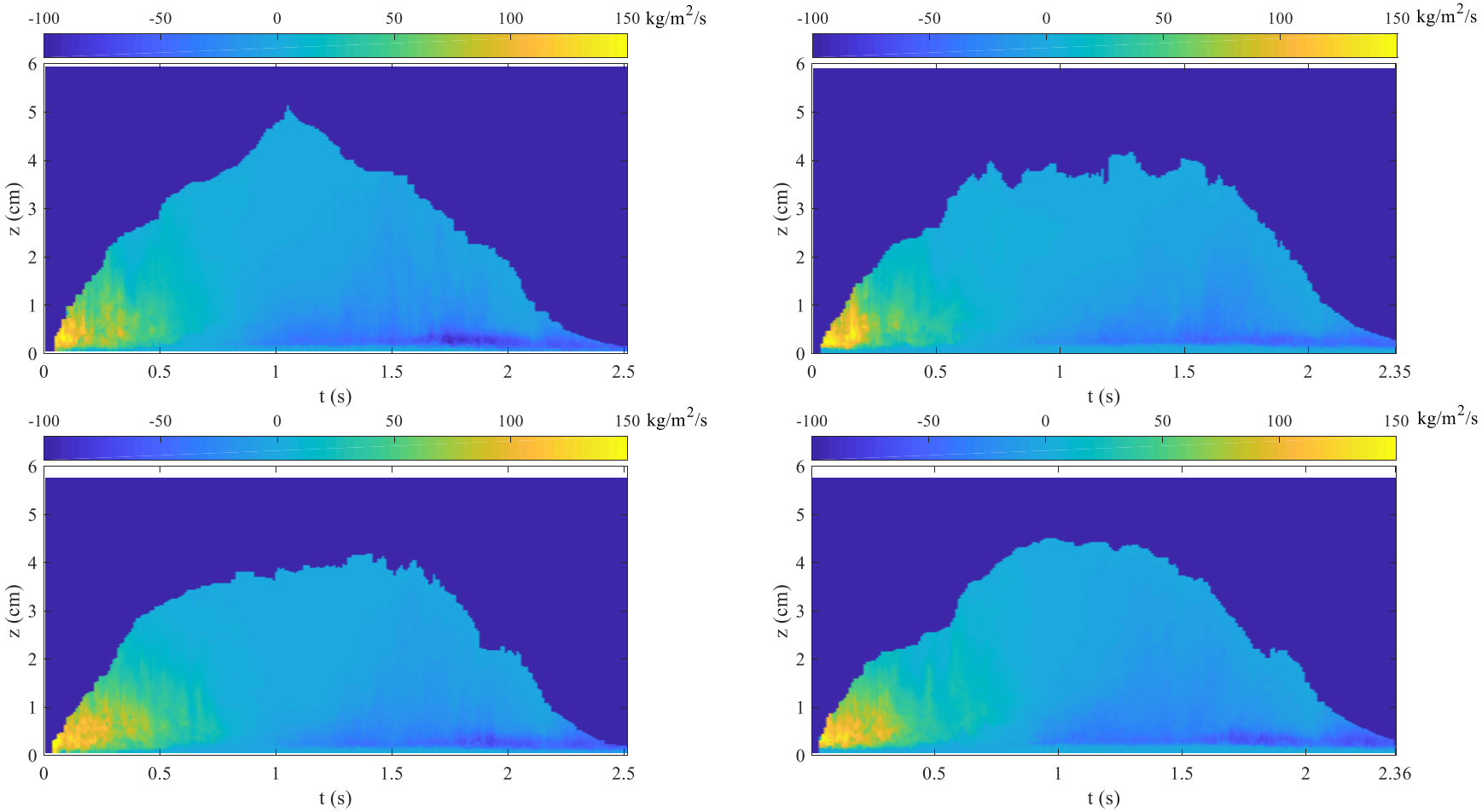

Figure 4-18. Temporal and spatial variation of bed-parallel sediment fluxo of 4 swash events

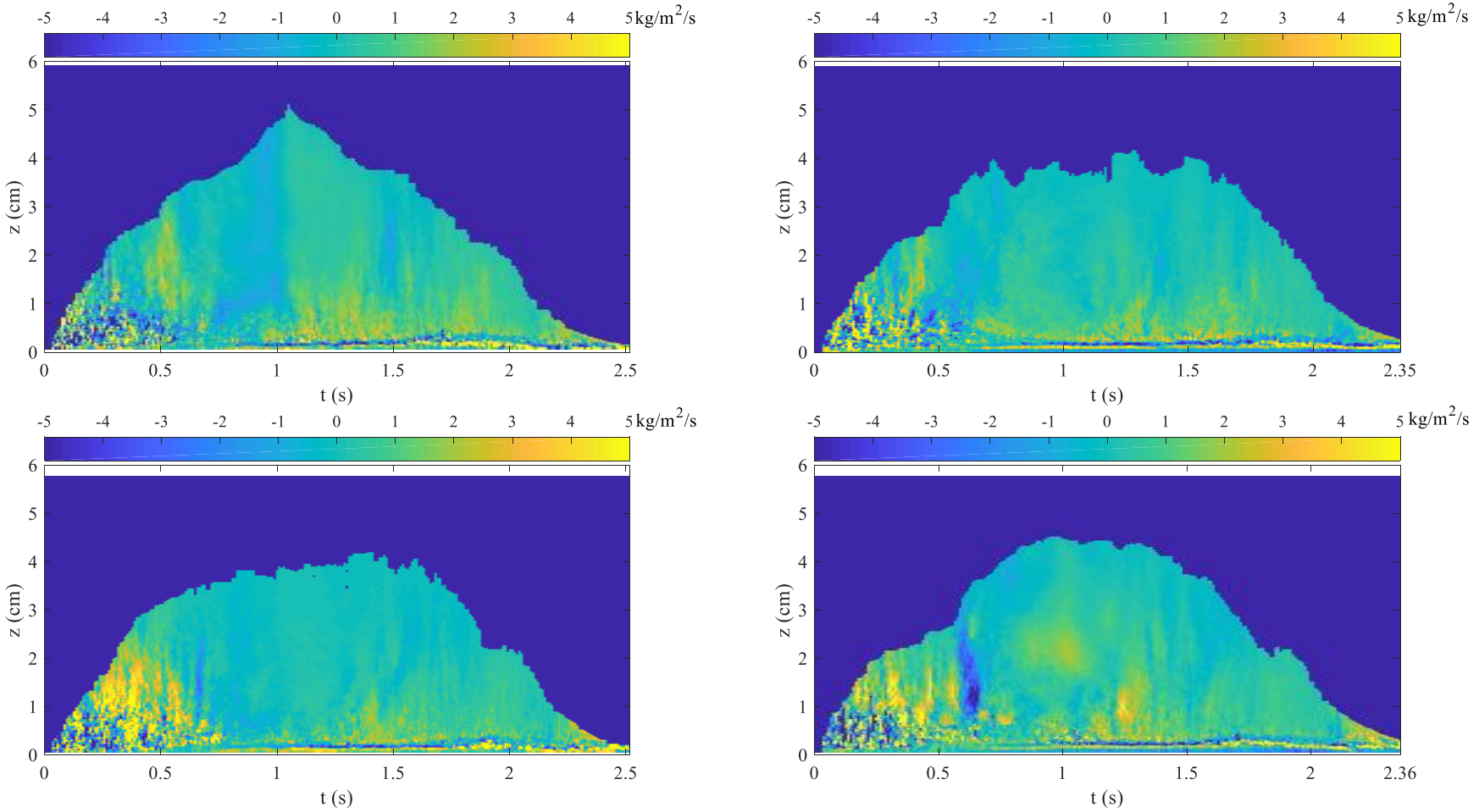

Figure 4-19. Temporal and spatial variation of bed-normal sediment flux of 4 swash events

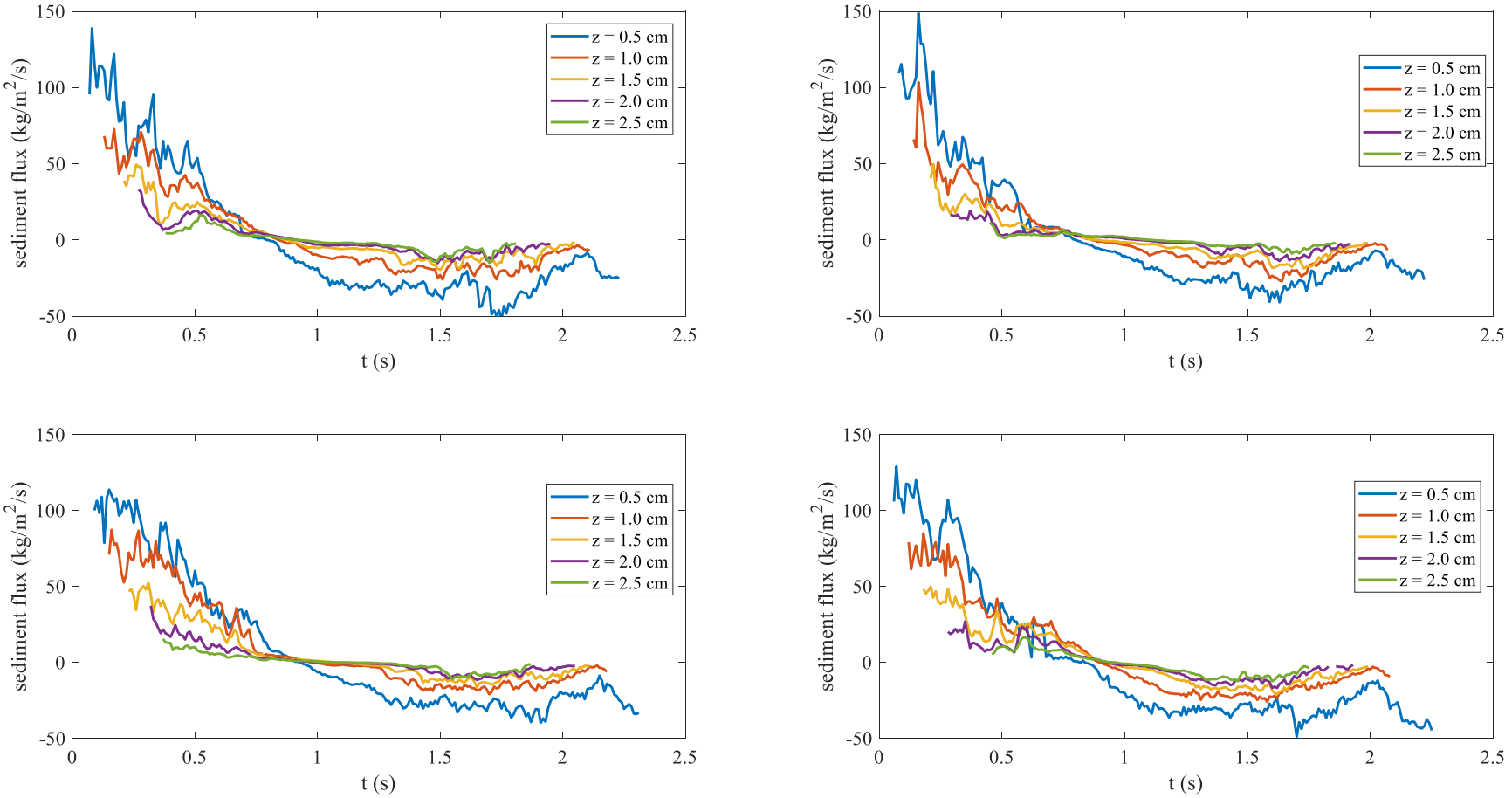

Figure 4-20. Time series of instantaneous sediment flux at several selective elevations of 4 swash events

4.7.2 Time series of instantaneous sediment flux

Fig. 4-20 shows the time series of instantaneous sediment flux of several selective elevations above the initial sand bed at inspection line 5 of 4 swash events. The instantaneous sediment flux generally shows a decreasing-increasing tendency except for that very close to the sand bed. In the vicinity of the sand bed (e.g. z = 0.5 cm), sand re-suspension is obvious leading to the sediment flux grows again in the final backwash. Sediment flux fluctuates significantly except in the flow reversal where the flow is more stable. Fluctuations in the uprush and backwash are suggested due to bore-generated and bed-related turbulence, respectively. Moreover, sediment flux in the upper water column changes more smoothly since the turbulence is not as powerful as that close to the sand bed.

4.7.3 Depth-averaged sediment flux

Depth-averaged sediment flux is shown in Fig. 4-21. The maximum depth-averaged sediment flux occurs in the initial uprush to a magnitude of 120 kg/m^2/s. The depth-averaged sediment flux reduces speedily to zero in the flow reversal. Sediment flux in the upper layers is very weak leading to a near zero depth-averaged sediment flux for most of the backwash. In the final backwash, the magnitude of depth-averaged sediment flux grows to 50 kg/m^2/s due to re-suspension and rapid decrease in the water depth.

4.7.4 Vertical profiles of sediment flux

Vertical profiles of instantaneous sediment flux of 4 swash events are shown in Fig. 4-22. The instantaneous sediment flux grows rapidly from the sand bed, reaching a peak in the lower water column and then decays mildly to the water surface. The maximum sediment flux for both uprush and backwash occurs between z = 0.25 cm and 0.50 cm. Below this level, the small velocity within the lower boundary layer generates a relatively weak sediment flux even though the sediment concentration is very large. In the upper layers where the horizontal bed-parallel velocity is nearly uniform, the sediment flux decreases monotonically with the elevation in the same manner as the sediment concentration. It is evident that sediment flux within the bottom boundary layer dominates both in the uprush and backwash at the very foreshore region. Sediment flux above the boundary layer is weaker than that in the boundary layer by one order of

magnitude. This is in contrast with Horn and Mason (1994) who suggested that suspended load dominates in the uprush and bed load dominates in the backwash.

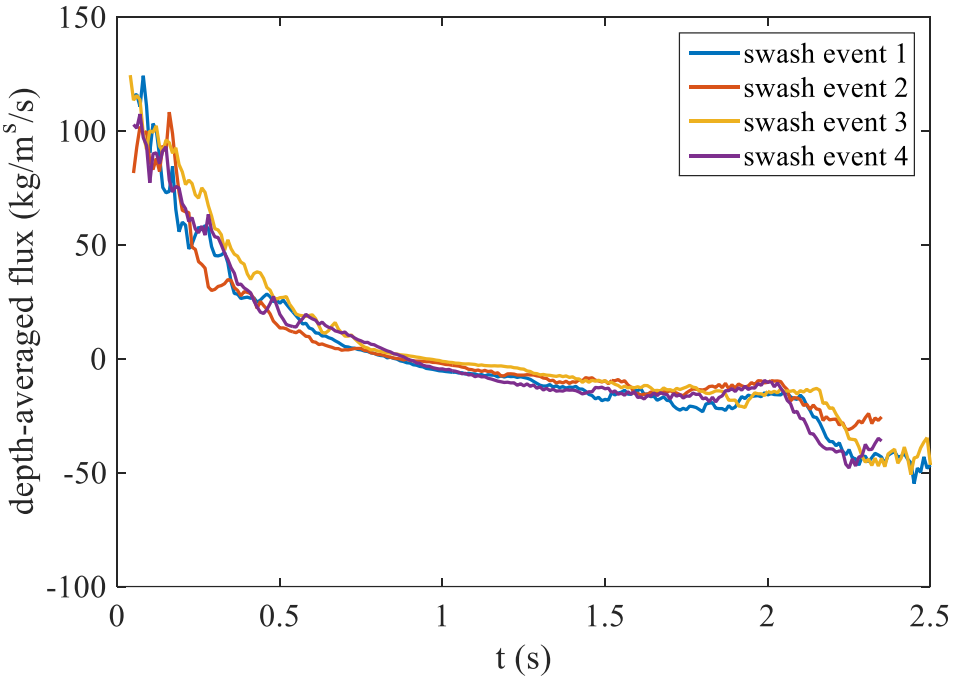

Figure 4-21. Time series of depth-averaged sediment flux of 4 swash events

4.8 Sediment transport load

The instantaneous sediment transport load was evaluated by,

$$Q = \int_{z=0}^{z=h} c(z)u(z)dz \approx \sum_{i=1}^{i=h/d} c_i u_i d \tag{4-5}$$

where i is the index of measurement point counting from the sand bed, d is the vertical distance between two adjacent measurement points. Fig. 4-23 shows the instantaneous sediment transport load of 4 swash events. The instantaneous sediment transport load develops rapidly when the water depth increases. The maximum value appears at $1/10T$ instead of the very initial uprush (since the water depth is very shallow) and then it

decreases with fluctuation until the flow changes its direction. In the backwash, the magnitude of instantaneous sediment transport load exhibits an increasing-decreasing trend. The maximum offshore instantaneous sediment transport load occurs in the early backwash (3/5*T*), slightly earlier than the maximum backwash velocity. The magnitude of maximum uprush instantaneous sediment transport load (1.2 kg/m/s) could be twice as large as the backwash value (-0.6 kg/m/s).

Sediment transport loads are generally divided into suspended load and sheet load. Sheet load transport is usually defined when the volumetric concentration exceeds 0.08 (Bagnold, 1966b). Instantaneous suspended load, Q_{susp}, and sheet load Q_{sheet}, are obtained by integrating instantaneous suspended flux, q_{susp} and sheet load flux q_{sheet} over the vertical as,

$$Q_{susp} = \int_{z=z_s}^{z=h} q_{susp} dz \tag{4-6}$$

$$Q_{sheet} = \int_{z=0}^{z=z_s} q_{sheet} dz \tag{4-7}$$

where, z_s is the elevation of the top of the sheet layer, z = 0 is the instantaneous bed level.

Q_{boun} and Q_{upper} are defined as sediment transport load inside and outside the bottom boundary layer, respectively, in order to investigate the sediment transport in detail. For clarity, this thesis refers to Q_{boun} and Q_{upper} as near bottom load and upper layer load, respectively. They are estimated as,

$$Q_{boun} = \int_{z=0}^{z=z_b} q_{boun} dz \tag{4-8}$$

$$Q_{sheet} = \int_{z=z_b}^{z=h} q_{upper} dz \tag{4-9}$$

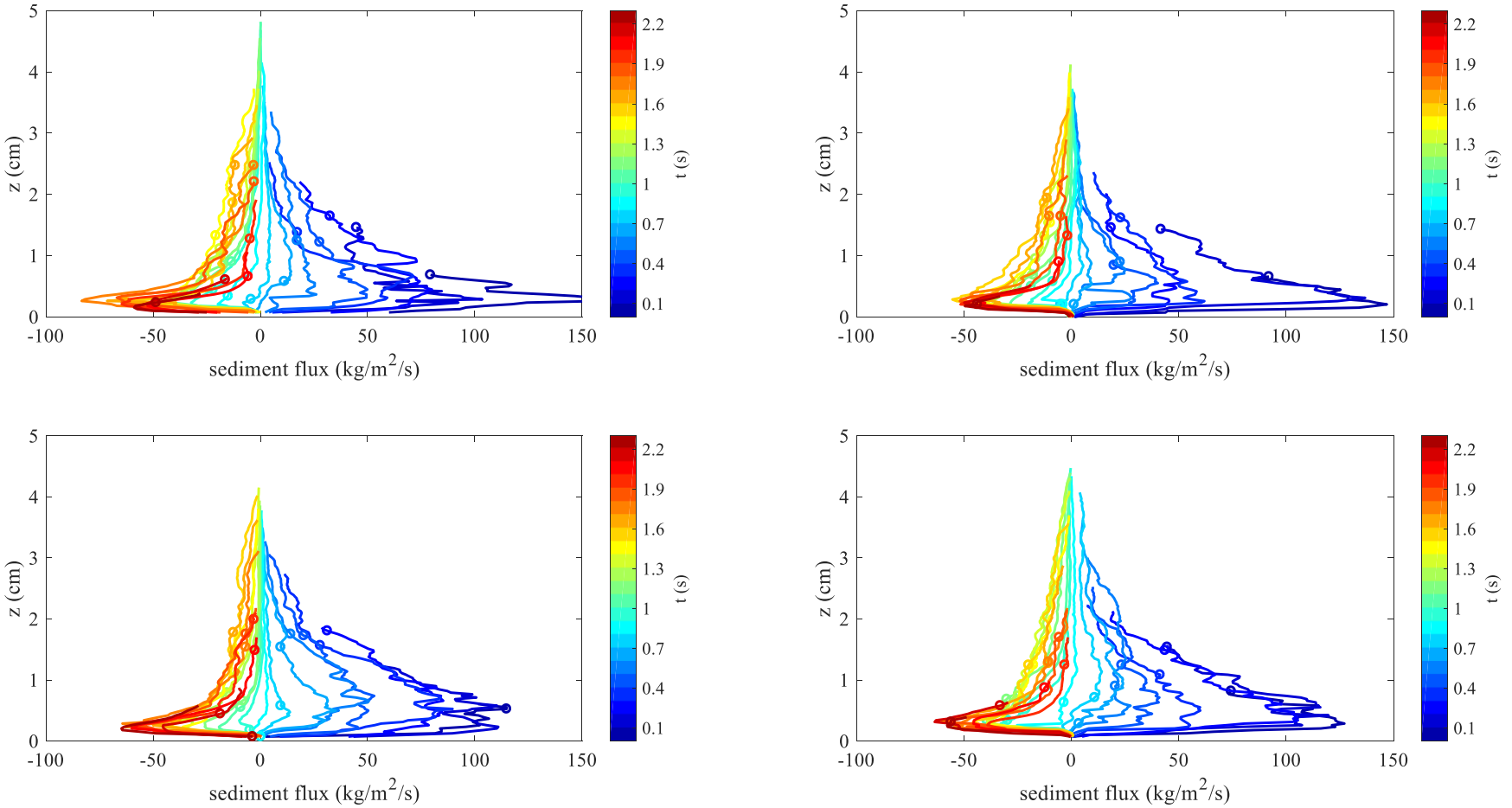

Figure 4-22. Vertical profiles of instantaneous sediment flux (circles indicate the local boundary layer thickness)

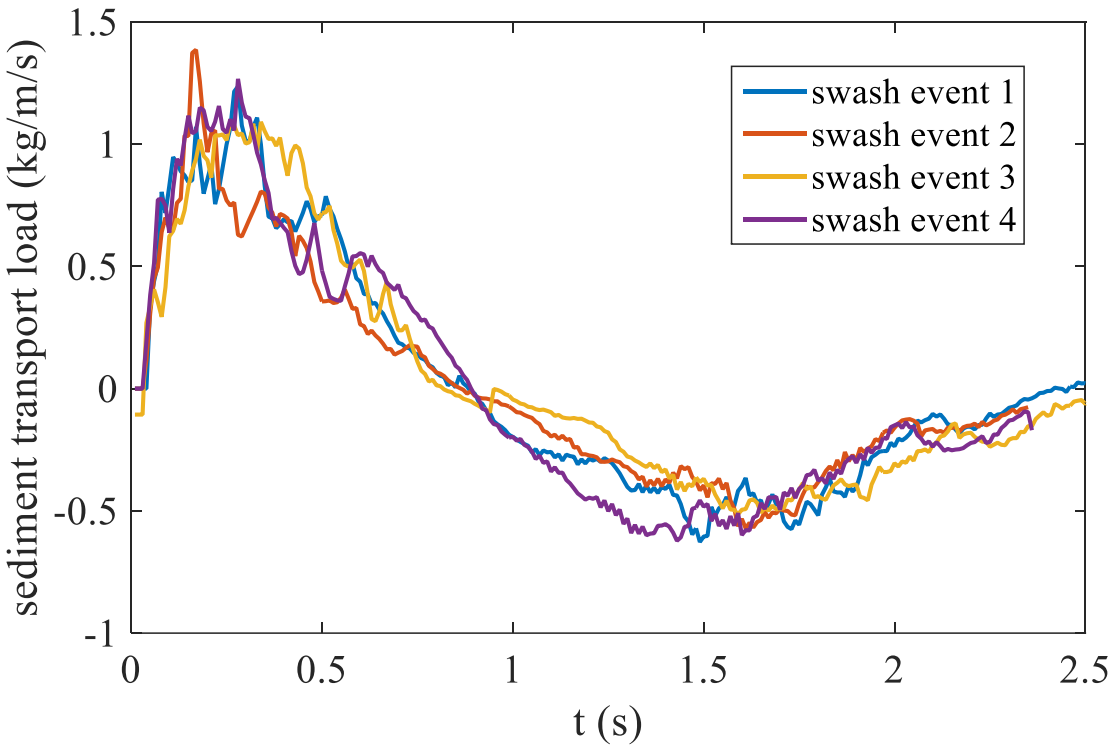

Figure 4-23. Instantaneous sediment flux at several selective elevations at inspection line 5 of 4 swash events

where, z_b is the elevation of the top of the instantaneous bottom boundary layer, q_{boun} and q_{upper} are the instantaneous sediment flux inside and outside the bottom boundary layer, respectively.

4.8.1 Sheet layer thickness

Fig. 4-17 plots the instantaneous sheet layer thickness along with the boundary layer thickness and the water level of 4 swash events. The instantaneous sheet layer thickness is much thinner than the bottom boundary layer thickness. During the uprush, the instantaneous sheet layer thickness is approximately 1/3 of the bottom boundary layer thickness. The maximum sheet layer thickness is about 0.6 cm, occurring in the middle uprush. Sheet load transport almost vanishes after the flow reversal if considering the change of instantaneous bed level. This is because that advection is the main source of sand passing through the measurement location and sand particles deposit rapidly so

that sediment concentration decays rapidly after the flow reversal. Moreover, the re-suspension effect is not powerful enough to make a sheet load transport in the late backwash.

4.8.2 Instantaneous sediment transport

a. Sheet load and suspended load

Fig. 4-24 shows the time series of instantaneous sediment transport, sheet load and suspended load. The suspended load transport dominates both in the uprush and backwash phase. The sheet load transport only occurs during the initial 2/3 of the uprush. The maximum instantaneous sheet load transport takes place in the middle uprush with a magnitude around 0.5 kg/m/s and it is much smaller than the maximum instantaneous suspended load transport (0.7 kg/m/s).

b. Near bottom load and upper layer load

Fig. 4-25 indicates that the near bottom transport dominates during the entire swash event, especially in the early uprush and late backwash where sediment transport almost takes place within the bottom boundary layer. The maximum instantaneous near bottom sediment transport load could be similar with the total instantaneous load while the maximum instantaneous upper layer transport load is only around 0.3 kg/m/s.

4.8.3 Cumulative sediment transport

Time series of instantaneous cumulative sediment transport loads are shown in Fig. 4-26. They are estimated by,

$$M_{cumu} = \int_{o}^{t} Q_{*} dt \tag{4-10}$$

where, M_{cumu} refers to cumulative load of different sediment transport modes. Q_{*} refers to different instantaneous loads sediment transport modes. For clarity, Table 4-3 indicates the detailed value of total and net cumulative sediment transport loads of each mode. The total cumulative sediment transport load grows rapidly and reaches its peak (around 50 kg/m/s) before flow reversal. When the flow starts to go offshore, the total

cumulative sediment transport load decays mildly and it ends at a slightly positively value (O < 10 kg/m/s). Since the sheet load transport mainly occurs in the uprush, it contributes to a positive (onshore) sediment movement with a magnitude of approximately 10 kg/m/s. The cumulative suspended load transport generally has a similar tendency with the cumulative total sediment transport while it makes a negative (offshore) contribution about -10 kg/m/s. it is suggested that the suspended load during backwash is slightly larger than that of uprush because the duration of backwash is 1.5 times as long as that of uprush although the instantaneous sediment flux in the uprush is more significant.

The cumulative near bottom sediment transport load shows a similar trend with the instantaneous cumulative sediment transport load as well. The maximum cumulative near bottom sediment transport load is very close to that of the cumulative suspended load transport (30~40 kg/m/s) and the onshore near bottom sediment transport is greater than the offshore component. The upper layer load transport is relatively much weaker. The maximum upper layer load transport is around 10 kg/m/s and the net value is close to zero.

Vertical profiles of cumulative sediment transport loads are estimated by integrating sediment transport load at different elevations over time,

$$Q_{cumu}(z) = \int_{t=0}^{t=T} Q(z)dt \tag{4-11}$$

The gross cumulative sediment transport is calculated by sum the absolute value of the onshore and offshore components. Fig. 4-27 indicates that the cumulative sediment loads of uprush, backwash and gross grow from the bed to some level and then drop gradually till the water surface. The maximum values of cumulative sediment transport load of uprush, backwash and gross occur at z = 0.2 cm to z = 0.3 cm, with magnitude around 1.2 kg/m/s, 2.0 kg/m/s, 3.0 kg/m/s, respectively. Cumulative net sediment transport load is offshore in the vicinity of the bed, onshore in the middle of the flow region and almost zero in the upper layers. Ruju et al. (2016a) reported a unidirectional onshore cumulative sediment transport profile measured in the swash zone over the

coarse sand beach from a prototype laboratory flume under irregular waves. It is suggested that the cumulative sediment transport profile is much depended on the measurement location and flow conditions.

Except for the sheet load transport, each mode of sediment transport is a combination of two opposite large components (onshore and offshore). The net sediment transport of each load is a small sum and the magnitude difference between the one-way load and net sediment transport could be as large as one order. The magnitude of net sediment transport load at each elevation is approximately half of the one-way sediment transport load.

4.8.4 Net sediment transport

In order to verify the reliability of the measurement system, the net sediment transport is compared to the mass change evaluated from the bed level evolution. The net sediment transport (Δm) between the inspection line 1 and 10 is estimated by,

$$\Delta m = m_{10} - m_1 = \int_{t=o}^{t=T} (Q_{10} - Q_1) l dt \tag{4-11}$$

where m_1 and m_{10} are the net sediment transport at inspection line 1 and 10 respectively. Q_1 and Q_{10} are the instantaneous sediment transport loads at inspection line 1 and 10, respectively. l is the path length which has been introduced in Chapter 2. Therefore, Δm is the net mass change which has the unit of kg. The mass change evaluated from the be level evolution (ΔM) is estimated by,

$$\Delta M = \rho_s V = \rho_s l L \Delta z (1 - p_w) \tag{4-12}$$

where ρ_s is the density of sand particles ($\rho_s = 2650$ kg/m^3). L is the distance between the 1st and 10th inspection line (L = 2.4 cm). Δz is the change of bed level of each swash event and it is assumed that the bed level change between the two inspection lines is uniform. p_w is the water ration of the local sand bed. Table 4-4 illustrates the

comparison of Δm and ΔM of 4 swash events. The net sediment transport estimated by the measurement system is smaller than that evaluated by the bed level change by at most 20%. This mismatch appears to be related to both of the error in bed level change and sediment flux. On one hand, the two dimensional bed profile is not entirely uniform. Due to the effect of the El-sheet and glass side wall, the bed level in the two sides is slightly lower than that in the middle. Therefore, assuming a uniform two dimensional bed level will underestimate the net mass change since the reference bed level is measured close to the side wall. On the other hand, net sediment load is a small difference of two large opposite components; any measurement error of instantaneous sediment flux is potentially leading to the change of net sediment transport. Moreover, sediment flux close to the water surface is removed due to the 'black shadow' which has been introduced before, and the 'black shadow' mainly appears in the backwash, therefore, offshore transport is under estimated resulting in a overestimation of the net sediment transport. However, due to the nature of difficulty in the quantification of sediment transport in the swash zone and the small magnitude of sediment transport in the present experiments, the current comparison results is considered as reasonable and the measurements are quite reliable (Wu et al., 2016).

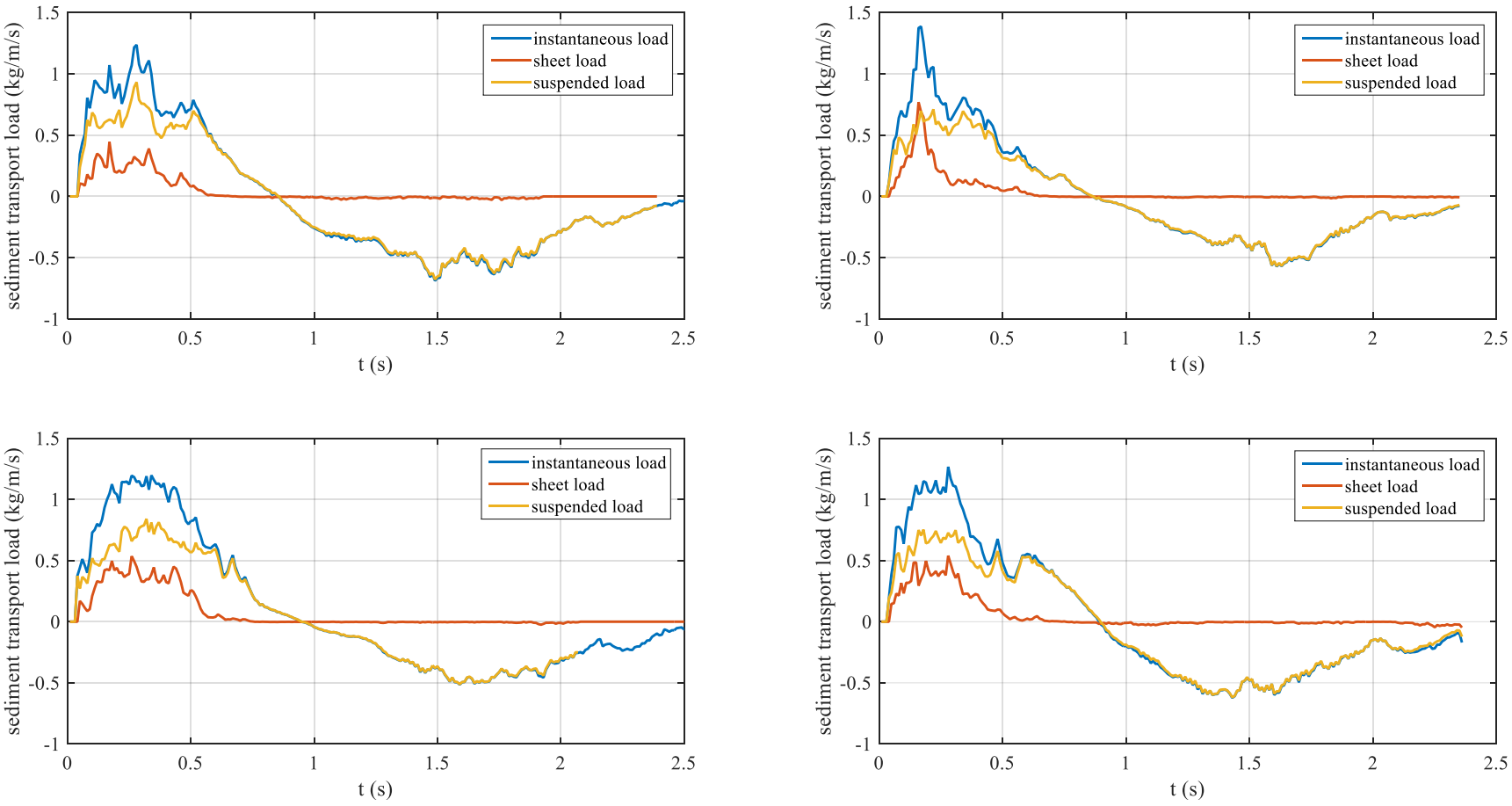

Figure 4-24. Time series of instantaneous sediment transport load, sheet load and suspended load

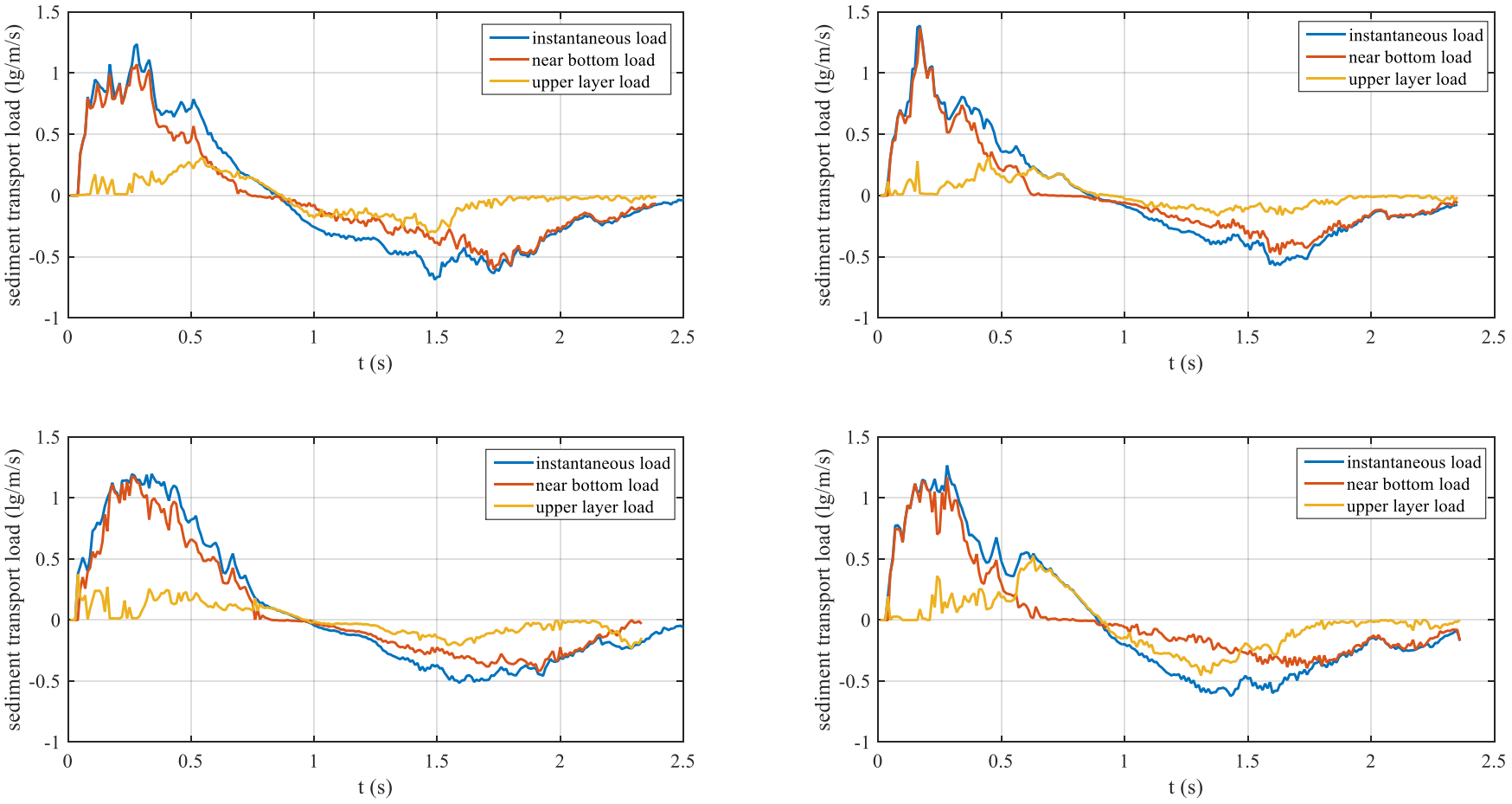

Figure 4-25. Time series of instantaneous sediment transport load, near bottom load and upper layer load

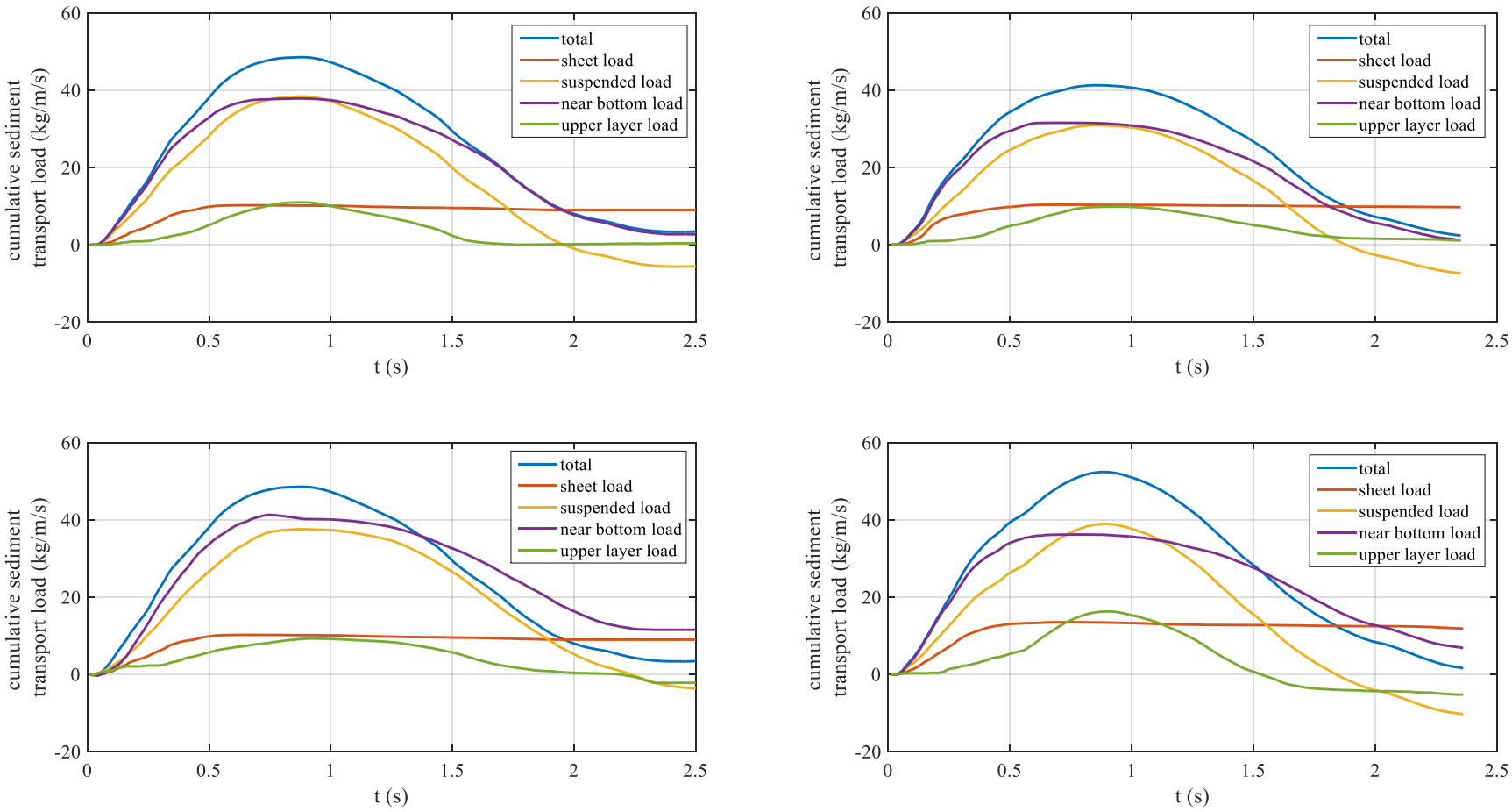

Figure 4-26. Time series of instantaneous cumulative sediment transport load, sheet load, suspended load, near bottom load and upper layer load

Table 4-3. Cumulative sediment transport loads

unit: kg/m/s	Uprush				Backwash				Net			
	case number											
	1	2	3	4	1	2	3	4	1	2	3	4
Total	48.49	41.29	49.37	52.38	-45.02	-38.92	-41.66	-50.83	3.47	2.37	7.71	1.55
Sheet load	10.24	10.39	11.95	13.51	-1.24	-0.64	-0.50	-1.65	9.00	9.75	11.45	11.86
Suspended load	38.25	30.90	37.42	38.87	-43.78	-38.32	-41.18	-49.26	-5.53	-7.42	-3.76	-10.39
Near bottom load	37.64	31.58	40.21	36.21	-34.92	-30.32	-28.67	-29.41	2.72	1.26	11.54	6.80
Upper layer load	10.85	9.71	9.16	16.17	-10.10	-8.60	-12.99	-21.42	0.75	1.11	-3.83	-5.25

Table 4-4. Comparison of net sediment transport between the estimates from bed level change

Case number	1	2	3	4
Δm (10-3 kg)	0.55	0.85	0.51	0.56
ΔM(10-3 kg)	0.45	0.76	0.49	0.51
Error (%)	-17.54	-11.20	-3.77	-8.62

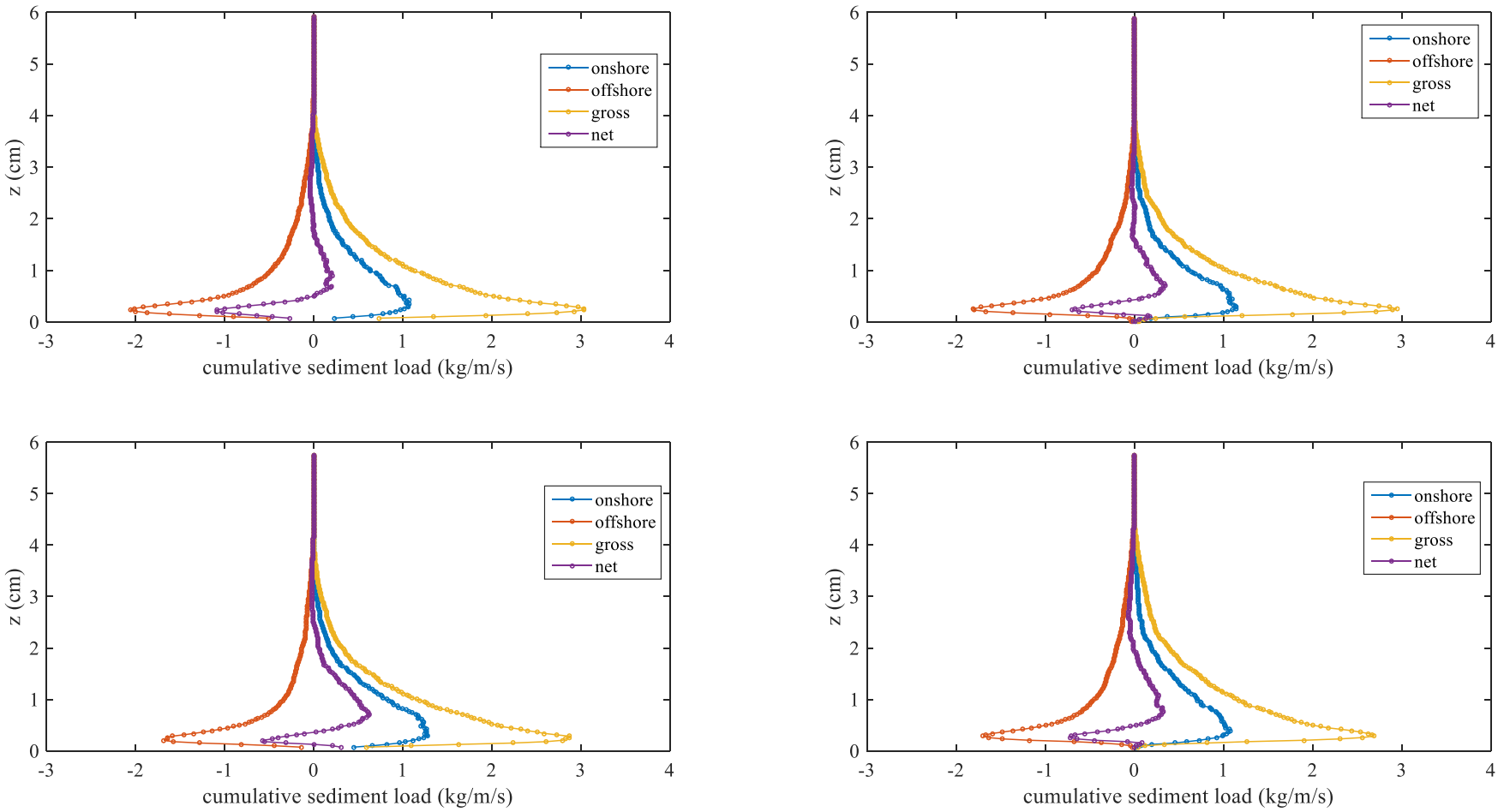

Figure 4-27. Vertical profiles of cumulative (time-integrated) onshore, offshore, gross and net sediment transport loads

Chapter 5 Intra-swash Sediment Transport Models

5.1 Introduction

It is widely acknowledged that measurement of sediment transport in the swash zone is extremely difficult, thus the numerical models provide a very valuable insight on this important topic (Braganti et al., 2016). However, validation of each numerical models is pretty important which further requires the improvement of measurement capability for reliable datasets. Prediction of intra-swash sediment transport has been attempted historically by energetics-type formulation, i.e. the most widely used Bagnold's energetics type model and the Meyer-Peter and Müller's Shields parameter model (Chardón-Maldonado et al., 2016). The Bagnold's energetics type model generally relates the total, suspended and bed load transport to the velocity of some power. And sediment transport in the Meyer-Peter and Müller's Shields parameter model is proportional to the product of flow velocity and bed shear stress. If the bed shear stress is arose from the quadratic law then the sediment transport rate in the Meyer-Peter and Müller's model is also linked to the cubic velocity. Both of the Bagnold's energetics type model and the Meyer-Peter and Müller's Shields parameter model are not developed for swash zone but for steady, unidirectional flow. They are popularly used for both scientific study and engineering application even though the conditions are not met in the swash zone.

A better representation for the sediment transport in the swash zone is process-based numerical models. Instantaneous sediment transport and morphological evolution are usually estimated by coupling to the hydrodynamic models while the output might be significantly related to the degree of coupling (i.e. uncoupled, weakly or fully). On the other hand, the degree of coupling determines the computational time and it may vary from O(1) min to O(10) days(Braganti et al., 2016). Various numerical techniques have been devised and practice for modeling hydrodynamics and sediment transport in the swash zone including the nonlinear shallow water equation (NLSWE) (Kelly and Dodd, 2010; Zhu et al., 2012; Zhu and Dodd, 2013, 2015; Hu et al., 2015) which is a depth-averaged model and cannot simulate the detailed flow structure; Boussinesq type

equations (Rakha et al., 1997; Karambas, 2003; 2006; Pedrozo-Acuna et al., 2006, 2007;), large-eddy simulation (LES) (Hirt and Nichols, 1981; Klostermann et al., 2013, Zhang and Liu, 2008) and Reynolds-Averaged Navier Stokes equations (RANS) (Lin and Liu 1998; Losada et al., 2008; Hsu et al., 2002).

One critical problem is that all of the aforementioned numerical models use the empirical relationship to couple the sediment transport to the swash flow parameters. Zhu and Dodd (2013) examined various empirical sediment transport formulas and find that simulation result is significantly changed by using different formulas for the same case. Li et al. (2017) also indicate that limitations of empirical sediment transport formulas for shallow water are significant and the resulting error might be up to factor 10^5 in some cases. Since the widely used relationship for coupling sediment transport and flow parameters is Bagnold's energetics type model and the Meyer-Peter and Müller's Shields parameter model, and their derivatives, their capability in the swash zone are investigated on the basis of the high-resolution measurement of the present study.

5.2 Logarithmic model

Since the main forcing parameter of most sediment transport models is the bed shear stress and therefore the Shields number, the logarithmic model is used to evaluate the intra-swash bed shear stress. The logarithmic model was initially established for fully developed, steady boundary layer flows, but it has been applied successfully to estimate bed shear stress under unsteady flows in the surf and swash zones (Cox et al., 1996; Inch et al., 2015; O'Donoghue et al., 2010; Puleo et al., 2012; Ruju et al., 2016). In this section, the highly resolved bed-parallel velocity profiles are applied to the logarithmic model to investigate the bed shear stress over the mobile sand bed for further investigating sediment transport models in the swash zone. The von Karman-Prandtl relationship describes the logarithmic velocity profile in the boundary layer as,

$$u(z) = \frac{u_*}{\kappa} \ln\left(\frac{z - d_*}{z_0}\right) \tag{5-1}$$

where $u(z)$ is the cross-shore velocity, which is taken as the bed-parallel velocity in this study. u_* is the friction velocity, κ is the von Karman's constant ($\kappa = 0.4$), d_* is the displacement distance ($d_* = 0.7d_{50}$) and z_0 is the height above the bed at which velocity is assumed to be zero. z_0 equals to $k_s/30$, where k_s is the equivalent Nikuradse roughness.

The model is valid for $30 < z^+ < 1200$ (Wei and Willmarth, 1989; Pope, 2000), where z^+ is the non-dimensional elevation defined as $z^+ = \frac{|u_*|z}{\nu}$, and ν is the kinematic viscosity ($\nu = 10^{-6}\ m^2/s$). The previous studies usually perform a least squares regressions between the velocity profile and $ln(z - d_*)$. The square of the correlation coefficient in the regression is used to accept or reject the logarithmic model and the slope of the least squares regression is used to derive the u_*. The bed shear stress τ therefore can be estimated by,

$$\tau = \rho {u_*}^2 \tag{5-2}$$

where ρ is the water density. The equivalent roughness is able to be deduced from the intercept with the y-axis of the regression. Typically, only a few current velocity meters are available in most of the field experiments thus the bed shear stress is usually estimated by the quadratic drag law as,

$$\tau = 0.5\ \rho f |u_f| u_f \tag{5-3}$$

Where u_f is the fluid velocity in the free stream (beyond the bottom boundary layer) and f is the empirical friction factor typically O(10^{-3} to10^{-2}) (Conley and Griffin, 2004; Hughes, 1995; Puleo and Holland, 2001; Raubenheimer et al., 2004). When the velocity profiles are available, the friction factor could be estimated by integrating Eqs. 5-2 and 5-3 as,

$$f = \frac{2u_*|u_*|}{u_f|u_f|} \tag{5-4}$$

In the previous studies, the least squares regression is often applied to a constant elevation or the elevation where velocity measurement is available. However, it should be noted that the elevation of velocity profile can significantly affect the regression and therefore the bed shear stress if it is higher than the bottom boundary layer. Even though the thickness of bottom boundary layer is determined through the velocity gradient in the previous chapter, velocity profiles from the instantaneous bed level up to different elevations are employed to investigate bed shear stress as well as the effect of different upper limit of the elevation. The lowest five velocity data points are always included in the velocity profiles for regression and the upper limit of the velocity profile is the boundary layer thickness.

The regression results of 4 swash events are shown in Fig. 5-1. Past studies often use correlation coefficient (R^2) of 0.9 or 0.95 to judge the capability of the logarithmic model for ensemble average swash events (e.g. O'Donoghue et al., 2010; Puleo et al., 2012) and R^2 = 0.7 or 0.8 for individual swash events (Inch et al., 2015; Ruju et al., 2016b; Puleo et al., 2016). Fig. 5-1 shows that the correlation coefficient is larger than 0.8 regardless the limit elevation of velocity profiles, which means that the velocity profile up to the boundary layer thickness fits the logarithmic model very well and the estimation of the bottom boundary layer thickness is reliable. The non-dimensional elevation z^+ is generally smaller than 1000 and even though it grows when the limit elevation used in the regression increases, the magnitude is still weaker than 1200 meaning that all of the regressions are within the valid range of the logarithmic model. Moreover, the distribution of bed shear stress estimated from velocity profiles with different upper limit elevations does not show large vertical variation except for a short duration in the middle backwash, further indicating that the boundary layer thickness is not overestimated. Therefore, it is considered that the estimation of boundary layer depth is reliable. Previous studies often use a constant elevation to do the least squares regression and find that the velocity profiles during the flow reversal and the early backwash do not conform to the logarithmic model (Inch et al., 2015; Puleo et al., 2012).

It is because the flow close to the sand bed changes direction earlier than that in the upper layer. So that velocities are negative close to the bed and positive in the upper layers when the flow starts to go reversal, leading to the failure of the model, which has also been proposed by O'Donoghue et al. (2010). In the early backwash, velocities are relatively low and the boundary layer is not fully developed hence using a constant elevation much larger than the local instantaneous boundary layer thickness must result in a poor correlation coefficient. Therefore, it is necessary to determine the bottom boundary layer thickness before conducting the least squares regression instead of setting a constant elevation when using the logarithmic model. It is useful for obtaining a more complete bed shear stress history.

The equivalent roughness is more sensitive to the variation in the limit elevation of the velocity profiles since it is the intercept with the *y*-axis and much affected by the variation of the data used for regression. Moreover, velocity profiles in this study are instantaneous value without any post-processing, such as moving averaging and ensemble averaging, therefore fluctuation of the velocity profile is very large for some phases and the regressing result could be modified significantly. The equivalent roughness develops during the uprush and decays during the backwash along with the increase in the limit elevation while the magnitude ranges between 0.01 and 0.05 m in most of the swash phases.

5.2.1 Bed shear stress and Shields parameter

Based on the above evidence that the boundary layer determination is reliable, it is assumed that the instantaneous bed shear stress could be estimated from the logarithmic model with velocity profiles up to the local boundary layer height. Fig. 5-2 shows the instantaneous bed shear stress of 4 swash events. The maximum bed shear stress occurs in the initial uprush accompanied by the bore arrival and then the bed shear stress decays gradually until the flow reversal. Previous studies usually present a monotonous decreasing tendency in the instantaneous bed shear stress during the backwash.In the present study, it is found that the bed shear stress firstly grows gently, reaching a peak in the middle backwash and decreases after that till the end of the swash run. One possible reason might be that the very late backwash is not measured due to the

limitation of the traditional instruments. The magnitude of maximum bed shear stress during the uprush and backwash is similar, around 20 to 30 N/m^2.

The non-dimensional bed shear stress (Shields parameter) is estimated by,

$$\theta = \frac{\tau}{\rho(s-1)gd_{50}} \tag{5-5}$$

where g is the gravitational acceleration. The Shields parameter ranges from 0 to 14, with the maximum value appears in the initial uprush and middle backwash. The tendency of bed shear stress and Shields parameter among different swash events are identical while the magnitude varies slightly mainly due to that the dam-break flow was generated hand-operated.

5.2.2 Equivalent roughness

For steady unmovable bed, bed roughness ought to be a constant value while O'Donoghue et al. (2010) reported that the k_s ranges 2 to 10 times d_{50} for their unmovable rough bed experiments. Here, k_s varies over the swash cycle ranging from $100d_{50}$ to $150d_{50}$ (Fig. 5-3). Major difference is that their study was carried out on unmovable bed while the present experiment was conducted on movable bed, so it is reasonable that a larger k_s appears in the present study. Moreover, the logarithmic model is very sensitive to the choice of limit elevation of the velocity profiles as indicated above. The logarithmic model was fitted to the velocity measurements in the range 0.45 cm < z < 1.15 cm only including 5 data points in O'Donoghue et al. (2010) but from the instantaneous bed level up to the local boundary layer height with much dense data points in the present study.

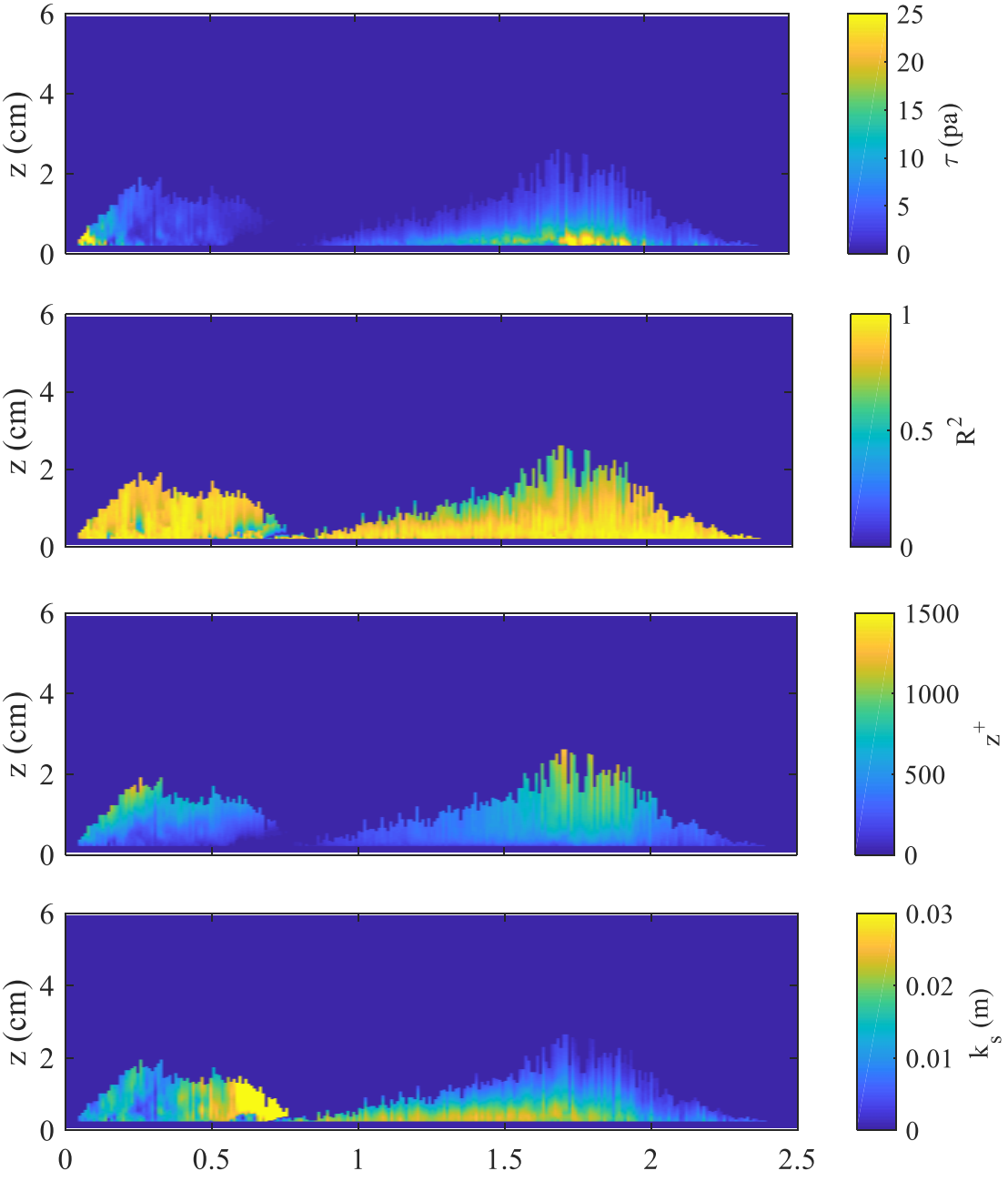

Figure 5-1. Instantaneous bed shear stress, correlation coefficient, non-dimensional elevation and equivalent roughness estimated from the logarithmic model by using velocity profiles up to different limit elevations of 4 swash events

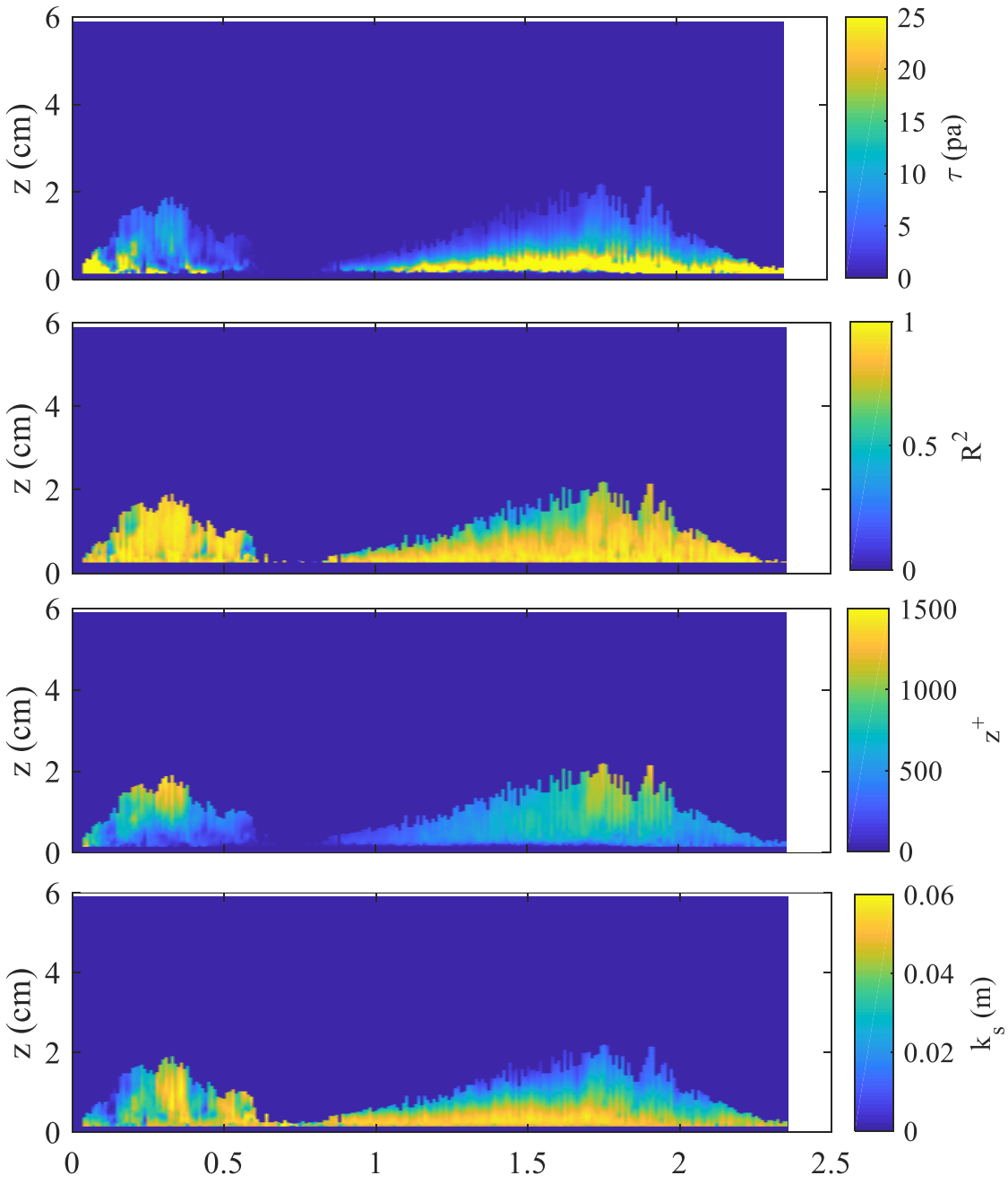

Figure 5-1 (continued). Instantaneous bed shear stress, correlation coefficient, non-dimensional elevation and equivalent roughness estimated from the logarithmic model by using velocity profiles up to different limit elevations of 4 swash events

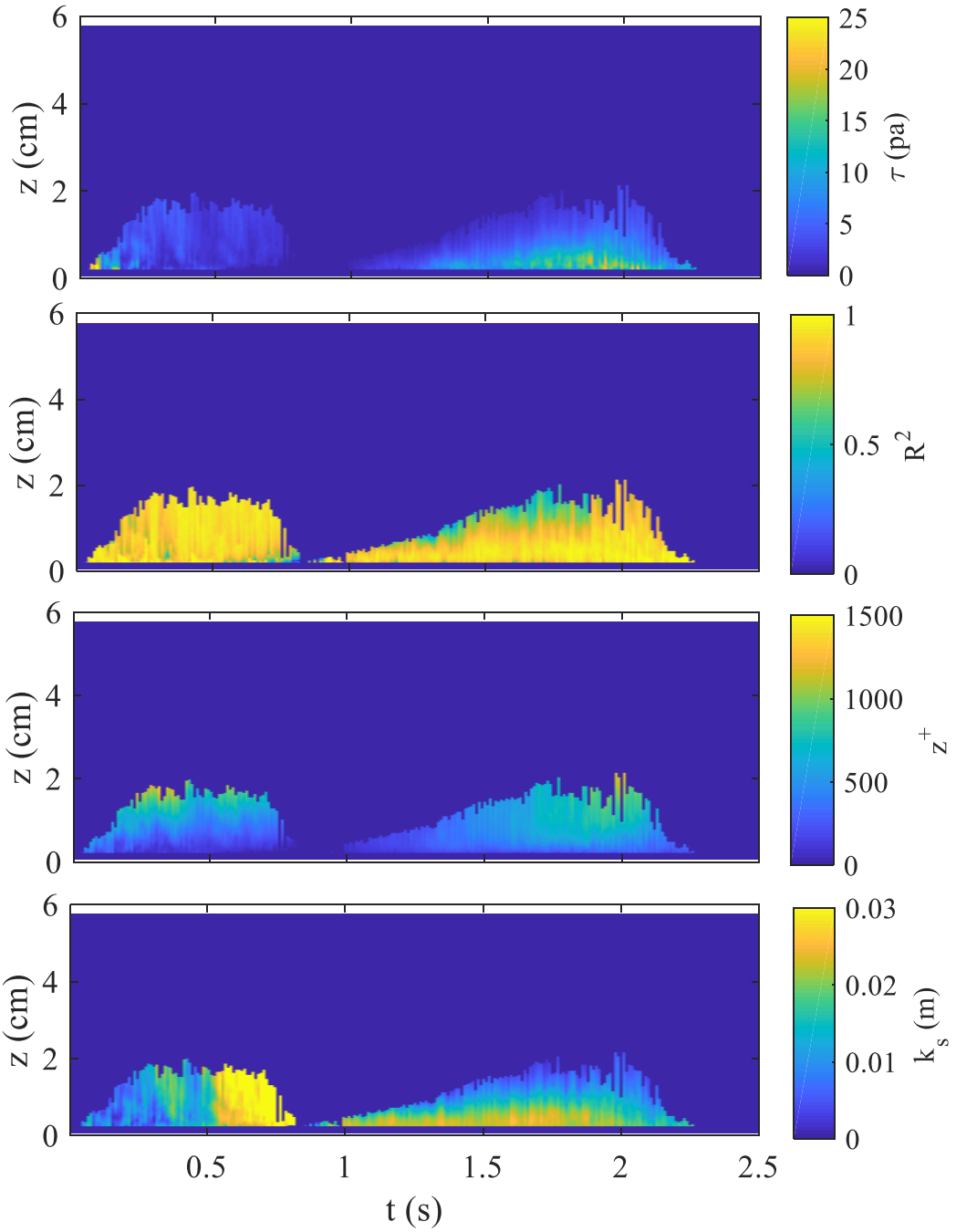

Figure 5-1 (continued). Instantaneous bed shear stress, correlation coefficient, non-dimensional elevation and equivalent roughness estimated from the logarithmic model by using velocity profiles up to different limit elevations of 4 swash events

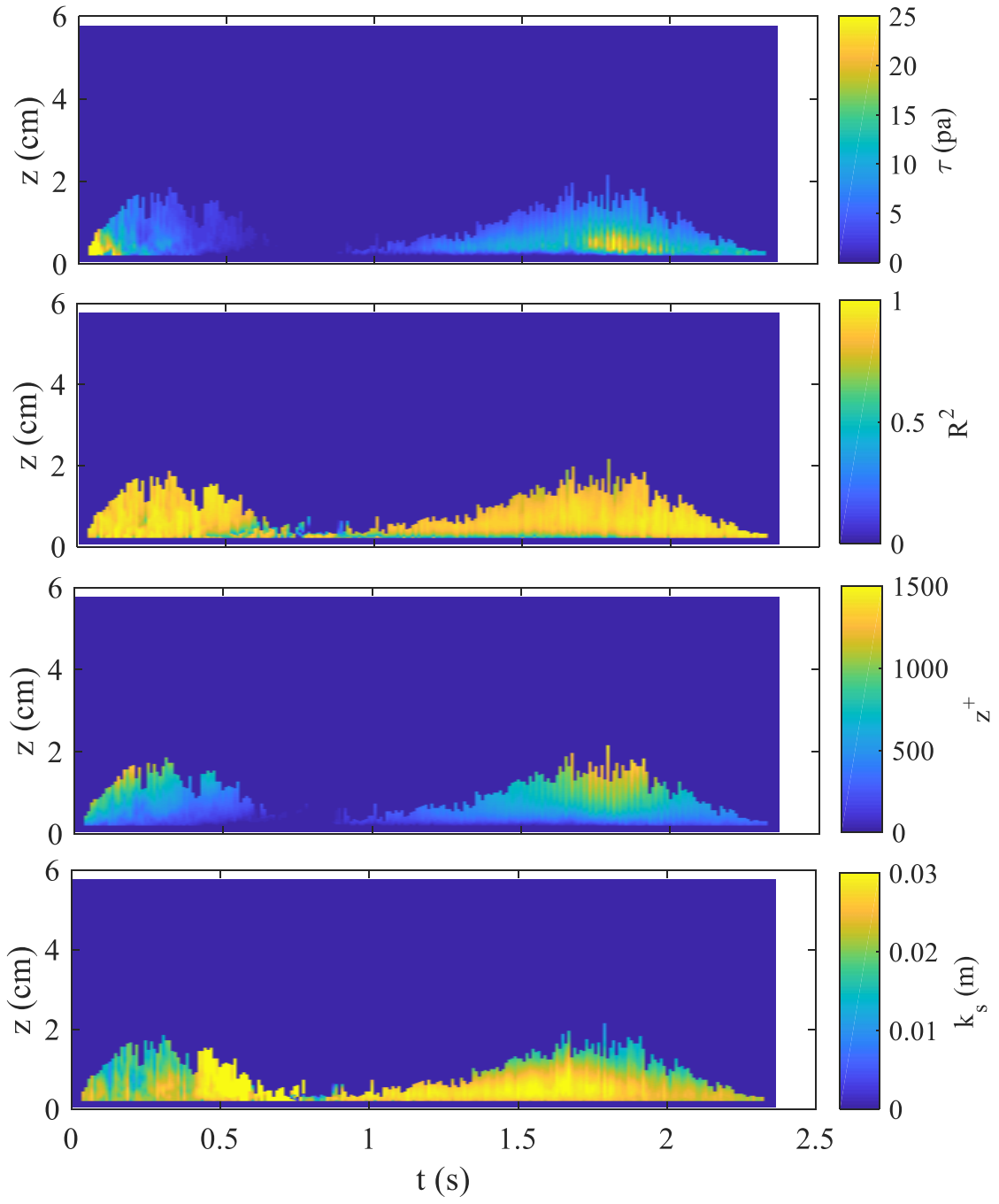

Figure 5-1 (continued). Instantaneous bed shear stress, correlation coefficient, non-dimensional elevation and equivalent roughness estimated from the logarithmic model by using velocity profiles up to different limit elevations of 4 swash events

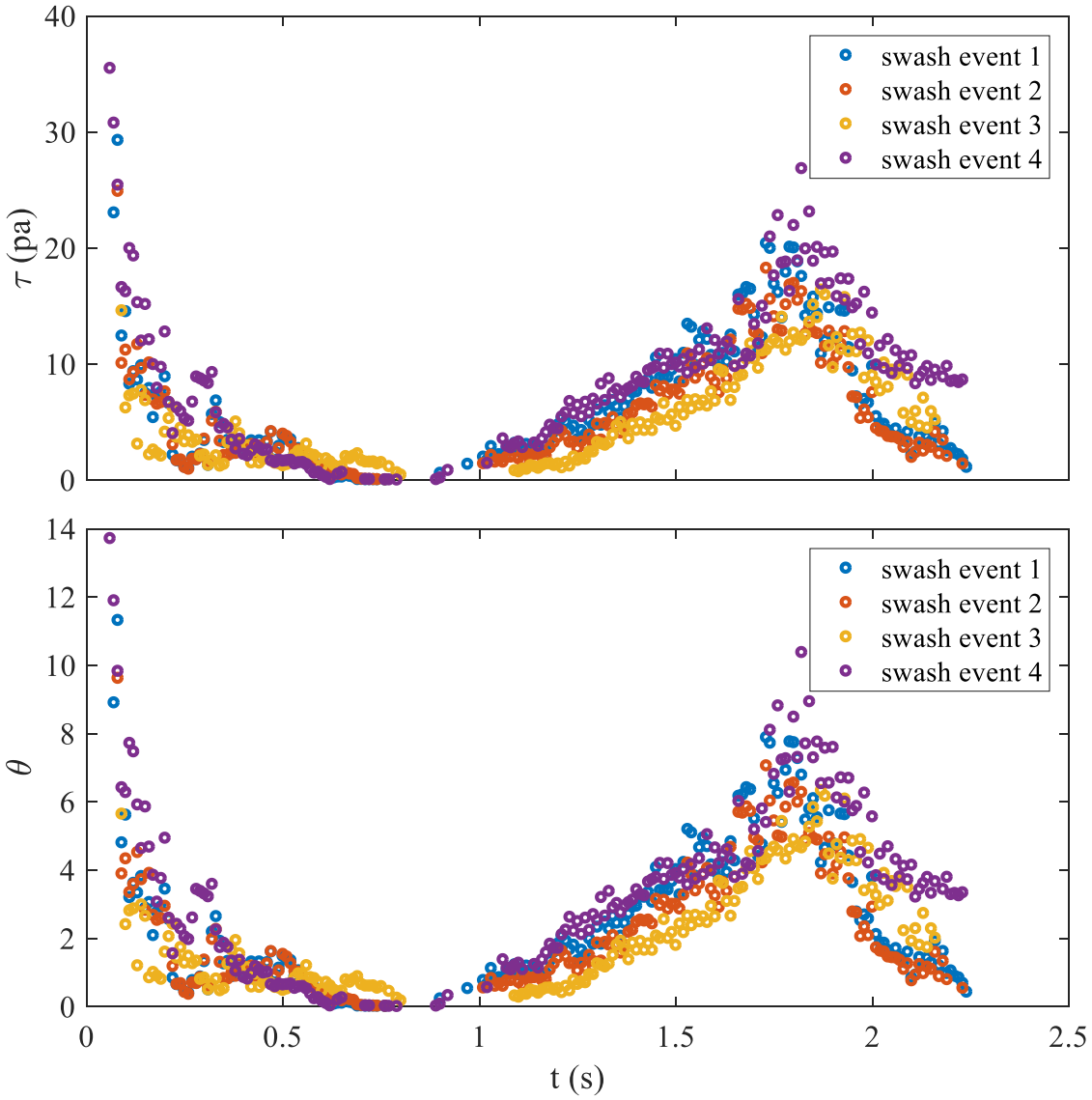

Figure 5-2. Times series of bed shear stress and Shields parameter of 4 swash events

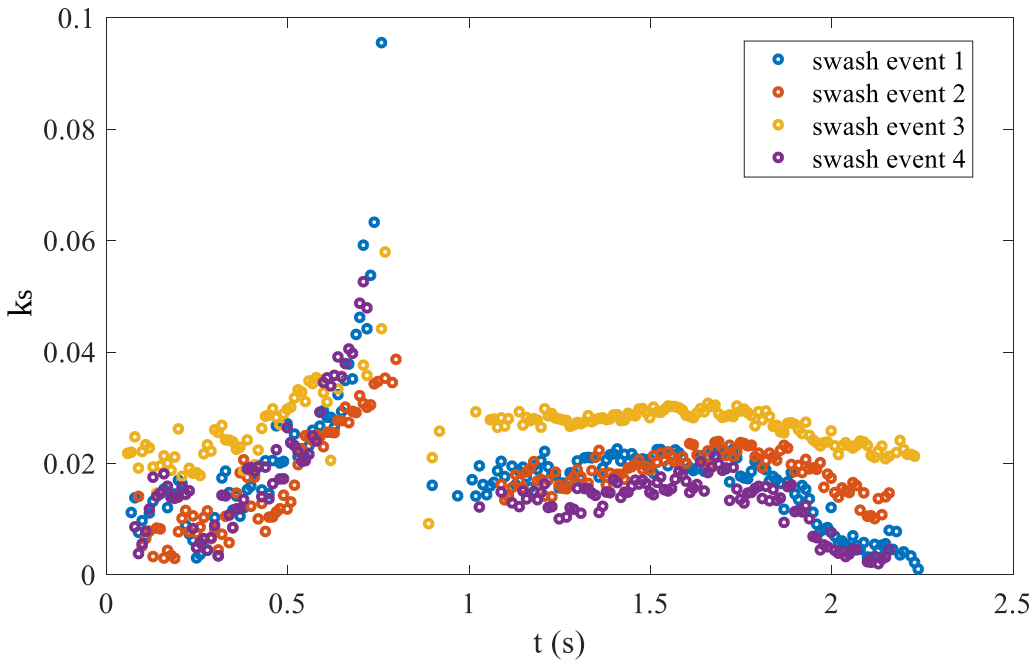

Figure 5-3. Time series of equivalent roughness of 4 swash events

5.2.3 Friction coefficient

Fig. 5-4 shows the time series of friction coefficient estimated from the logarithmic model. It should be noted that instantaneous depth-averaged velocity is used in Eq. 2-4 to evaluate the friction coefficient since the free stream velocity is difficult to be determined. Therefore, the estimated friction coefficient is slightly larger than its true value. Fig. 5-5 shows the friction coefficient estimated from velocity history at different elevations of one swash event. It is found that variation of the friction coefficient is not significant, thus it is assumed that using depth-averaged velocity is appropriate and the following analysis will be based on the friction coefficient estimated from the depth-averaged velocity. It is interesting to find that the friction coefficient is larger during the initial and late period of the uprush and backwash (both) phases. The magnitude of the friction coefficient in the initial and late period of the two phases is over 0.1. For the other phases, it is relatively stable with the magnitude (around 0.03) in the uprush is slightly larger than that in the backwash (around 0.02).

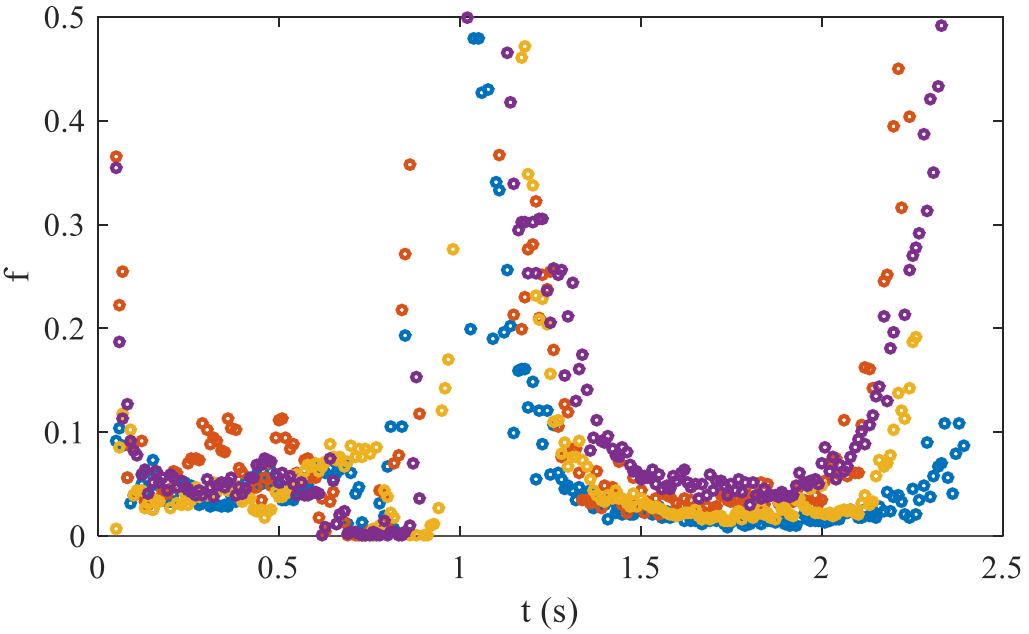

Figure 5-4. Time series of friction coefficient of 4 swash events

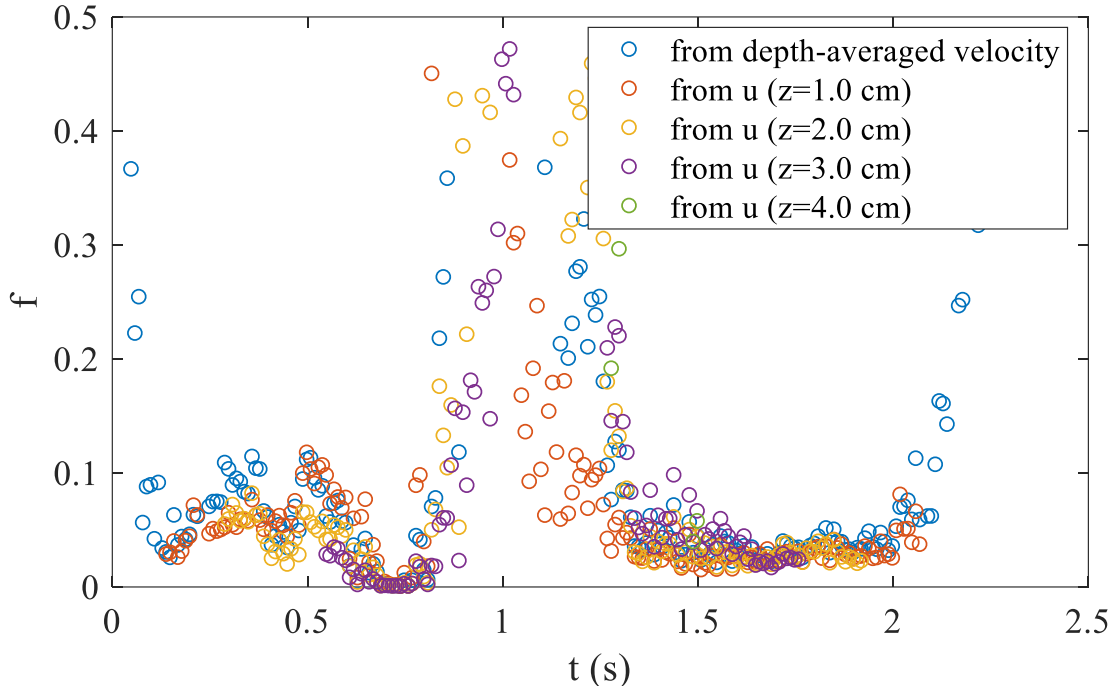

Figure 5-5. Time series of friction coefficient estimated from velocity at different elevations of 4 swash events

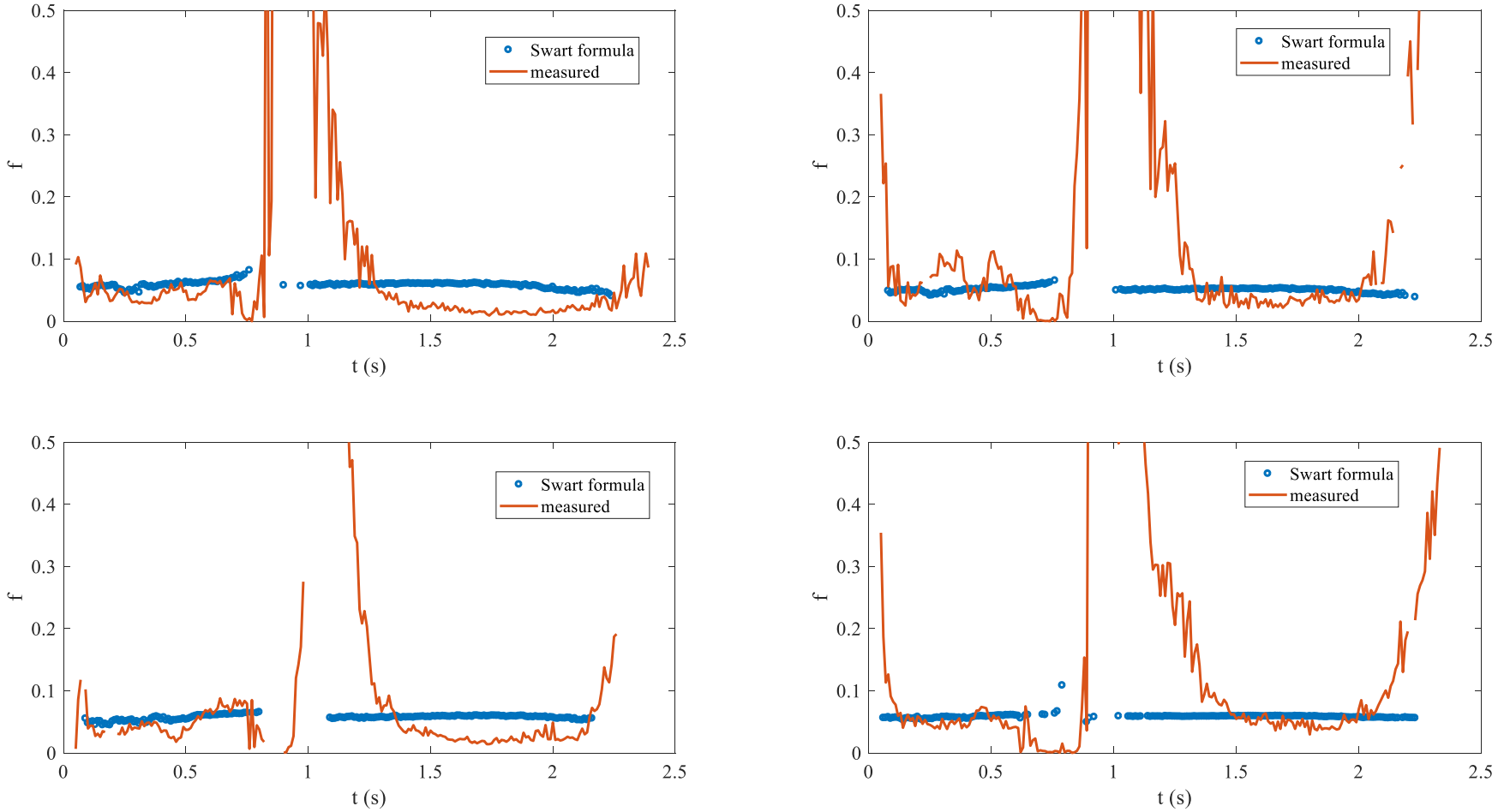

Figure 5-6. Comparison between the measured friction coefficient and Swart formula of 4 swash events

In the absence of velocity profile, the bed shear stress is estimated by Eq. 5-3 based on an empirical friction coefficient. Here, the estimated friction coefficient is compared to the commonly used Swart formula (Swart, 1974) for determining the friction coefficient. It writes as,

$$f = 0.025\exp\left[5.213\left(\frac{a}{k_s}\right)^{-0.194}\right] \tag{5-5}$$

where a is the amplitude of the oscillatory flow water particle displacement, following O'Donoghue et al. (2016), a is estimated from,

$$a = \frac{T}{\sqrt{2\pi}} u_{sd} \tag{5-6}$$

where u_{sd} is the standard deviation of the depth-averaged velocity. By substituting Eq. 5-6 and the equivalent roughness history into Eq. 5-5, intra-swash friction coefficient is deduced (Fig. 5-6). Generally, the friction coefficient estimated by the Swart formula can fit the measured value moderately. During the uprush, the measured friction coefficient is of similar magnitude with the Swart formula while the Swart formula is greater than the measured value in the backwash. Significant difference occurs in the flow reversal and late backwash which is supposed due to the limitation of the Swart formula in the swash zone. Since the Swart formula is established over multiple flow circles and much deeper flow depth, the condition of swash zone cannot meet. The swash flow only has single circle and the water depth is very shallow especially in the initial uprush and late backwash. And in the flow reversal, it is considered that the less developed boundary layer leads to the failure of the Swart formula. It should be noted that the measured friction coefficient is not ground truth since it is estimated from the logarithmic model and the unsteady, non-uniform nature of the swash flow make the logarithmic model questionable as well. Here, the variable equivalent roughness is used to calculate the friction coefficient. A constant value of 0.02 is tried in Eq. 5-5 and gives an invariant friction coefficient ranging between 0.04 and 0.06 of the 4 swash events. It

is concluded that the Swart formula might be appropriate for estimating friction coefficient for most of the swash period for engineering application except of the flow reversal and late backwash where the formula is not suitable.

5.3 Bagnold's model

Bagnold (1963; 1966a) presented both bed load and suspended load transport models for steady flow. Bagnold's energetics type models are based on the assumption that a part of the fluid power (ω) is able to deliver to the sediment particles and initiate their mobilization. The Bagnold bed load and suspended load models are described as,

$$I_b = \frac{k_b \omega}{tan\varphi - tan\beta} \tag{5-7}$$

$$I_s = \frac{0.5(1 - k_s)\omega}{W/u_s - (|u|/u)tan\beta} \tag{5-8}$$

where, I_b and I_s are immersed weight of bed load and suspended load, respectively. k_b and k_s are bed load and suspended load coefficient (kg/N), respectively. φ is the internal friction angle of the sediments ($\tan\varphi = 0.63$), β is the bed slope, W is the sediment fall velocity calculated by (Soulby, 1997),

$$W = \frac{\mu}{\rho d_{50}}(\sqrt{1.049 d_*^3 + 107.3} - 10.36) \tag{5-9}$$

$$d_* = d_{50}\left[\frac{\rho^2 g(s-1)}{\mu^2}\right]^{1/3} \tag{5-10}$$

where, $\mu = 10^{-3}$ Ns/m is the dynamic viscosity of the fluid. u_s is the horizontal velocity of the sediments. The fluid power is often related to the product of free stream velocity and bed shear stress ($\omega = u\tau$).

Many past studies have evaluated the capability of the Bagnold's energetics models by using field measurements in the swash zone. Bed shear stress is often described in the form $\tau = \frac{1}{2}\rho f u|u|$ and an empirical constant f is usually adopted in the past studies for calibrating the Bagnold's energetics approach. Thus, the Bagnold's energetics models are simplified as $I_b = k_b u^3$ and $I_s = k_s u^4$ if the sediment velocity is assumed to be equal to the fluid velocity. These type of Bagnold's energetics models have been calibrated either in the inter-swash time scale over individual wave circles or half circles usually by use of sediment traps (Hardisty et al., 1984; Hughes et al., 1997; Masselink and Hughes, 1998; Masselink et al., 2009) or in intra-swash time scale relying on the collaborated measurements of sediment concentration and transport velocity (Puleo et al, 2000). The calibration of Bagnold's energetics models shows varying degrees of success. A common finding is that the coefficient of uprush is greater than that of backwash, suggesting that uprush is more powerful to transport sediments (Butt et al., 2005).

In order to evaluate the capability of the Bagnold's energetics model, the modeled value of the immersed weight of sediment transport load is compared to the measured depth-averaged sediment transport load of different transport modes. The fluid power is estimated by $\omega = \bar{u}\tau$, where $\bar{u}$ is the depth averaged bed-parallel velocity since it is difficult of determine the free stream velocity. The absolute value of bed shear stress is used in the equation to insure the transport direction. Fig. 5-7 shows the scatter plots of the modeled value (I_b/k_b, $I_s/(1-k_s)$) and measured total depth-averaged sediment transport load. If the Bagnold's model is applicable in the swash zone, linear relationship should be existed between the measured and modeled transport load. It is found that the bed load and suspended load models exhibit similar tendency. Linear relationships exist both for the uprush and backwash phases except for the very initial and late swash period. The coefficient k_b ranges between 10.0 kg/N to 20.0 kg/N and k_s is approximately 1 kg/N which is consistent with the previous studies that the uprush is much more powerful to transport sediments. The Bagnold's model overestimates the sediment transport load in the initial uprush. One probable reason is that there is a 'phase lag' between the driving force and the sediment transport. In other words, it takes some time for the local sand bed to respond to the driving force. Therefore, when the

large driving force firstly occurs along with the bore arriving, sediment transport cannot answer simultaneously leading to the overestimation of the model. In the late backwash, the Bagnold's model underestimates the sediment transport load which is supposed due to sand re-suspension. So it is suggested that the 'phase lag' and re-suspension effect need to be considered into the Bagnold's model or other energetics type models.

The instantaneous sediment transport load is separated into sheet load/suspended load and near bottom load/ upper layer load in the previous chapter. Here, the separated instantaneous transport load is used to evaluate the Bagnold's model. Fig. 5-8 and 5-9 show the comparison between the modeled sediment transport load and the separated sediment transport loads. It is found that the comparison is similar for the near bottom load and suspended load since they dominate in the instantaneous sediment transport for each separation way while the coefficient estimated from the boundary layer load is slightly larger than that from the suspended load. Moreover, there is no clear relationship could be deduced from the comparison between the sheet load transport and Bagnold's bed load model as well as the upper layer load transport and Bagnold's suspended load model. Therefore, it is likely not necessary to divide the sediment transport load into two transport modes when using Bagnold's energetics model in the swash zone. On one hand, it will significantly improve the complexity of the prediction. On the other hand, the Bagnold's model is simple equations far from accuracy since many important parameters are not included in the model, so separating the instantaneous sediment transport is not very meaningful for this kind of rough model.

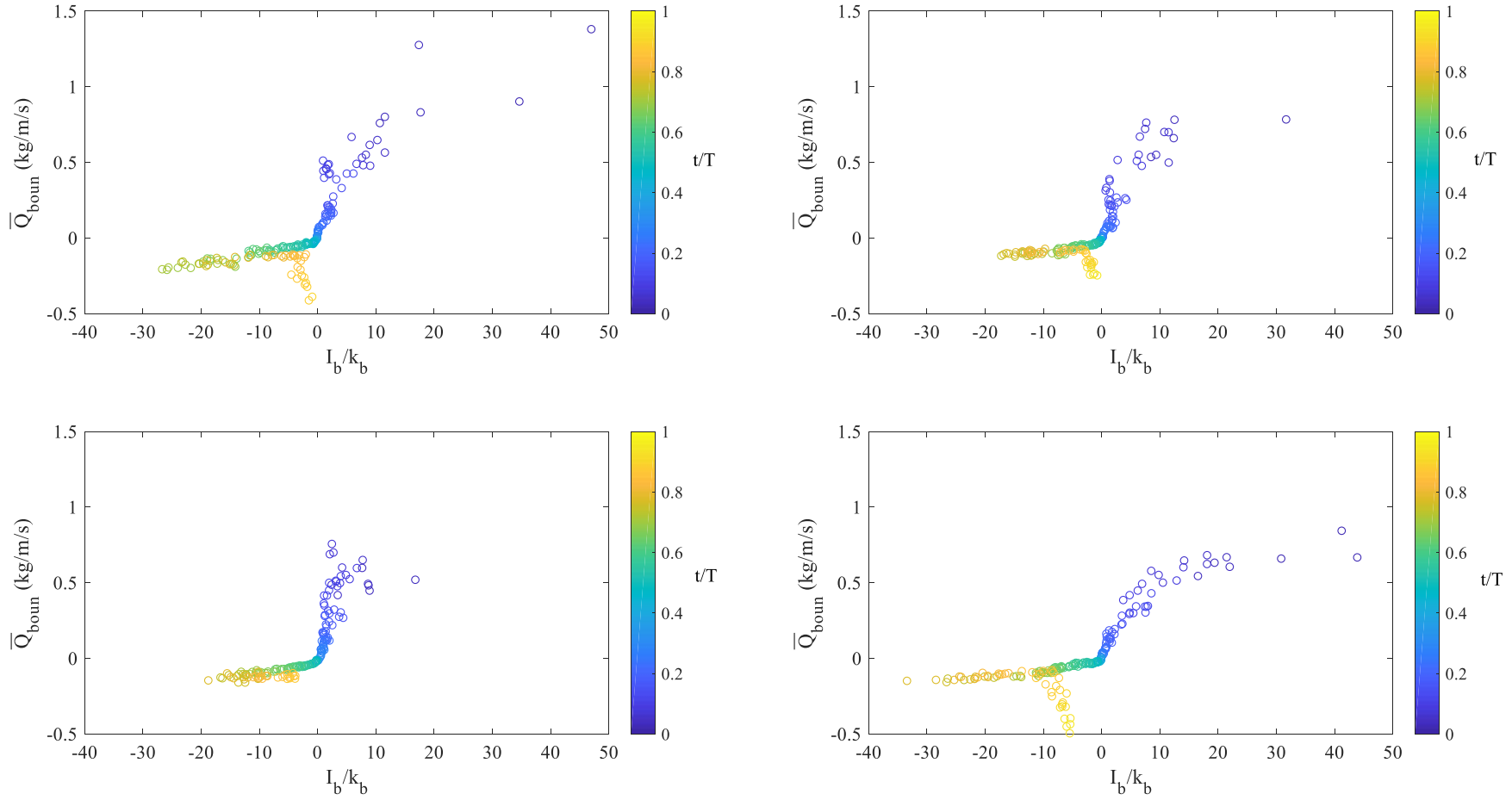

Figure 5-7. Comparison between the Bagnold's bed load model and the measured depth-averaged sediment transport load of 4 swash events

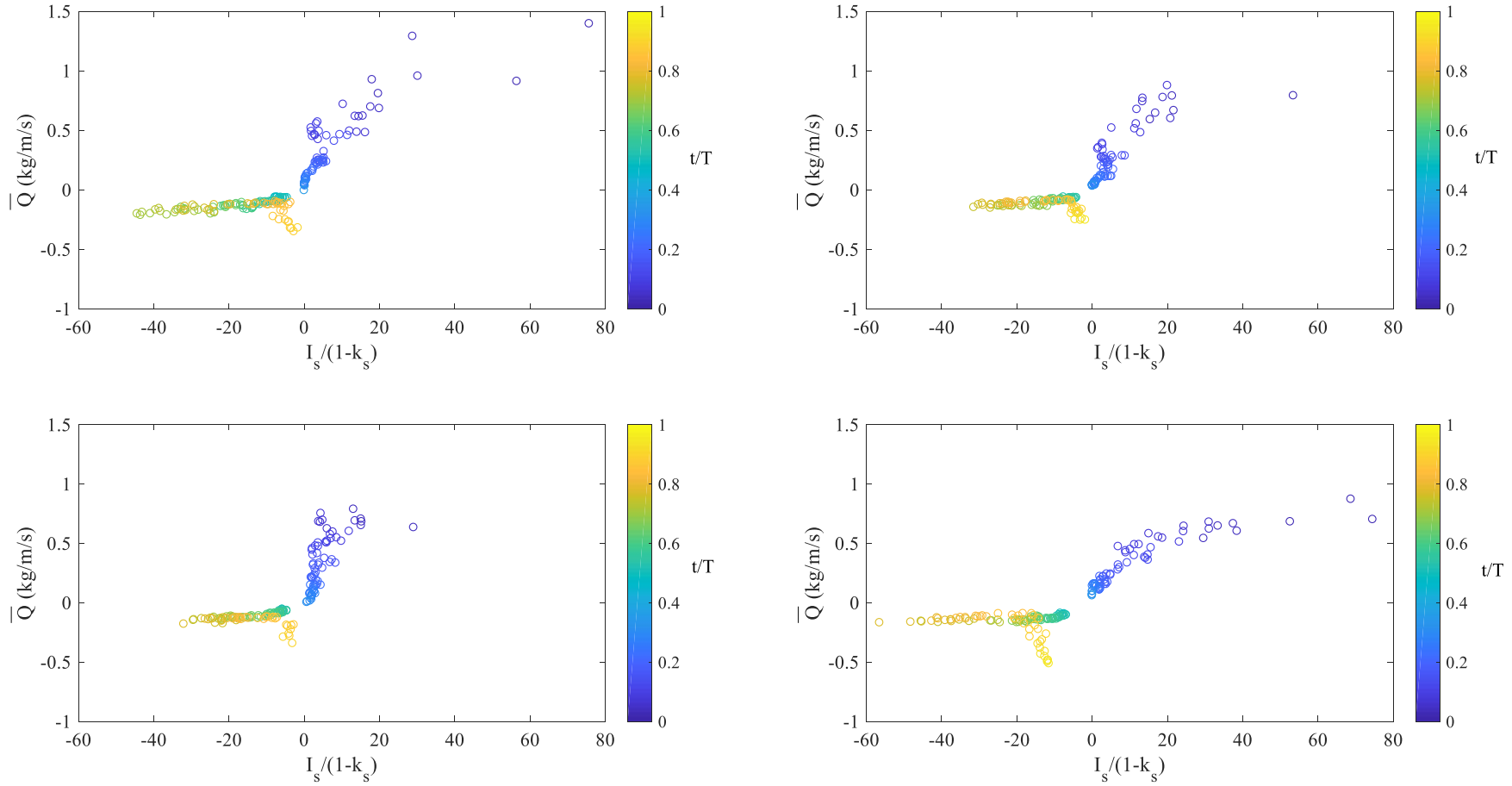

Figure 5-7 (continued). Comparison between the Bagnold's suspended load model and the measured depth-averaged sediment transport load of 4 swash events

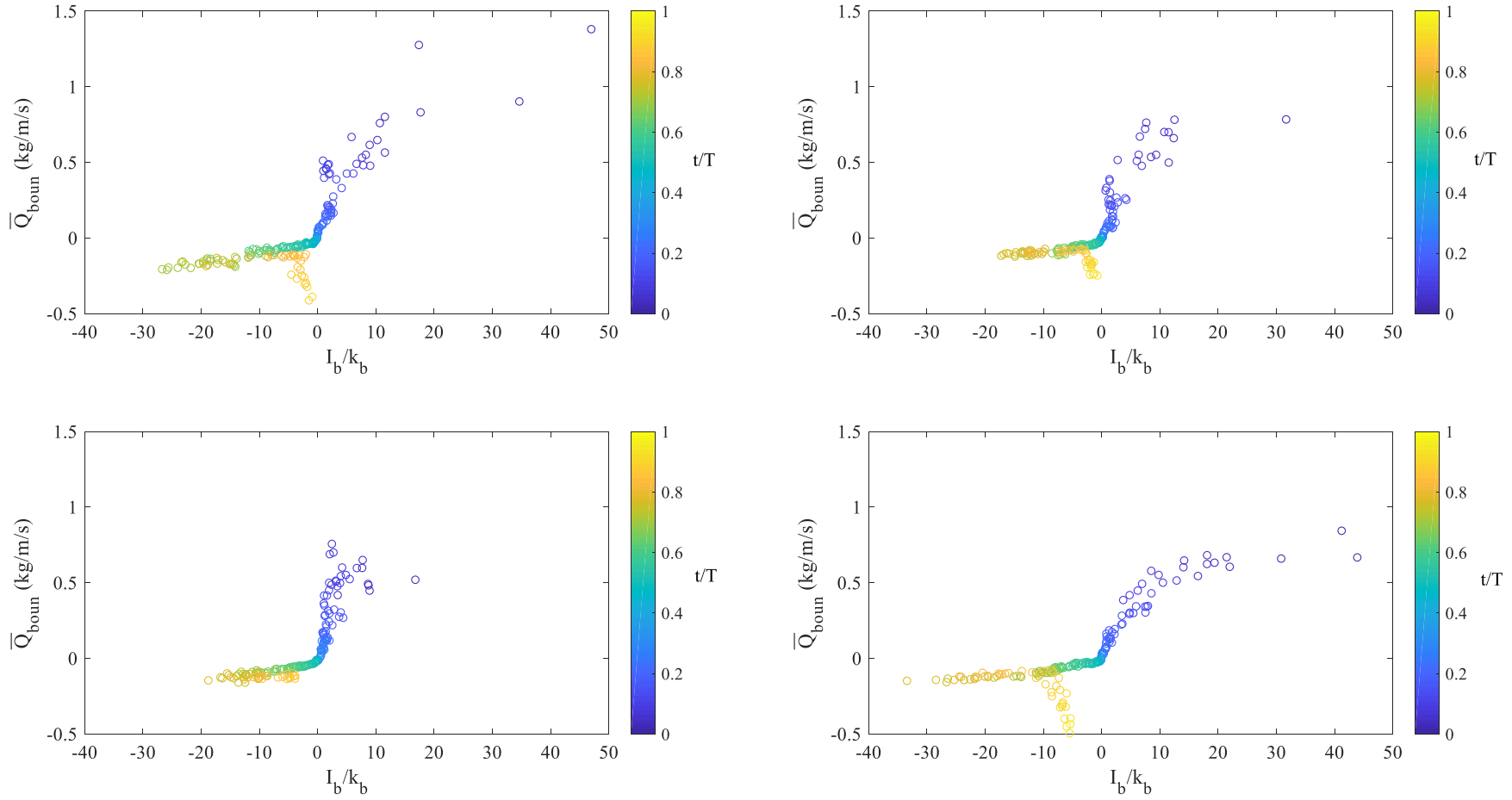

Figure 5-8. Comparison between the Bagnold's bed load model and the measured near bottom transport load of 4 swash events

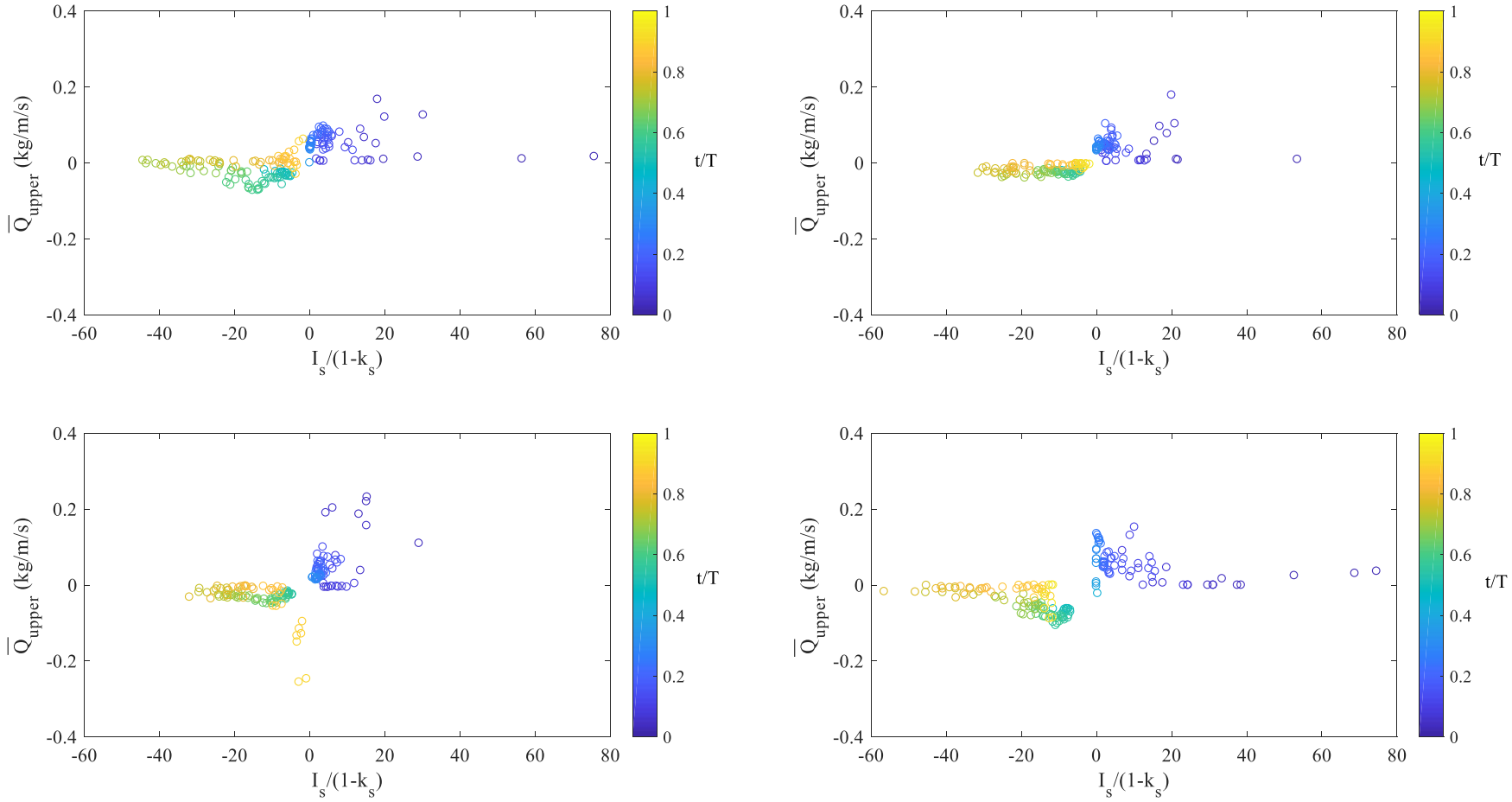

Figure 5-8 (continued). Comparison between the Bagnold's suspended load model and the measured upper layer transport load of 4 swash events

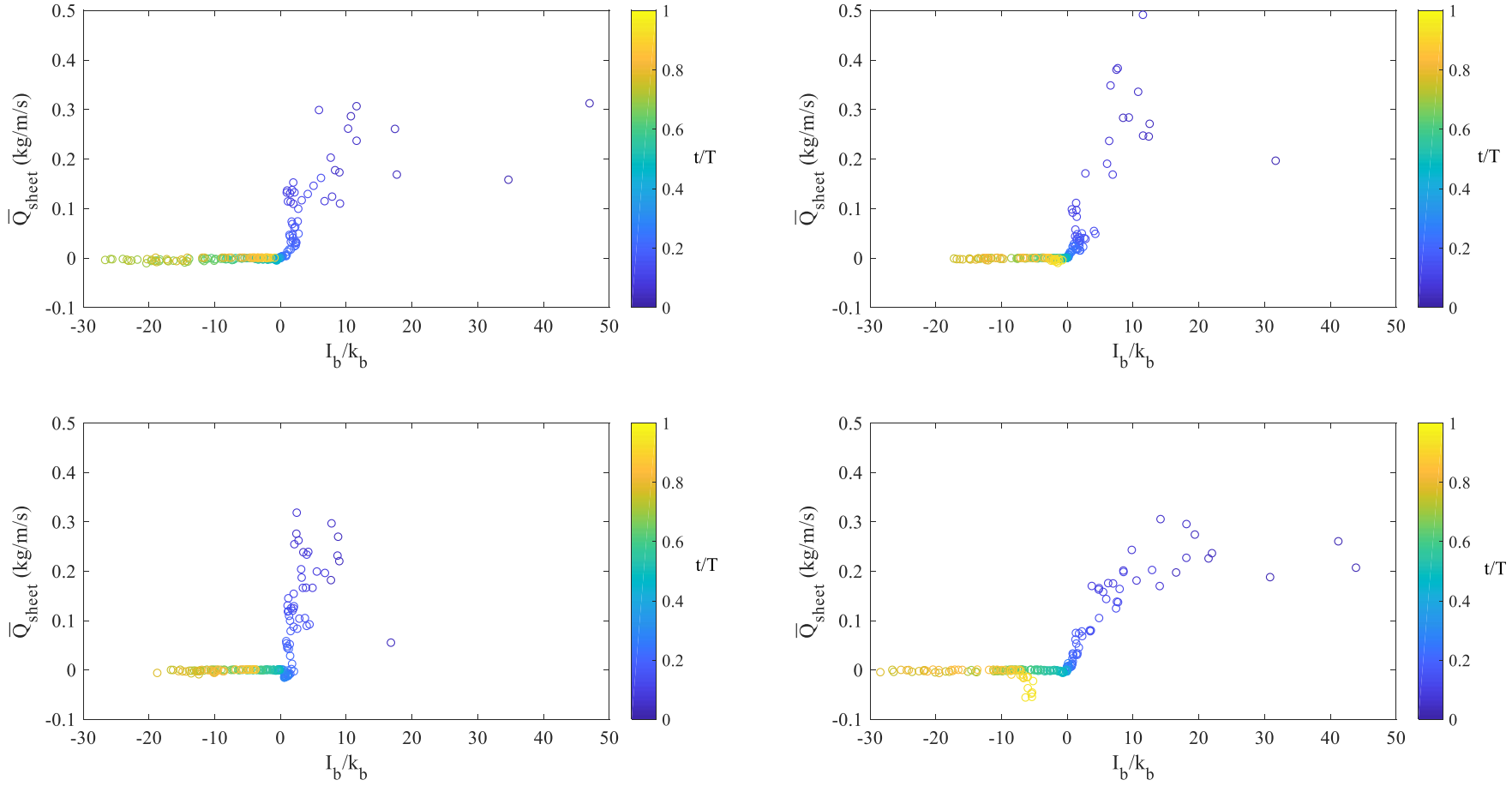

Figure 5-9. Comparison between the Bagnold's bed load model and the sheet load transport of 4 swash events

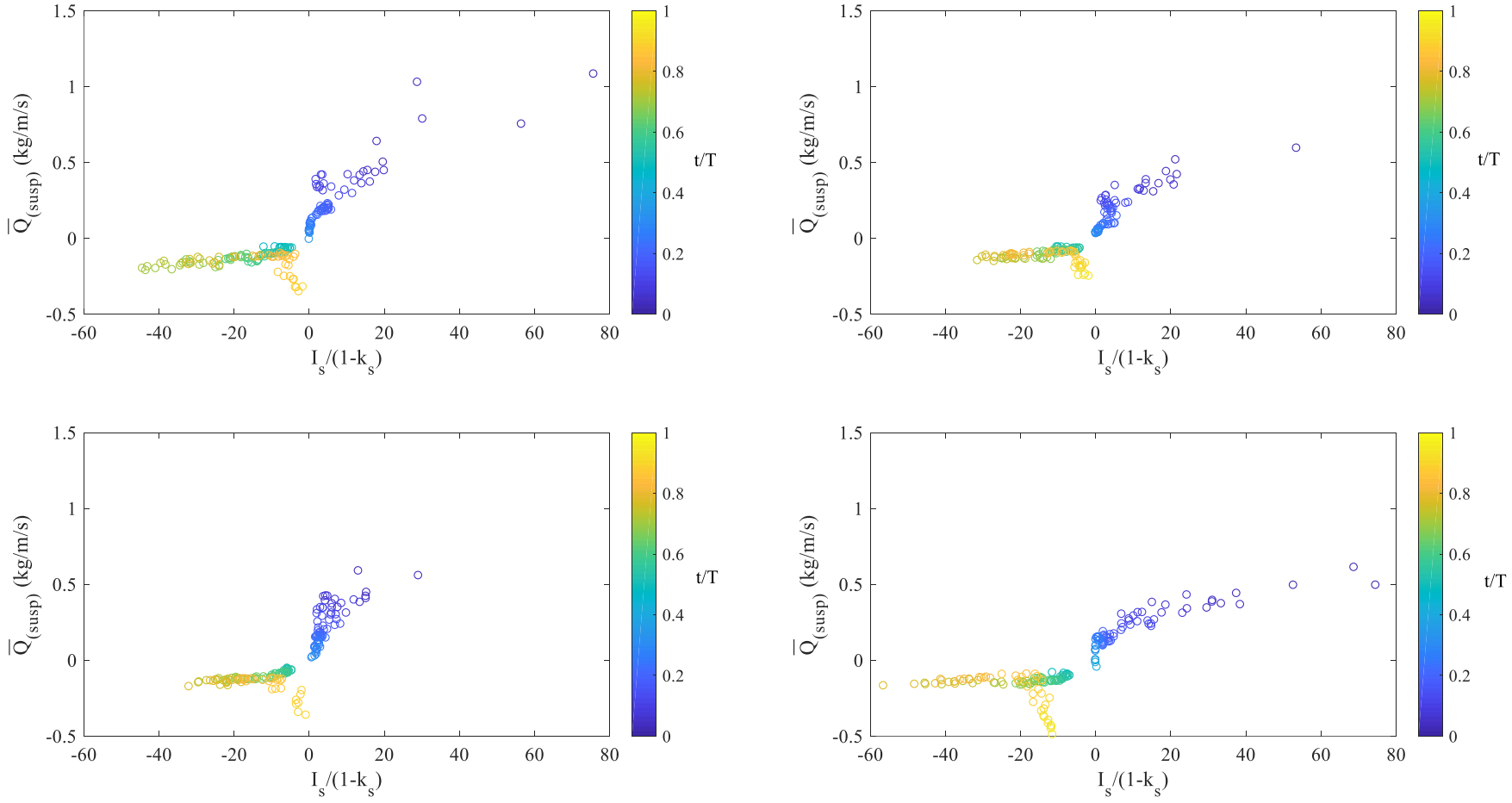

Figure 5-9 (continued). Comparison between the Bagnold's suspended load model and the measured suspended transport load of 4 swash events

5.4 Meyer-Peter and Müller' model

Meyer-Peter and Müller (1948) suggested the non-dimensional sediment transport rate Φ has a relationship with the Shields parameter as following,

$$\Phi = k_c(\theta - \theta_{cr})\sqrt{\theta} \tag{5-11}$$

where Φ is defined as,

$$\Phi = \frac{Q}{\sqrt{(s-1)g{d_{50}}^3}} \tag{5-12}$$

k_c is an empirical coefficient. For steady flow, k_c = 8 is often used. Nielsen (1992) indicates that k_c= 12 is more accuracy for fine sand at high flow intensities. θ_{cr} is the critical Shields stress parameter below which no sediment transport occurs. Here, the bed slope effect is included in the estimation of θ_{cr} to account for the threshold of motion for sand particles on a slope, where particles on a downward slope is more easily dislodged and vice versa. It is derived from ta force balance in air via the Colomb law as introduced by Fredsoe and Deigaard (1992),

$$\theta_{cr} = \theta_{cr\beta=0}(1 \pm \frac{\tan\beta}{\tan\alpha})\cos\beta \tag{5-13}$$

where $\tan\beta$ and $\tan\alpha = 0.63$ are the bed slope and angle of repose of sediment, respectively. $\theta_{cr\beta=0}$ is the critical Shields value on a horizontal bed and it is estimated from the Shileds diagram following Van Rijn (1993),

$$\theta_{cr\beta=0} = \begin{cases} 0.14{d_*}^{-0.64}, & 4 < d_* \leq 10 \\ 0.04{d_*}^{-0.1}, & 10 < d_* \leq 20 \\ 0.013{d_*}^{0.29}, & 20 < d_* \leq 150 \end{cases} \tag{5-14}$$

In this study, $\theta_{cr\beta=0}$ = 0.057 and θ_{cr} is 0.071 and 0.042 for uprush and backwash, respectively.

Fig. 5-10 shows the time series of modeled and measured intra-swash sediment transport load of 4 swash events. The model overpredicts the sediment transport load in the very initial uprush due to the sand bed needs a response time to answer the large driving force when the bore first reaching the sand bed as explained in the previous section. After that, the model underestimates the instantaneous sediment transport load significantly in the left uprush phases. O'Donoghue et al. (2016) indicate that the Meyer-Peter and Müller's model works well in the uprush than the backwash in their laboratory experiment. The main difference is that sand particles in their experiment are much coarser (d_{50} = 1.3 mm and 8.4 mm) than that used in the present study. In that case, sediment flux is more locally generated. However, sediment advection is the main source of the sediment load in the present study. Since the advection is not incorporated in the Meyer-Peter and Müller's model, sediment transport would be underpredicted for the fine sand case. The Meyer-Peter and Müller's model can generally predict the backwash sediment transport load well while the modeled value lags the measured value slightly which is considered due to the pre-suspended sand in the water column since sand particles sink slowly and a large amount of sand is not deposited onto the bed during the flow reversal. Thus, the sediment transport load is underestimated in the early backwash leading to a phase lag.

Fig. 5-11 shows the comparison by plotting the modeled instantaneous sediment transport load against the measured value. Agreement in the initial uprush is quite poor and for the other phases, the discrepancy is within factor order 3. Othman et al. (2014) report coefficient in the range 22-42 when they apply the Meyer-Peter and Müller's model to their measurement of total sediment load overwashing a truncated slope, with bed shear stress estimated by various methods. O'Donoghue et al. (2016) report that the coefficient k_c = 12 gives good estimates of the uprush sediment load for their experiment. Here, it is found that the coefficient ranging between 50 and 100 may give good result for uprush instantaneous sediment transport load and k_c = 12 is reasonable for backwash. Othman et al. (2014) also indicate that the value of optimum transport

coefficient is larger for fine grains. The main difference is that the bed shear stress is estimated from the logarithmic model by the high-resolution velocity profiles in this study and is from empirical formula in the aforementioned two studies. Moreover, Othman et al. (2014) compared the total transport load to the Meyer-Peter and Müller's model instead of intra-swash sediment transport. Besides, the grain size used in the experiment may also influence the optimal coefficient. The effect of grain size could be investigated by conducting experiment with various grain sizes under same conditions in future studies. O'Donoghue et al. (2016) find that the calculated backwash sediment transport load over-estimates the volume observed in the experiment for gravel beach. It is supposed that the critical Shields parameter is necessary to be modified corresponding to the grain size. More importantly, sediment advection must be incorporated into the model when evaluating sediment transport of fine sand by using the Meyer-Peter and Müller's model. Further experiments should be conducted to obtain simultaneous measurement of sediment transport at several adjacent cross-shore locations for quantifying the advection effect.

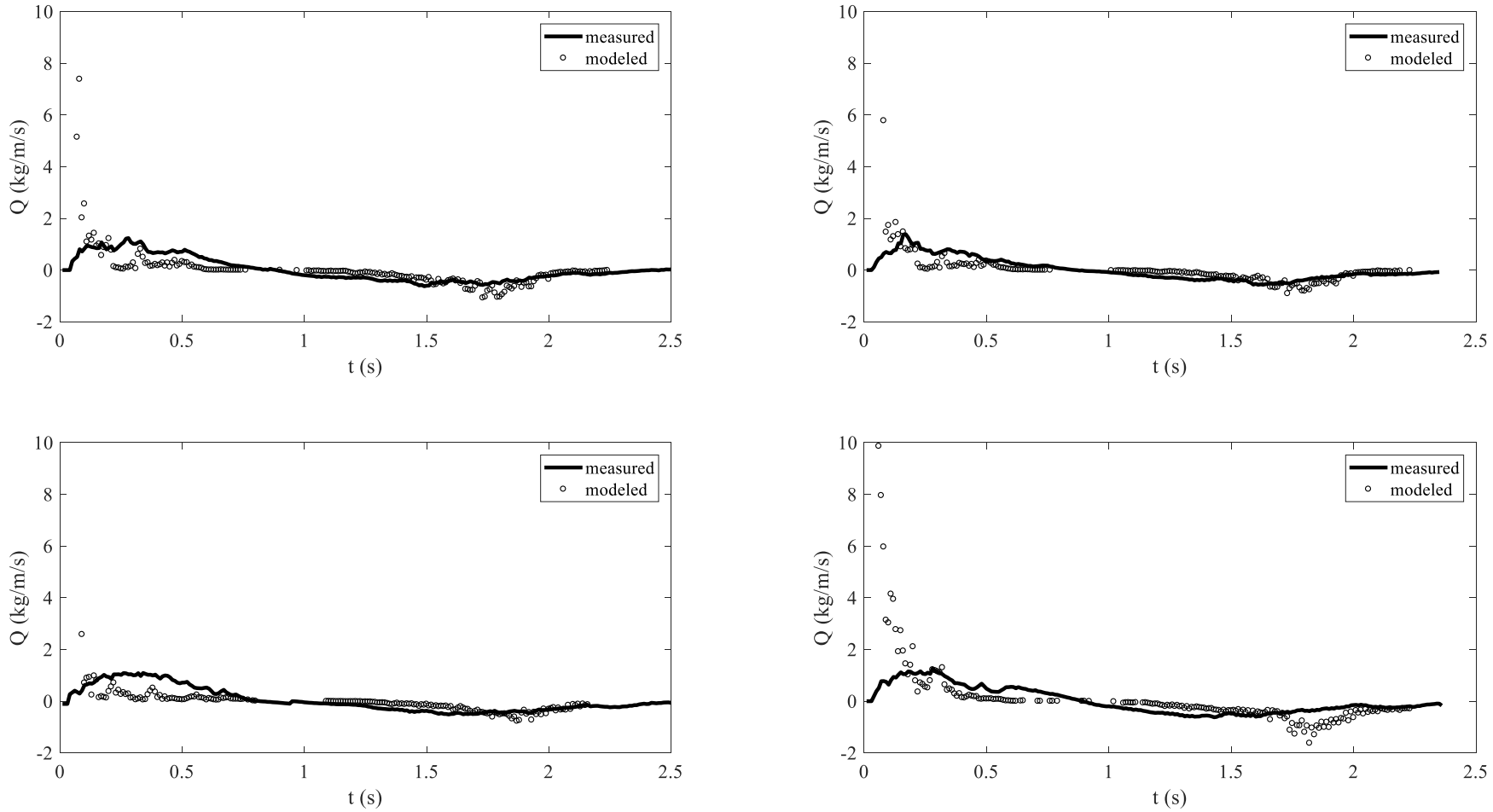

Figure 5-10. Comparison between the Meyer-Peter and Müller's Shields parameter model and the measured sediment transport of 4 swash events

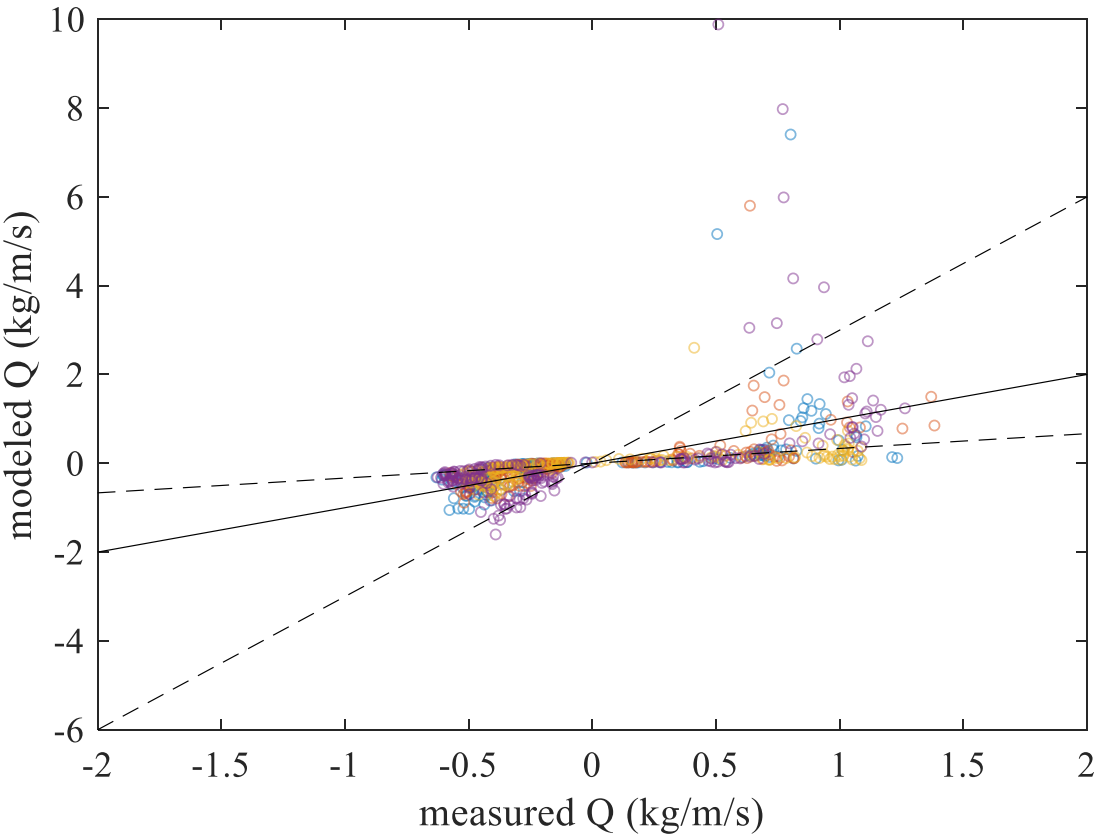

Figure 5-11. Modeled sediment transport plotted against the measured sediment transport; solid line is line of perfect agreement and dashed line indicates factor 3 difference

Chapter 6 Conclusions and recommendations

6.1 Conclusions

The active swash zone is arguably the most dynamic part of the nearshore region separating the land and ocean. The word ‘challenging’ could be found in almost every research paper in terms of the swash zone. The main objective of this study is to improve our understanding of the swash zone and it is partially fulfilled from the following three parts. First, a sediment flux measurement system based on image analysis is developed, which is capable of simultaneously measuring sediment concentration and transport velocity with high temporal and spatial resolution leading to a complete clear ‘picture’ of sediment flux distribution. Secondly, the developed sediment flux measurement system is employed in a laboratory experiment which is carried out over a mobile sand beach under dam-break flow for investigating the hydro- and sediment-dynamics in the swash zone. Sediment concentration, velocity, and flux are quantified successfully throughout the whole swash duration with a temporal resolution of 0.01 s and spatial resolution (vertical) of 0.27 mm. It is one of the most complete and high-resolution datasets of sediment transport in the swash zone since the measurement covers the whole water column over the entire swash duration and the characteristics of the swash zone dynamics are analyzed accordingly. Thirdly, the capability of the most widely used empirical formulas (Bagnold’s energetics type model and Meyer-Peter and Müller’ Shields parameter model) which are often used for predicting sediment transport directly and indirectly (used for coupling flow parameters and sediment transport in process-based models) in the swash zone are evaluated. Advantages and limitations of the empirical models are specified in detail. The main conclusions of the present study are as follows.

The sediment flux measurement system is developed on the basis of several image analysis techniques. Sediment movement in the target flow is recorded by a high-speed camera with an Electronic Luminance sheet as a backlight and a stroboscope as a front light source. All of the instruments are synchronized by a digital delay generator and two types (normal and combined illuminated) of images can be obtained by adjusting

the frequency of the instruments. Sediment flux is quantified by simultaneous measurement of sediment concentration and transport velocity at respective locations in the recorded images. Sediment concentration is measured from the normal images according to the Beer-Lambert law. A specially designed PIV algorithm is used to measure the transport velocity. The velocity field is a combination of the velocity result measured from normal images when sediment concentration is moderate and result from combined illuminated images when sediment concentration is large. The developed image analysis based sediment flux measurement system is flexible and accurate. Temporal resolution is depended on the frequency of the instruments and spatial resolution relies on the installation of the instruments and the PIV analysis. Sediment flux in the flow with a wide range of sediment concentration and transport velocity can be quantified. Verification tests show that sediment flux up to 300 g/L can be precisely measured with an error less than 10%. The measurement system is one of (might be the only one so far) the techniques which can be used for quantification of sediment flux in the swash zone with high resolution.

Sediment concentration, velocity, and flux are successfully obtained across the entire water column (from the vicinity of the mobile sand bed to the water surface) and whole swash duration (from initial uprush to late backwash) over a fine sand bed in the swash zone. It is the first time that the sediment dynamics could be completely measured with such a high resolution (temporal resolution of 0.01 s and spatial (vertical) resolution of 0.27 mm) leading to an extremely valuable database for investigating sediment transport in the swash zone.

Sediment concentration reaches a peak soon after the arrival of the dam-break flow with the maximum value occurs around ¼ to ½ of the uprush duration. It decays gradually until the final backwash where sediment re-suspension takes place leading to an increase in the sediment concentration. A sudden decrease in the concentration is observed during the flow reversal. The maximum sediment concentration in the uprush could be twice as large as that in the backwash. Moreover, the difference of the maximum sediment concentration between uprush and backwash is much larger at the lower elevations than that at the higher water column. Sand particles gather in a thin layer (less than 1.0 cm) close to the sand bed. Exceeding this elevation, sediment

concentration drops gradually and restlessly due to sinking. The depth-averaged sediment concentration decays gradually during the uprush to a low value about 50 g/L and this value keeps stable during the flow reversal and former half of the backwash indicating that sediment pick-up and deposition achieve a balance. In the final backwash, the depth-averaged sediment concentration rises rapidly due to sediment re-suspension and this process could reshape the sand bed profile significantly. The vertical distribution of time-averaged sediment concentration can generally fulfill Rouse's profile. Two reference concentrations are used to test the Rouse's formula and it is found that the using reference concentration at z = $100d_{50}$ is slightly better than that using z = 0.05h. The Rouse number is found to be ranging between 0.43 and 0.62 and it might be able to be used as an indicator for swash zone sediment transport modeling.

Sand particles follow the dam-break swash flow over the sloping beach very well. The magnitude of maximum uprush velocity is much larger than that of backwash due to energy dissipation. It is found that the uprush duration is approximately 2/3 of the backwash duration. Sand particles near the bed reverse earlier than those in the upper layers. Reversal time is around 0.7 s at z = 0.5 cm and 1.1s at z = 2.5 cm. The difference in the reversal time could be 1/6 of the total swash duration within this thin water column. The maximum backwash bed-parallel velocity appears in the late backwash instead of at the end of the swash event with the magnitude around ¾ of the maximum uprush velocity. Vertical gradient of the bed-parallel velocity is very large throughout the whole water column in the entire uprush period thus the velocity profiles are completely non-depth uniform. In the backwash, the velocity gradient is only significant in the lower water column and the velocity tends to be uniform in the upper layers. The instantaneous boundary layer can extend to the local water depth in the initial uprush and stays for about 1/10T. It decays gradually and turns to be almost zero during flow reversal. The instantaneous boundary layer depth grows progressively after the flow reversal and is constricted by the water depth again in the late backwash (keeps approximately 1/5T). The maximum boundary layer depths of both uprush and backwash are of similar magnitude, being 2/5 of the maximum water depth. It is suggested that the boundary layer develops rapidly and can extend to a large part of the water column in the very foreshore region even though the flow duration is very short.

Time series of the instantaneous sediment flux generally shows a decreasing-increasing tendency except for that very close to the sand bed where sediment flux grows again in the final backwash due to re-suspension. The instantaneous sediment flux grows rapidly from the sand bed, reaching a peak in the lower water column and then decays mildly to the water surface. The maximum sediment flux for both uprush and backwash occurs between 0.05*h* and 0.10*h*. Sediment flux above the boundary layer is weaker than that of the boundary layer by one order of magnitude.

The magnitude of maximum uprush instantaneous sediment transport load (1.2 kg/m/s) could be twice as large as the backwash value (-0.6 kg/m/s). It is found that the instantaneous sheet layer thickness is approximately 1/3 of the bottom boundary layer thickness during the uprush in this study. The maximum sheet layer thickness is about 1/10*h*, occurring in the middle uprush. Sheet load transport almost vanishes after the flow reversal. The maximum instantaneous sheet load transport takes place in the middle uprush with a magnitude around 0.5 kg/m/s and it is much smaller than the maximum instantaneous suspended load transport (0.7 kg/m/s). The maximum instantaneous near bottom sediment transport load could be similar with the total instantaneous load while the maximum instantaneous upper layer transport load is only around 0.3 kg/m/s. The instantaneous cumulative sediment transport load grows rapidly and reaches its peak (around 50 kg/m/s) before flow reversal. When the flow starts to go offshore, the total cumulative sediment transport load decays mildly and it ends at a slightly positively value (O < 10 kg/m/s). Since the sheet load transport mainly occurs in the uprush, it contributes to a positive (onshore) sediment movement with a magnitude of approximately 10 kg/m/s. The suspended load transport generally has a similar tendency with the total sediment transport while it makes a negative (offshore) contribution about -10 kg/m/s. The maximum cumulative near bottom sediment transport load is very close to that of the suspended load transport (30~40 kg/m/s) and the onshore near bottom sediment transport is greater than the offshore component. The upper layer load transport is relatively much weaker. The maximum upper layer load transport is around 10 kg/m/s and the net value is close to zero. In this study, time-integrated net sediment transport load is offshore in the vicinity of the bed, onshore in the middle of the flow region and almost zero in the upper layers. The net sediment

transport of each load is a small sum of two large opposite components and the magnitude difference between the one-way load and net sediment transport could be as large as one order. The magnitude of net sediment transport load at each elevation is approximately half of the one-way sediment transport load. The net sediment transport estimated by the measurement system is smaller than that evaluated by the bed level change by at most 20%. This mismatch appears to be related to both the error in bed level change and sediment flux.

Most of the velocity profiles are well described by the logarithmic model. Bed shear stress, friction coefficient, and equivalent roughness are derived from the logarithmic model successfully. The maximum bed shear stress occurs in the initial uprush accompanied by the bore arrival and then the bed shear stress decays gradually until the flow reversal. During the backwash, the bed shear stress firstly grows gently, reaching a peak in the middle backwash and decreases after that till the end of the swash run. The equivalent roughness varies over the swash cycle ranging from $100d_{50}$ to $150d_{50}$. The friction coefficient is larger during the initial and late period of the uprush and backwash (both) phases. The magnitude of the friction coefficient in the initial and late period of the two phases is over 0.1. For the other phases, it is relatively stable with the magnitude around 0.03 in the uprush slightly larger than that in the backwash (around 0.02). By comparing the measured friction coefficient to the Swart formula, it is concluded that the Swart formula might be appropriate for estimating friction coefficient for most of the swash period for engineering application except the flow reversal and late backwash where the formula is not suitable.

By comparing the measurements to the Bagnold's energetics type model, it is found that The Bagnold's model overestimates the sediment transport load in the initial uprush due to phase lag effect. In the late backwash, the Bagnold's model underestimates the sediment transport load which is supposed due to sand re-suspension. So it is suggested that the 'phase lag' and re-suspension effect need to be considered into the Bagnold's model or other energetics type models. The Bagnold's model thus could be only used for roughly predicting sediment transport in the swash zone. The coefficient k_b ranges between 10.0 kg/N to 20.0 kg/N and k_s is approximately 1 kg/N which means the uprush is much more powerful to transport sediments. The instantaneous sediment transport

load is separated into sheet load/suspended load and near bottom load/ upper layer load for comparing with the Bagnold's model, and it is found that the model capability is not improved.

For the Meyer-Peter and Müller' model, it overpredicts the sediment transport load in the very initial uprush and underestimates significantly in the left uprush period. The Meyer-Peter and Müller's model can generally predict the backwash sediment transport load well while the modeled value lags the measured value slightly which is considered due to the pre-suspended sand in the water column. Agreement between the model and measurements in the initial uprush is quite poor and for the other phases, the discrepancy is within factor order 3. It is supposed that the critical Shields parameter is necessary to be modified corresponding to the grain size. More importantly, sediment advection must be incorporated into the model when evaluating sediment transport of fine sand.

6.2 Recommendations

The developed sediment flux measurement system has shown promising capability in investigating sediment transport in the swash zone. An extremely valuable dataset was generated through the laboratory experiment. However, the measurement was only carried out on one single condition (flow condition, slope angle and sand type) and one cross-shore location. Therefore, the dataset is unique but limited and some experimental results of the present study are strongly location depended rather than universal truth for the swash zone. Experimental conditions are expected to be expanded in order to generate a more detailed and complete dataset of swash zone sediment transport. In that case, hydro- and sediment-dynamics of the swash zone can be investigated more comprehensively.

Wave/bore breaking on the sand bed plays a critical role in the swash zone sediment transport. Image technology seems the only way can accurately quantify the sediment flux due to breaking. With the developed sediment flux measurement system, setting a much higher fps might be helpful for analyzing the breaking process and the resulted sediment entrainment since this process is pretty short. If the turbulence and resulted sediment entrainment due to wave/bore breaking is explicit, empirical sediment

transport formulas can be improved significantly. Moreover, setting a higher fps is also useful for measuring the bed-normal velocity and therefore the diffusion process.

In the present laboratory experiment, intra-swash bed level change is very small. Therefore, is it difficult to derive the pick-up rate through conservation law,

$$E = D - (1 - \lambda)\frac{\partial z_b}{\partial \mathrm{t}} \tag{6-1}$$

where, E is the pick-up rate, *D* is the deposition rate which can be evaluated by the product of settling velocity and near-bed sediment concentration. Further experiments are expected to be conducted under more strong flow condition to generate a large bed level evolution. Thus, pick-up function for the swash zone sediment transport might be deduced. If the diffusion process can also be clear, new process-based sediment transport formula for the swash zone is possible.

One significant drawback of the swash zone study is that most experiments are focusing on 'pure' swash event while the swash-swash interaction is common in the nature swash zone. Driving force due to the interaction makes the sediment transport process more complex; however, research on this theme is necessary and urgent. The measurement system developed in the present dissertation can be used for studying this problem but air bubbles due to interaction might add some unknown difficulties.

It is strongly suggested that experiments should be the priority to investigate the swash zone instead of numerical modeling. On one hand, the reliable dataset is important for validating the numerical models. On the other hand, much most numerical models are using empirical functions which are not developed for swash zone. It is obvious that only the empirical function can be modified to satisfy the swash zone condition, numerical models can give convincible results. Therefore, experimental investigations are the base for improving our knowledge of the swash zone and much more laboratory and field experiments should be conducted.

References

Aagaard, T. and Hughes, M.G., 2006. Sediment suspension and turbulence in the swash zone of dissipative beaches. Marine Geology 228 (1–4), 117–135.

Austin, M.J. and Masselink, G., 2006. Observations of morphological change and sediment transport on a steep gravel beach. Marine Geology 229 (1–2), 59–77.

Bagnold, R.A., 1963. Mechanics of marine sedimentation. The sea, Hill, M. N. (editor), Vol. 3, Wiley Interscience, New York.

Bagnold, R.A., 1966a. An approach to the sediment transport problem from general physics, No. 422-I, US Geological Survey, Washington, DC.

Bagnold, R.A., 1966b. The shearing and dilatation of dry sand and the 'singing' mechanism. Philosophical Transaction of the Royal Society of London. Mathematic Physical Science 295(1442), 219-232.

Bakhtyar, R., Barry, D.A., Li, L., Jeng, D.S., and Yeganeh-Bakhtiary, A., 2009. Modeling sediment transport in the swash zone: a review. Ocean Engineering 36, 767–783.

Barnes, M.P., O'Donoghue, T., Alsina, J.M. and Baldock, T.E., 2009. Direct bed shear stress measurements in bore-driven swash. Coastal Engineering 56, 853-867.

Blenkinsopp, C.E., Turner, I.L., Masselink, G. and Russell, P.E., 2011. Swash zone sediment fluxes: field observations. Coastal Engineering 58 (1), 28–44.

Briganti, R., Torres-Freyermuth, A., Baldock, T.E., Brocchini, M., Dodd, N., Hsu, T., Jiang, Z., Kim, Y., Pintado-Patiño, J.C. and Postacchini, M., 2016. Advances in numerical modelling of swash zone dynamics. Coastal Engineering 115, 26-41.

Butt, T. and Russell, P., 2000. Hydrodynamics and cross-shore sediment transport in the swash-zone of natural beaches: a review. Journal of Coastal Research 16 (2), 255-268.

Butt, T., Russell, P., Puleo, J.A. and Masselink, G., 2005. The application of Bagnold-type sediment transport models in the swash zone. Continental Shelf Research 21, 887–895.

Butt, T., Russell, P.E., Puleo, J.A., Miles, J.R. and Masselink, G., 2004. The influence of bore turbulence on sediment transport in the swash and inner surf zones. Continental Shelf Research 24, 757–771.

Chardón-Maldonado, P., Pintado-Patino, J.C. and Puleo, J.A., 2016. Advances in swash-zone research: small-scale hydrodynamic and sediment transport processes. Coastal Engineering 115, 8-25.

Chen, B., Kikkert, G.A., Pokrajac, D. and Dai, H., 2016. Experimental study of bore-driven swash–swash interactions on an impermeable rough slope. Coastal Engineering 108, 10-24.

Conely, D.C. and Griffin, J.G., 2004. Direct measurements of bed stress under swash in the field. Journal of Geophysical Research 109, C03050.

Cox, D.T., Kobayashi, N., and Okayasu, A., 1996. Bottom shear stress in the surf zone. Journal of Geophysical Research: Oceans 101 (C6), 14337–14348.

Fredsoe, J. and Deigaard, R., 1992. Mechanics of coastal sediment transport. Advanced Series on Ocean Engineering, Vol. 3. Singapore, World Scientific.

Hardisty, J., Collier, J., and Hamilton, D., 1984. A calibration of the Bagnold beach equation. Marine Geology 61, 95–101.

Hirt, C.W., and Nichols, B.D., 1981. Volume of fluid (VOF) method for the dynamics of free boundaries. Journal of Computational Physics 39, 201–225.

Horn, D. P., and Mason, T., 1994. Swash sediment transport modes. Marine Geology 120, 309–325.

Hsu, T.J., Sakakiyama, T. and Liu, P.L.F., 2002. A numerical model for wave motions and turbulence flows in front of a composite breakwater. Coastal Engineering 46, 25–50.

Hu, P., Li, W., He, Z., Phtz, T. and Yue, Z., 2015. Well-balanced and flexible morphological modeling of swash hydrodynamics and sediment transport. Coastal Engineering 96, 27– 37.

Hughes, M.G., 1995, Friction factors for wave uprush, Journal of Coastal Research 11(4), 1089 – 1098.

Hughes, M.G., Masselink, G. and Brander, R.W., 1997. Flow velocity and sediment transport in the swash zone of a steep beach. Marine Geology 138 (1–2), 91–103.

Inch, K., Masselink, G., Puleo, J.A., Russell, P., and Conley, D.C., 2015. Vertical structure of near bed cross-shore flow velocities in the swash zone of a dissipative beach. Continental Shelf Research 101, 98-108.

Jackson, N.L., Masselink, G. and Nordstrom, K.F., 2004. The role of bore collapse and local shear stresses on the spatial distribution of sediment load in the uprush of an intermediate-state beach. Marine Geology 203 (1–2), 109–118.

Karambas, T.V., 2003. Modelling of infiltration–exfiltration effects of cross-shore sediment transport in the swash zone. Coastal Engineering Journal 45, 63–82.

Karambas, T.V., 2006. Prediction of sediment transport in the swash zone by using a nonlinear wave model. Continental Shelf Research 26, 599–609.

Kelly, D.M., Dodd, N., 2010. Beach-face evolution in the swash zone. Journal of Fluid Mechanics 661 (12), 316–340.

Kikkert, G.A., O'Donoghue, T., Pokrajac, D. and Dodd, N., 2012. Experimental study of bore-driven swash hydrodynamics on impermeable rough slopes, Coastal Engineering 60, 149–166.

Kikkert, G.A., Pokrajac, D., O'Donoghue, T. and Steenhauer, K., 2013. Experiment study of bore driven swash hydrodynamics on permeable rough slopes, Coastal Engineering 79, 42–56.

Klostermann, J., Schaake, K., and Schwarze, R., 2013. Numerical simulation of a single rising bubble by vof with surface compression. International Journal for Numerical Methods in Fluids 71, 960– 982.

Kobayashi, N., 1999. Numerical modeling of wave run-up on coastal structures and beaches. Marine Technology Society Journal 33 (3), 33-37.

Li, W., Hu, P., Pähtz, T., He, Z. and Cao, Z., 2017. Limitations of empirical sediment transport formulas for shallow water and their consequences for swash zone modelling. Journal of Hydraulic Research 55 (1), 114-120.

Lin, P., and Liu, P.L.F., 1998. Turbulence transport, vorticity dynamics, and solute mixing under plunging waves in surf zones. Journal of Geophysical Research 103, 15677–15694.

Liu, H., and Sato, S., 2005. Laboratory study on sheetflow sediment movement in the oscillatory turbulent boundary layer based on image analysis. Coastal Engineering Journal 47(1), 21-40.

Long, S., Petti, M. and Losada, I.J., 2002. Turbulence in the swash and surf zones: a review. Coastal Engineering 45, 129-147.

Losada, I.J., Lara, J.L., Guanche, R. and Gonz á lez-Ondina, J.M., 2008. Numerical analysis of wave overtopping of high mound breakwaters. Coastal Engineering 55, 47–62.

Masame, Y., 2013. Image based technique for sediment flux measurement with a light transmission method (In Japanese). Master's thesis, Tokyo University of Marine Science and Technology.

Masselink, G. and Hughes, M., 1998. Field investigation of sediment transport in the swash zone. Continental Shelf Research 18(10), 1179-1199.

Masselink, G. and Puleo, J.A., 2006. Swash-zone morphodynamics. Continental Shelf Research 26, 661–680.

Masselink, G., Evans, D., Hughes, M.G., and Russell, P., 2005. Suspended sediment transport in the swash zone of a dissipative beach. Marine Geology 216 (3), 169–189.

Masselink, G., Russell, P., Turner, I.L. and Blenkinsopp, C., 2009. Net sediment transport and morphological change in the swash zone of a high-energy sandy beach from swash event to tidal cycle time scales. Marine Geology 267, 18–35.

Nielsen, P., 1992. Coastal bottom boundary layer and sediment transport. Advanced Series on Ocean Engineering, Vol. 4. Singapore, World Scientific.

O'Donoghue, T., Kikkert, G.A., Pokrajac, D., Dodd, N. and Briganti, R., 2016. Intra-swash hydrodynamics and sediment flux for dambreak swash on coarse-grained beaches. Coastal Engineering 112, 113–130.

O'Donoghue, T., Pokrajac, D., and Hondebrink, L.J., 2010. Laboratory and numerical study of dambreak-generated swash on impermeable slopes. Coastal Engineering 57 (5), 513–530.

Osborne, P.D., Rooker, G.A., 1999. Sand re-suspension events in a high energy infragravity swash zone. Journal of Coastal Research 15 (1), 74–86.

Othman, I.K., Baldock, T.E. and Callaghan, D.P., 2014. Measurement and modelling of the influence of grain size and pressure gradient on swash uprush sediment transport. Coastal Engineering 83, 1–14.

Pedrozo-Acuna, A., Simmonds, D.J., Chadwick, A.J. and Silva, R., 2007. A numericalempirical approach for evaluating morphodynamic processes on gravel and mixed sand-gravel beaches. Marine Geology 241, 1–18.

Pedrozo-Acuna, A., Simmonds, D.J., Otta, A.K., and Chadwick, A.J., 2006. On the crossshore profile change of gravel beaches. Coastal Engineering 53 (4), 335–347.

Pope, S.B., 2000., Turbulent Flows. University Press, Cambridge, UK, pp. 771.

Puleo, J.A., and Butt, T., 2006. The first international workshop on swash-zone processes. Continental Shelf Research 26, 556-560.

Puleo, J.A., and Torres-Freyermuth, A., 2016. The second international workshop on swash-zone processes. Coastal Engineering 115, 1-7.

Puleo, J.A., 2009. Tidal variability of swash zone sediment suspension and transport. Journal of Coastal Research 25, 937–948.

Puleo, J.A., and Holland, K.T., 2001. Estimating swash zone friction coefficients on a sandy beach, Coastal Engineering 43, 25 – 40.

Puleo, J.A., Beach, R.A., Holman, R.A. and Allen, J.S., 2000. Swash zone sediment suspension and transport and the importance of bore-generated turbulence. Journal of Geophysical Research: Oceans 105(C7), 17021-17044.

Puleo, J.A., Lanckriet, T., Conley, D. and Foster, D., 2016. Sediment transport partitioning in the swash zone of a large-scale laboratory beach. Coastal Engineering 113, 73–87.

Puleo, J.A., Lanckriet, T.M. and Wang, P., 2012. Near bed cross-shore velocity profiles, bed shear stress and friction on the foreshore of a microtidal beach, Coastal Engineering 68(10), 6–16.

Raffel, M., Willert, C., Wereley, S. and Kompenhans, J., 2007. Particle Image Velocimetry-A Practical Guide. Springer-Verlag, Berlin, Heidelberg.

Rakha, K.A., Deigaard, R. and Brøker, I., 1997. A phase-resolving cross shore sediment transport model for beach profile evolution. Coastal Engineering 31, 231–261.

Raubenheimer, B., Elgar, S. and Guza, R.T., 2004. Observations of swash zone velocities: a note on friction coefficients. Journal of Geophysical Research 109, C01027.

Rouse, H., 1937. Modern conceptions of the mechanics or fluid turbulence. Transactions of the American Society of Civil Engineers 102(1), 463-505.

Ruju, A., Conley, D., Masselink, G., and Puleo, J., 2016a. Sediment transport dynamics in the swash zone under large scale laboratory conditions. Continental Shelf Research, 120, 1-13.

Ruju, A., Conley, D., Masselink, G., Austin, M., Puleo, J., Lanckriet, T. and Foster, D., 2016b. Boundary layer dynamics in the swash zone under largescale laboratory conditions. Coastal Engineering 113, 47-61.

Schmidt, W., 1925. Der Massenaustausch in freier Luft und verwandte Erscheinungen. Probleme der kosmischen Physik, 7, Hamburg, Germany, (in German).

Shibayama, T. and Rattanpitikon, W. 1993. Vertical distribution of suspended sediment concentration in and outside surf zone, Coastal Engineering in Japan 36, 49-66.

Shimozono, T., Masame, Y. and Okayasu, A., 2013. Image-based measurement of sediment flux for highly concentrated sediment-laden flows (in Japanese). Journal of JSCE 69(2), pp.1426-1430.

Shimozono, T., Masame, Y., Kobayashi, K. and Okayasu, A., 2012. Light-transmission planar measurement of sediment flux under water flow (in Japanese). Japanese J. Multiphase Flow 25(5), pp.435-442.

Shimozono, T., Sasaki, A., Okayasu, A., and Matsubayashi, Y., 2008. Laboratory measurement of high sediment concentration with light extinction method (in Japanese). Journal of JSCE 55, pp.1436-1440.

Soulsby, R. L. 1997. Dynamics of Marine Sands: A Manual for Practical Applications. London: Thomas Telford. pp. 249.

Swart, D.H., 1974, Offshore sediment transport and equilibrium beach profiles. Doctoral Thesis, Delft University of Technology.

Turner, I.L., Russell, P.E. and Butt, T., 2008. Measurement of wave-by-wave bed-levels in the swash zone. Coastal Engineering 55 (12), 1237–1242.

van der Zanden, J., Alsina, J.M., Caceres, I., Buijsrogge, R., and Ribberink, J.S., 2015. Bed level motions and sheet flow processes in the swash zone: observations with a new conductivity-based concentration measuring technique (CCM+). Coastal Engineering 105, 47–65.

Van Rijn, L. 1984. Sediment transport, part II: suspended load transport. Journal of the Hydraulics Division 110, 1613- 1641.

Vanoni, V.A., 1946. Transportation of suspended sediment by water. Transaction of ASCE 111, 67-133.

Wei, T., and Willmarth, W.W., 1989. Reynolds-number effects on the structure of a turbulent channel flow. Journal Fluid Mechanics 204, 57–95.

Wu, L., Feng, D., Shimozono, T. and Okayasu, A., 2014. Sediment flux measurement at high concentration based on image analysis with combined illumination. Journal of JSCE, Ser. B 70(2), 736–740.

Wu, L., Feng, D., Shimozono, T. and Okayasu, A., 2016. Laboratory measurements of sediment transport and bed level evolution in the swash zone. Coastal Engineering Journal 58, 1650004.

Zhang, Q. and Liu, P.L.F., 2008. A numerical study of swash flows generated by bores. Coastal Engineering 55, 1113–1134.

Zhu, F., and Dodd, N., 2013. Net beach change in the swash zone: a numerical investigation. Advances in Water Resources 53, 12–22.

Zhu, F., and Dodd, N., 2015. The morphodynamics of a swash event on an erodible beach. Journal of Fluid Mechanics 762, 110–140.

Zhu, F., and Dodd, N., Briganti, R., 2012. Impact of a uniform bore on an erodible beach. Coastal Engineering 60, 326–333.